UC Berkeley
UC Berkeley Electronic Theses and Dissertations

Title

Development and Deployment of Novel Arsenic Remediation Technologies in the Contexts of Rural India and the Central Valley of California

Permalink

https://escholarship.org/uc/item/5k2577vv

Author

Hernandez, Dana

Publication Date

2022

Peer reviewed|Thesis/dissertation

eScholarship.org Powered by the California Digital Library
University of California

Development and Deployment of Novel Arsenic Remediation Technologies in the Contexts of Rural India and the Central Valley of California

By

Dana Alejandra Hernandez

A dissertation submitted in partial satisfaction of the

Requirements for the degree of

Doctor of Philosophy

In

Engineering – Civil and Environmental Engineering

and the Designated Emphasis

in

Development Engineering

in the

Graduate Division

of the

University of California, Berkeley

Committee in charge:

Professor Ashok Gadgil, Chair
Professor Kara Nelson
Professor Alice Agogino

Fall 2022

Abstract

Development and Deployment of Novel Arsenic Remediation Technologies in the Contexts of Rural India and the Central Valley of California

By

Dana Alejandra Hernandez

Doctor of Philosophy in Civil and Environmental Engineering

and the Designated Emphasis in Development Engineering

University of California, Berkeley

Professor Ashok Gadgil, Chair

Globally, it is estimated that 94 – 220 million people are exposed to high levels of naturally occurring arsenic through groundwater used as a primary source of drinking water. High levels of arsenic refer to concentrations above the EPA and WHO allowable limit of 10 µg/L. Arsenic is a potent carcinogen that also causes skin lesions, ulcers, gangrene, and cardiovascular, neurological, and immunological diseases. While technologies exist that can effectively remove arsenic from drinking water sources, they have proved to be unsustainable in resource poor communities such as rural South Asia. Despite past investments in remediation projects, solutions were not installed with long-term sustainable societal placement strategies, resulting in failure of the technologies over time. In the U.S., the most affected communities tend to be small, rural, low-income, and marginalized communities lacking the technical, managerial, and financial capacity to implement and maintain arsenic remediation systems.

The purpose of this dissertation is to present insights from the lab to field trajectory, in the development and scale-up process, of novel arsenic remediation technologies for safe drinking water. First, the 10,000 LPD capacity ECAR (ElectroChemical Arsenic Remediation) plant at a high school in rural West Bengal, India, is used as a case study to shed light on the critical project efforts for ensuring a sustainable safe water system. The lessons learned from the field, with a focus during the commissioning phase (last six months) of the project, elucidate both the technical and social obstacles that were overcome working alongside a multidisciplinary and international team. From April 2016 to January 2017, a total of 540,000 liters of arsenic-safe water was produced, consistently and reliably reducing arsenic concentrations from initial 252 ± 29 to final 2.9 ± 1 µg/L. The ultimate commercialization of ECAR was based on its contextual design, a rigorous educational campaign and trust building, supporting local livelihoods, and complying with local regulations within a defined Critical Effort Zone (CEZ) period. Also key to the project was the financial support from a funding source focused on invention maturation into commercial systems. In short supply is the knowledge of how to transition from successful field testing to a scalable successful business model leading to large scale impact. The lessons from successfully crossing the “valley of death” are much less understood and much less reported on, than either of

the two sides of that valley. This work bridges a knowledge gap between case studies of successful technology field testing on one hand, and those reporting on technologies with good social acceptance, having achieved robust performance over long-term operation and implemented through a financially viable business model.

The takeaways from deployment of ECAR in rural India are then leveraged for development of a next generation system for the context of the Central Valley of California, requiring a higher throughput and more compact design. In the ECAR, or conventional iron electrocoagulation (Fe-EC) process, two large 1,250-liter tanks require aeration, and the entire treatment train spans a spatial footprint of 1,400 ft^2 to treat 500 liters per hour (LPH) of water contaminated with 250 μg/L arsenic. Adapting Fe-EC with a carbon-based air diffusion cathode allows for modularized electrochemical reactors to meet large throughput demands and treats 600 LPH of comparably arsenic contaminated water within a spatial footprint of about 120 ft^2.

Next, the performance of ACAIE (air cathode assisted iron electrocoagulation), or air-EC, in a synthetic California groundwater matrix, for co-removal of arsenic (As(III)) and manganese (Mn(II)) is investigated in the laboratory. The coulombic dosage rates (CDRs) reach over 300 times greater than at the ECAR plant, with a large dynamic range, from 6 to 1500 C/L/min, as well as a wide pH range from 4 to 10. Systematically varying these operating conditions and utilizing molecular-scale techniques, the reaction products are characterized to uncover the As(III) and Mn(II) removal mechanisms in air-EC. CDR did not have a major impact on removal efficiencies, but inverse trends with respect to pH were found for As(III) and Mn(II) removal. The MCL for As was reached at pH 4 and 7, while the secondary MCL for Mn was reached only at pH 10. Under the optimal pH values, removal was achieved in electrolysis times as short as 24 seconds. Furthermore, complete As(III) oxidation to As(V) was achieved, while only ~40% of Mn(II) was oxidized to Mn(III), indicating that As(III) more strongly competes for the reactive oxidant species in the system. Lastly, the As(V) was bound in binuclear, bidentate inner-sphere complexes with the electrolytically generated Fe(III) (oxyhydr)oxides, which is the dominant binding mode in conventional Fe-EC.

In the final section, we investigate the endpoints of the Fenton reaction that allow for effective and simultaneous As and Mn removal in air-EC, which relies on effective H_2O_2 generation at the cathode. Using Faradaic Efficiency (*FE*) as a performance metric, the efficacy of H_2O_2 production was assessed in both new and used modified gas diffusion layers (GDLs) to investigate the impact from air-EC operating conditions in a complex synthetic groundwater matrix. While operating at a high current density of 50.8 mA/cm^2, the *FE* values are high at ~80%, whereas at a low current density of 0.20 mA/cm^2, the *FE* yields are only ~30%. Scanning electron microscopy (SEM) and energy dispersive X-ray spectroscopy (EDS) are used to elucidate morphological attributes of the GDL base, newly modified- and used cathodes, and respective atomic compositions. Synchrotron-based XAS and X-ray fluorescence mapping were performed to obtain the elemental distribution of iron, calcium, chloride, and sulfur present on the cathode after use in the air-EC system. Raman Spectroscopy and X-ray photoelectron spectroscopy (XPS) were employed to offer potential mechanistic explanations for efficiencies and losses in H_2O_2 production, showing the reduction of defects in the carbon lattice. The loss of catalytic oxygen reduction reaction (ORR) sites contributed to the lower *FE* for H_2O_2 production. These results elucidate the role of groundwater composition in the fouling of the cathode in air-EC. While the

ionic composition of the arsenic-contaminated groundwater will vary across aquifers, the air-EC system can be designed as a two-chamber system to minimize fouling from the anodically generated Fe precipitates.

The lessons learned from the field in India will continue to inform the development and deployment of ACAIE within the Central Valley of California. Work remains to better understand the stability of the As- and Mn-laden precipitates and potential remobilization of contaminants once in typical landfill conditions. At the cathode, effective and simple regeneration methods must be further investigated to increase lifespan while minimizing maintenance costs. Finally, long-term operation of the air-EC system must be optimized in the field, as well as the implementation of a sustainable business model contextual to rural California.

Para mi papá,

Quien me enseñó,

Que la solución somos todos.

Table of Contents

Chapter 1. Introduction…… 1
1.1 The Global Arsenic Problem……..... 1
1.1.1 The India Context……...……. 2
1.1.2 The California Context……...……. 3
1.2 Arsenic in Groundwater……. 4
1.2.1 Impacts of Climate Change……. 5
1.3 Existing Technologies…… 6
1.3.1 Adsorption……..... 6
1.3.2 Co-precipitation……..... 7
1.3.3 Membrane Separation……. 7
1.3.4 Ion Exchange……..... 8
1.4 Need for a Novel Solution……..... 10
1.5 Novel Electrochemical Technologies……. 10
1.5.1 ElectroChemical Arsenic Remediation……..... 10
1.5.2 Air Cathode Assisted Iron Electrocoagulation…… 12
1.6 Outline of Remaining Chapters……..... 13
Chapter 2. Strategies for Successful Field Deployment in a Resource-Poor Region: Arsenic Remediation Technology for Drinking Water……. 15
2.1 Introduction and Background……. 15
2.2 ECAR: From Lab to Field……..... 16
2.2.1 The First Large-Scale ECAR Plant……...……..... 17
2.3 Critical Effort Zone…… 20
2.4 Critical Effort Strategies……. 23
2.4.1 Community-Scale Technology Design……... 23
2.4.2 Increasing Economic Opportunity……..... 29
2.4.3 Bridging the Knowledge Divide……. 29
2.4.4 Compliance with Local Regulations……... 31
2.4.5 Addressing Sustainable Development Goals (SDGs)……. 31
2.5 Concluding Remarks……..... 32
Chapter 3. Inverse Trends of As(III) and Mn(II) Removal in Air Cathode Assisted Iron Electrocoagulation…… 34
3.1 Introduction and Background……. 34
3.2 Materials and Methods……... 36
3.2.1 Reactor…… 36
3.2.2 Groundwater Synthesis……..... 37
3.2.3 Batch Experiments……..... 37
3.2.4 Chemical Measurements……. 38
3.2.5 Solid Phase Characterization……... 38
3.3 Results…… 39
3.3.1 Mn Removal…… 39
3.3.2 As Removal……. 41

3.3.3 Removal of Competing Species……..... 42
3.3.4 X-ray Diffraction of Fe Precipitates…… 44
3.3.5 Transmission Electron Microscopy of Fe particles……. 44
3.3.6 Fe K-edge EXAFS and LCFs……..... 47
3.3.7 Fe K-edge EXAFS Fourier Transform Shell-by-Shell Fits……. 49
3.3.8 Mn K-edge XANES and LCFs…… 51
3.3.9 As K-edge XANES and LCFs……. 53
3.3.10 As K-edge EXAFS Fourier Transform Shell-by-Shell Fits……..... 54
3.4 Discussion……..... 57
3.4.1 Fe Phase Generated in SCaGW as a Function of pH and CDR…….. 57
3.4.2 Effect of pH and CDR on Mn removal……... 58
3.4.3 Effect of pH and CDR on As removal…… 59
3.4.4 Technical and Environmental Implications……. 59
Chapter 4. Investigating Performance of Modified Gas Diffusion Layer in Air-EC……... 61
4.1 Introduction…… 61
4.2 Materials and Methods……... 62
4.2.1 Cathode Fabrication…… 62
4.2.2 Faradaic Efficiency Tests…… 62
4.2.3 Reactor Configurations..…… 63
4.2.4 Electrolyte Compositions.……..... 64
4.2.5 Cathode Characterization…… 64
4.3 Results and Discussion……... 65
4.3.1 Faradaic Efficiencies for H_2O_2 Production……. 65
4.3.2 Macroscopic Surface Layer Properties……... 67
4.3.3 Impact of Modification and Use on Morphology and Atomic Composition…..... 68
4.3.4 Influence of Complex Electrolyte on Precipitate Species……... 73
4.3.5 Effect of Air-EC Operating Conditions on ORR Catalytic Sites…… 77
4.3.6 Anode Characterization……... 82
4.3.7 Technical and Environmental Implications……. 83
Chapter 5. Conclusions…… 85
5.1 Strategies for Successful Field Deployment in a Resource-Poor Region: Arsenic Remediation Technology for Drinking Water……. 85
5.1.1 Summary of Results…… 85
5.1.2 Implications of Research and Future Work……. 85
5.2 Inverse Trends of As(III) and Mn(II) Removal in Air Cathode Assisted Iron Electrocoagulation…… 86
5.2.1 Summary of Results…… 86
5.2.2 Implications of Research and Future Work……. 87
5.3 Investigating Performance of Modified Gas Diffusion Layer in Air-EC……... 88
5.3.1 Summary of Results…… 88
5.3.2 Implications of Research and Future Work……. 88
References…… 90

List of Figures

Figure 1.1 Map of probabilities of global arsenic contamination in groundwater. Magnified areas indicate the regions where probabilities of high arsenic presence are relatively high. Image from Podgorski et al., 2020.[2] 1

Figure 1.2 Arsenic presents the highest risk of lifetime-cancer compared to regulated carcinogens in drinking water. Figure values are based on relative risk data from Smith et al., 2002.[17]. 2

Figure 1.3 Speciation of trivalent arsenite (a) and pentavalent arsenate (b) as a function of pH. The points where the curves intersect represent the pKa of each species, where α represents the fraction of each species of arsenous acid (a) and arsenic acid (b). 4

Figure 1.4 Eh-pH diagram for arsenic in As–O_2–H_2O system at 25 ºC and 101.3 kPa. Image from Nicomel et al., 2015.[42] 5

Figure 1.5 Schematics of ECAR and ACAIE. The major difference is the oxidant reacting with Fe(II). ECAR relies on the recharge of oxygen into the bulk solution. ACAIE does not depend on DO because the system generates H_2O_2 in-situ, which reacts more quickly with Fe(II), or by four orders of magnitude.[62] Owing to its faster chemical kinetics, ACAIE reactor is also more compact relative to ECAR reactor for the same throughput rate of treated water. 12

Figure 2.1 Over the course of 10 years, ECAR scaled successfully and progressively from a 0.2-liter beaker, to 100-liter and 600-liter prototypes, to a 10,000-LPD capacity field pilot plant. ... 16

Figure 2.2 Digital photographs of the 10,000 LPD capacity pilot plant at Dhapdhapi High School. a) ECAR Room: Contains the two ECAR reactors in which electrolysis occurs b) Tube Settler Room: Contains the tube settler, flocculation chamber, and subsequent tertiary treatment systems for particle separation. 17

Figure 2.3 Schematic representation of the treatment process at the Dhapdhapi pilot plant: 1) raw water pump, 2) ECAR reactors, 3) flocculation chamber, 4) tube settler, 5) rapid sand filter, 6) micron filters, 7) ultraviolet disinfection system, 8) automatic dispensing unit..... 17

Figure 2.4 a) ECAR Power Supply: Supplies the current to the two ECAR reactors in order for electrolysis, or the dissolving of the iron anodes, to occur. b) Main Circuit Board: Located in the Tube Settler Room, the main electrical board provides power to the entire plant..... 18

Figure 2.5 Results from the plant in West Bengal, India, from April 2016 to January 2017, depicting continuous effective arsenic removal to less than 10 ppb during both pilot and distribution phases. The spike in arsenic concentration around 23-May and excellent performance after 1-Aug are explained in Section 2.4.1. 20

Figure 2.6 Navigating the innovation path. The Critical Effort Zone requires more than technology efficacy—acceptable social placement within unique environmental contexts is also necessary.

This figure is modified from a presentation to the United Kingdom parliament[80] and public presentations about technology-maturation programs at the U.S. Department of Energy. 21

Figure 2.7 a) The busbar connections of the 6-mm wires, each wire connecting one of the 16 plates (total 32 plates in total 2 reactors) to a busbar, were all initially placed facing away from the reactor wall, thus, making them susceptible to daily accidental yanks and pulls while electrode plates were brushed, and therefore causing fraying at the connection to the busbar. b) After rewiring for improved performance, the connection of each wire is now placed facing the reactor wall, avoiding direct physical pull on the connection, and avoiding any sharp angles that would cause stress at the wire ends. 24

Figure 2.8 a) The red and black cables connect the polarity-reversal switch to the miniature circuit-breakers of the reactor tanks 1 and 2. b) In the reviewed layout, new black and red cables connect the polarity-reversal switch to the reactor tank miniature circuit breakers. Excess wiring was given in case of future heat damage that may also require trimming the cables and securing them again with a new copper lug. However, that has not happened owing to the corrosion inhibitor that has been applied to the folded copper busbars. 25

Figure 2.9 a) Components of the polarity switch showing burned insulation from overheating. b) A new lug (left) compared to the previous burnt-insulation lug (right). On the burnt insulation, the (green) corrosion of the copper wires is visible. New copper 95 mm lugs were placed on the 70 mm^2 wires, and new heat shrinkable rubber slip tubes of higher quality were placed on the two cross-over bars in the back (not pictured). 25

Figure 2.10 a) Cable tray leading towards reactor tanks. b) Red and black wires guided down from the cable tray to the miniature circuit breaker of reactor tank 1, and to the polarity switch where the wires from reactor tanks 1 and 2 meet. 26

Figure 2.11 The two white-colored holding tanks were placed directly above the automatic dispensing units where drinking water is collected. 26

Figure 2.12 This figure shows a) sample of the cards distributed to the students and teachers of Dhapdhapi. In Bengali, the card says, “Let us keep our health and our family’s health safe by accessing arsenic-free water from arsenic-safe sources," b) school girl who has just received her own card with spaces for name, grade level, roll number, and water card number, c) automatic dispensing units installed, and d) water queue formed during first water distribution. 28

Figure 3.1 a) Digital picture and b) schematic of air-EC. The current supplied to the system oxidizes the Fe(0) in the iron anode to Fe(II), depicted as green circles. At the cathode, hydrogen peroxide (H_2O_2) is generated. In the bulk solution, Fe(II) released from the sacrificial anode reacts with H_2O_2 to form Fe(III), depicted as orange circles, which is highly insoluble at circumneutral pH, and simultaneously generates reactive intermediates, like Fe(IV) and $^{\bullet}OH$, which oxidize arsenite, As(III) (light purple circles) to arsenate As(V) (dark purple circles), the more readily removed form of As. To a lesser extent, there is also oxidation of Mn(II) (light grey circles) to Mn(III) (dark grey circles). The Fe(III) captures the As and Mn and the aggregated precipitates settle out of solution, leaving As- and Mn-safe water at the effluent. 36

Figure 3.2 As(III) and Mn(II) removal from synthetic California groundwater as a function of CDR and pH. The total Coulombic dose was 600 C/L. The dashed line refers to either a) the primary MCL for As of 10 μg/L or b) the secondary MCL for Mn of 50 μg/L. 40

Figure 3.3 As:Fe and Mn:Fe ratios of adsorbed species onto electrolytically generated iron (oxyhydr)oxides for total of 3.1 mM Fe.. 41

Figure 3.4 P and Ca removal from SCaGW as a function of CDR and pH. The total Coulombic dose was 600 C/L.. 42

Figure 3.5 P:Fe and Ca:Fe ratios of adsorbed species onto electrolytically generated iron (oxyhydr)oxides for total of 3.1 mM Fe.. 43

Figure 3.6 XRD of precipitate samples generated in a range of CDRs at a) pH 7, pH 10, and b) pH 4.. 44

Figure 3.7 TEM of samples from air-EC experiments conducted at a) pH 7 and 600 C/L/min, and c) pH 4 and 6 C/L/min. Panels b and d are the magnified regions outlined in panels a and c, respectively.. 45

Figure 3.8 TEM of samples generated in a Synthetic Bengal Groundwater (solution matrix described in Delaire et al., 2015)[34]. The scale bar for both micrographs is 200 nm. The smoothness of the spherical particles indicates a highly disordered Fe(III) state.. 46

Figure 3.9 Size distribution of particles as determined using ImageJ software..... 46

Figure 3.10 Additional TEM micrographs of particles depicting morphology and chain-like aggregation in Synthetic Bengal Groundwater. The scale bar across micrographs is 200 nm.. ... 47

Figure 3.11 Fe K-edge EXAFS spectra for selected samples at pH 7 and 10. 48

Figure 3.12 Fourier-transformed EXAFS spectra and shell fits of selected samples. Dashed lines represent data and solid lines represent the fit. 50

Figure 3.13 Mn K-edge XANES spectra. Vertical dashed lines are placed on the absorption maximum of each reference mineral spectrum. 52

Figure 3.14 As K-edge XANES spectra. Vertical dashed lines are placed on the absorption maximum of each reference spectrum. 53

Figure 3.15 As K-edge a) EXAFS and b) Fourier Transform. 55

Figure 4.1 Digital photographs of a) front view of air-EC reactor showing the air-facing (graphite layer), the titanium current collector, and 10 bolts, washers, and wing nuts, b) back view of reactor comprised of a HDPE plate fitted with 10 bolts and washers, and the MMO anode, c) top view of reactor showing the modular components tightened together with gaskets between each HDPE

sheet to create a leak-proof system. The flexible light-yellow material in the middle is the AEM that creates a two-chamber system. 64

Figure 4.2 Comparison of *FE* for H_2O_2 production in air-EC of new and used cathodes operated at three selected dosage rates (1500, 600 and 6 C/L/min). 66

Figure 4.3 pH and DO values of catholyte (squares) and anolyte (triangles) chambers for new (blue-colored markers) and used (orange-colored markers) cathodes at the end of electrolysis. The dotted line represents the initial average pH and DO values of the electrolyte. In panel a, the orange triangle markers are slightly shifted in the x-axis to make the blue markers visible. 67

Figure 4.4 Digital photographs of the a) as-purchased carbon fiber paper, b) a newly modified cathode (the CB water-facing side), and c) a used cathode after a 40-experiment series, as representative samples for various characterization techniques. 68

Figure 4.5 SEM images of a) as-purchased carbon fiber paper, b) newly modified cathode (the CB water-facing side), and c) used cathode. 69

Figure 4.6 Cross-sectional SEM images of a) carbon fiber paper, b) magnified region as indicated by the white boxed region in panel a, c) new cathode, and d) used cathode. 69

Figure 4.7 SEM images of a) prepared water-facing catalytic side and b) graphite air-facing side, and c) water-facing side and d) air-facing side atomic percent elemental compositions. 70

Figure 4.8 SEM images comparing a) new cathode and b) used cathode. The dashed boxes indicate the regions that may contain distinct phases of iron precipitates. 71

Figure 4.9 SEM and EDS of used cathodes corresponding to a and c) HFO-appearing species, and b and d) lepidocrocite-appearing species. 72

Figure 4.10 XRD of the carbon fiber paper, newly modified cathode, and used cathode. T and G refer to PTFE and graphite, respectively. 73

Figure 4.11 The eight sample locations of the used cathode that were probed with μXRF and μXANES spectroscopy. 1 x 1 cm^2 samples were cut as indicated by the numbered spots, each corresponding to either the top, middle, or bottom region of the cathode. The top region was closest to the electrolyte/air interface, as the reactor operated as an open-air batch process. 74

Figure 4.12 μXRF maps of samples 5, 6, and 7. The Fe map was scanned at 100 eV above the Fe K-edge. Other maps were acquired at 100 eV above the Ca K-edge. The spot labels on the Ca map indicate the points that were selected for Ca K-edge μXANES. The scale bars are 50 μm. 75

Figure 4.13 Ca K-edge μXANES on selected spots of μXRF maps. 76

Figure 4.14 μXRF maps of samples 2 and 3. The Fe map was scanned at 100 eV above the Fe K-edge. Other maps were acquired at 100 eV above the Ca K-edge. The spot label on the Ca map

indicates the point selected for Ca K-edge μXANES. The scale bars are 20 μm (sample 2) and 50 μm (sample 3). 77

Figure 4.15 Raman spectra of representative samples of carbon fiber paper, newly modified cathode, and used cathode..... 78

Figure 4.16 XPS spectra of representative samples of carbon fiber paper, newly modified cathode, and used cathode a) survey spectra b) carbon paper, c) new cathode, and d) used cathode C 1s spectrum. 79

Figure 4.17 XPS O 1s spectrum of a) newly modified cathode and b) used cathode. 81

Figure 4.18 SEM of a) unused iron anode and b) iron electrode after use at high dosage rates (50 – 100 C/L/min, 5 – 10 mA/cm^2 or) and c) vertical scanning interferometry of the used anode... 83

List of Tables

Table 1.1 Summary of advantages and disadvantages of existing arsenic removal technologies……... 9

Table 2.1 Raw water average element concentrations as tested by ICP-OES at UC Berkeley……. 19

Table 2.2 Actions taken during the Critical Effort Zone to address the UN's SDGs…… 32

Table 3.1 Solution Chemistry of Synthetic California Groundwater…… 37

Table 3.2 Solids ratio of adsorbed As and Mn species onto Fe solids…….. 41

Table 3.3 Solids ratio of adsorbed P and Ca species onto Fe solids……. 43

Table 3.4 Initial molar ratios of various elements to Fe content (3.1 mM) in SCaGW…… 43

Table 3.5 Results of LCFs using the Fe K-edge Chi data……. 49

Table 3.6 Summary of shell-by-shell fitting results…….. 51

Table 3.7 Summary of the Mn K-edge XANES LCFs……. 52

Table 3.8 Summary of the As K-edge XANES LCFs……..... 54

Table 3.9 Summary of shell-by-shell fitting results for As……..... 56

Table 4.1 Atomic % from XPS analysis of used cathode condition……. 80

Table 4.2 Results of C 1s deconvolution of all samples……... 80

Table 4.3 Results of O 1s deconvolution of all samples……... 82

List of Abbreviations

AA	Activated Alumina
AC	Activated Carbon
ACAIE	Air Cathode Assisted Iron Electrocoagulation
AEM	Anion Exchange Membrane
ALS	Advance Light Source
AOP	Advanced Oxidation Process
ARE	Arsenic Removal Efficiency
BSE	Backscatter Electron
CEZ	Critical Effort Zone
CFD	Computational Fluid Dynamics
COE	Consent to Establish
COO	Consent to Operate
DI	Deionized
DIC	District Industries Center
DO	Dissolved Oxygen
DOC	Dissolved Organic Carbon
EAOP	Electrochemical Advanced Oxidation Process
EC	Electrocoagulation
ECAR	ElectroChemical Arsenic Remediation
EDS	Energy Dispersive X-ray Spectroscopy
EIS	Electrochemical Impedance Spectroscopy
EPA	Environmental Protection Agency
EXAFS	Extended X-ray Absorption Fine Structure
FE	Faradaic Efficiency
Fe-EC	Iron Electrocoagulation
GAC	Granular Activated Carbon
GCP	Global Change Program
GDL	Gas Diffusion Layer
HCl	Hydrochloric Acid
HDPE	High Density Polyethylene
HFO	Hydrous Ferric Oxide
IARC	International Agency of Research on Cancer
ICP-MS	Inductively Coupled Plasma Mass Spectroscopy
ICP-OES	Inductively Coupled Plasma Optical Emission Spectroscopy
JU	Jadavpur University
LCF	Linear Combination Fit
LBNL	Lawrence Berkeley National Laboratory
MCL	Maximum Contaminant Level
MF	Microfiltration
μXRF	Micro-Focused X-ray Fluorescence
NF	Nanofiltration
NOC	No Objection Certificate
NOM	Natural Organic Matter
ORR	Oxygen Reduction Reaction
PAC	Powdered Activated Carbon

PHG	Public Health Goal
PIPS	Passivated Implanted Planar Silicon
PTFE	Polytetrafluoroethylene
PZC	Point of Zero Charge
RO	Reverse Osmosis
SDG	Sustainable Development Goal
SEM	Scanning Electron Microscopy
SSRL	Stanford Synchrotron Radiation Lightsource
TMF	Technical, Managerial and Financial
UC	University of California
UF	Ultrafiltration
UN	United Nations
USGS	United States Geological Survey
WBPCB	West Bengal Pollution Control Board
WHO	World Health Organization
WTP	Willingness To Pay
XANES	X-Ray Absorption Near Edge Structure
XAS	X-Ray Absorption Spectroscopy
XFM	X-Ray Fluorescence Microprobe
XPS	X-Ray Photoelectron Spectroscopy
XRD	X-Ray Diffraction
XRF	X-Ray Fluorescence
ZLD	Zero Liquid Discharge

Acknowledgements

I would first like to thank my family: My mom, Elvira Higuera, my dad, Luis F. Hernández, my brother, Fernando Hernández, and my sister, Paola Hernández Romero, for supporting and encouraging me throughout my academic journey, no matter how far I go from home.

I am grateful to my research advisor, Ashok Gadgil, whose dedication to solving global challenges inspired me and confirmed my decision to pursue a PhD. Thank you for your guidance since I joined the group as a field engineer, your mentorship along the stages of the PhD, and for the many engaging and insightful discussions over the years which have shaped how I approach problems and conduct research.

I thank my dissertation committee members, Professors Kara Nelson and Alice Agogino, for their support and feedback on my doctoral work, and advice whenever I needed to pivot my focus. I also thank Professors Baoxia Mi, Céline Pallud, and Laura Lammers for their recommendations as I prepared for my preliminary and qualifying exams. I'm thankful to Katya Cherukumilli for being a wonderful role model, helping me get started in the lab early on and exposing me to impactful entrepreneurship. I want to express my gratitude to my mentor, Case van Genuchten, who introduced me to synchrotron-based spectroscopic techniques and offered many hours of guidance on experimental design, sample preparation, data collection, reduction, and analysis, and writing. I'm thankful to Siva Rama Satyam Bandaru for being such a caring mentor, lab mate, and friend all throughout my PhD.

I'm appreciative of the warm welcome I received and the support I had during my field work from our partners at Jadavpur University and the Global Change Program, including Professor Joyashree Roy, Prasenjit Paul, Monalisa Ghosh, Abhisek Roy, Shreya Some, Jayanta Talukder, Rajesh Bhattacharya, and the community at Dhapdhapi High School. I am thankful to our collaborators in the School of Public Health, including Winston Tseng, and to our community partners in Lemoore and in Allensworth. I appreciate the support from Sirine Fakra at the Advanced Light Source, Reena Zalpuri at the Berkeley Microscope Lab, John Grimsich at the Earth and Planetary Science Department, Tracy Mattox, Anne Pham, Tevye Kuykendall, Emory Chan, and Virginia Altoe at the Molecular Foundry, Ryan Davis at the Stanford Synchrotron Radiation Lightsource, and Jacob Gallego and Jeff Higginbotham at the UCB Student Machine Shops. I am thankful to the undergraduate and master's student researchers who helped me with experimental work: John Cadiz, Meire Mehare, Julian Falagán, Sara Mahmoud, and Chandra Vogt.

I am thankful for my lab mates and dear friends. From helping me in the lab, reviewing pieces of writing, or hosting dinners and weekend game nights, I greatly appreciate you all: Emily Cook, Gabriel Lobo, Bavisha Kalyan, Andrea Naranjo-Soledad, Jay Majmudar, Kate Boden, Sara Glade, Mohit Nahata, Lukas Hackl, Bilen Aküzüm, Logan Smesrud, Andrew Haddad, Daniel Ocasio, Yanghua Duan, Soliver Fusi, and Rohini Tamarana. I'm thankful to all my peers in the Berkeley Water Center for sharing many lunches and coffee breaks over the years. I thank my friends, including Mathias Paumgarten, Kristen Legault, and Johan Jaenisch, with whom I've shared delicious potlucks, trail running, and climbing adventures over the years.

Finally, I am grateful to my partner, Niklas Mundhenk, for his unconditional love and support the last five years. Early on you helped me with my electrochemistry questions, and towards the end have provided stability as I navigate future steps. Whether it has been making progress in research, or climbing a new grade in the bouldering gym, you make sure that we celebrate each milestone along the way. Thank you for everything.

I also want to acknowledge the funding sources and resources that made my doctoral work possible: UC Berkeley Chancellor's Fellowship, National Science Foundation (NSF) Graduate Research Fellowship, NSF Innovations at the Nexus of Food, Energy, and Water Systems (InFEWS) Fellowship (Grant No. DGE-1633740), the SMART Mentorship Program, CERC-WET Project 2.9, and the CEE department. Work at the Molecular Foundry and ALS was supported by the Office of Science, Office of Basic Energy Sciences, of the U.S. Department of Energy under Contract No. DE-AC02-05CH11231. The Graduate Division Conference travel grants partially supported a domestic and international trip to present my research. I also acknowledge the Big Ideas Award through the Blum Center for Developing Economies, the Environmental Protection Agency (EPA) People, Prosperity, and the Planet (P3) Phase I and Phase II awards, and the University of California Office of the President (UCOP) Tobacco-Related Disease Research Program (TRDRP) for broader project efforts in bringing arsenic-safe drinking water to the Central Valley of California.

Chapter 1. Introduction

1.1 The Global Arsenic Problem

Globally, up to 220 million people are estimated to be exposed to high levels of arsenic through contaminated groundwater, which is used as a primary source of drinking water.[1–3] High levels of arsenic refers to concentrations above 10 micrograms per liter (µg/L), which is the World Health Organization (WHO) guideline limit.[4] Figure 1.1 from Podgorski et al., 2020 shows the global probabilities of high arsenic being present in the groundwater.

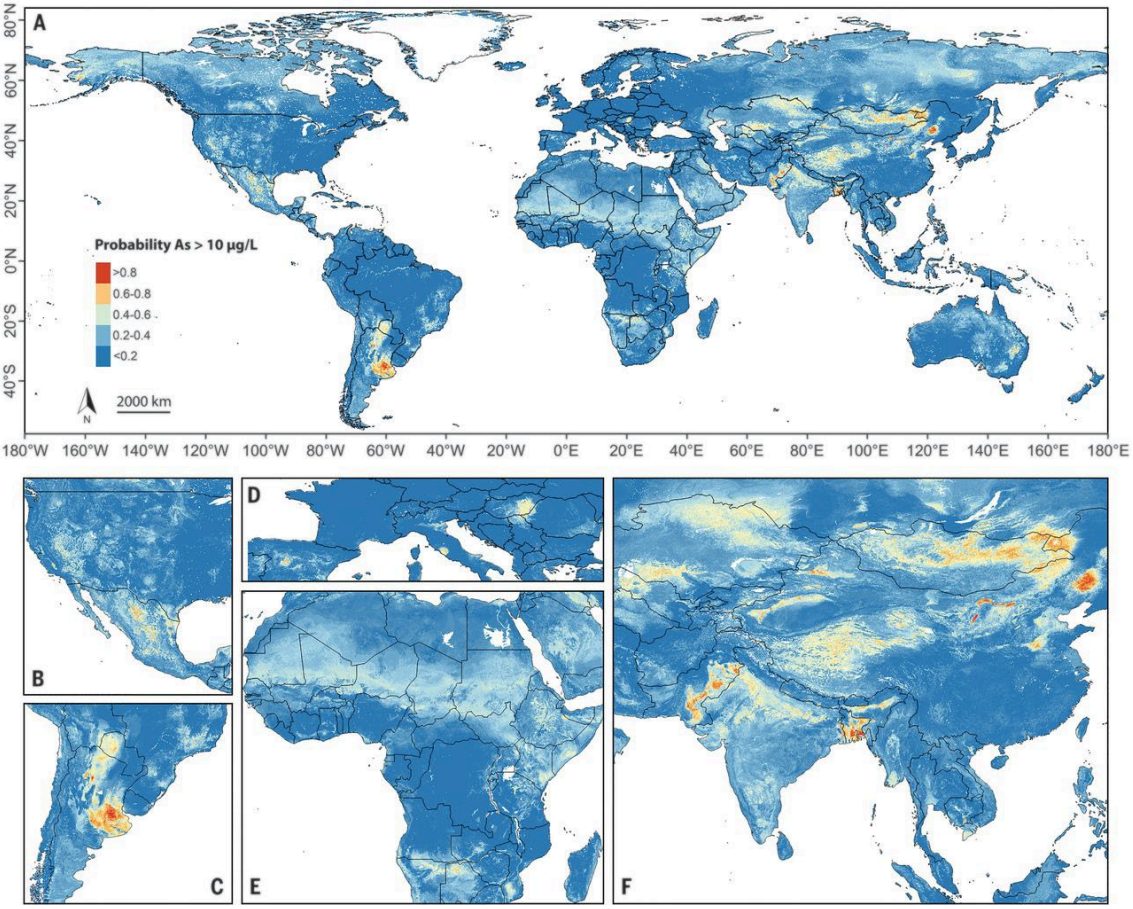


Figure 1.1 Map of probabilities of global arsenic contamination in groundwater. Magnified areas indicate the regions where probabilities of high arsenic presence are relatively high. Image from Podgorski et al., 2020.[2]

Arsenic is an odorless, colorless, and tasteless naturally occurring toxic contaminant found in groundwater.[5,6] This metalloid causes cardiovascular, immunological, dermatological, neurological, developmental, and respiratory diseases.[3,7] Arsenic exposure also increases risk for diabetes, and recent studies have shown that low-level (below 10 µg/L) arsenic may impact fetal growth and may be related to preterm birth.[8,9] Chronic exposure to high concentrations of arsenic leads to gangrene of the extremities, keratosis and skin lesions.[7,10] As classified by the International Agency of Research on Cancer (IARC) and the Environmental Protection Agency (EPA), arsenic is a Class I and Group A Human Carcinogen, respectively, causing skin, lung, bladder, kidney,

and liver cancers.[3,11,12] In 2001, the carcinogenic potency of inorganic arsenic was determined to cause 350 excess internal cancers in a population of 100,000 exposed to a lifetime daily consumption of one liter of water at its current MCL of 10 µg/L.[13,14] However, more recent estimation methods assume a daily consumption of two liters, which doubles these estimates of excess cancer incidence.[15,16] Figure 1.2 shows that arsenic, at its MCL, poses the highest cancer risk of any regulated carcinogenic water contaminant, at their respective MCLs, in the United States.[16,17]

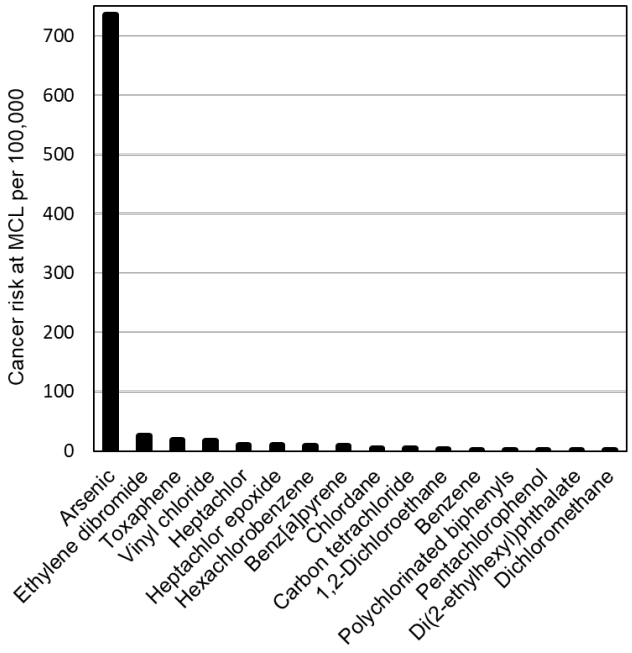


Figure 1.2 Arsenic presents the highest risk of lifetime-cancer compared to regulated carcinogens in drinking water. Figure values are based on relative risk data from Smith et al., 2002.[17]

Although the WHO limit for arsenic is currently 10 µg/L, its first recommended guideline limit was set at 200 µg/L in 1958.[18] The MCL was lowered in 1963 to 50 µg/L after epidemiological studies demonstrated the chronic toxicity of arsenic ingestion. It wasn't until 1993 that the WHO limit was lowered to its current value.[18] In the U.S., the EPA did not lower its Maximum Contaminant Level (MCL) from 50 to 10 µg/L until 2006.[19] To better safeguard its population's health, the Netherlands has lowered its MCL to 1 µg/L.[20] Various countries, such as Bangladesh and India, still hold a higher guideline limit value of 50 µg/L.[18,21] Specific to the Indian standard, the 10 µg/L is the desirable MCL but 50 µg/L is permitted if a lower level cannot be achieved.[22]

1.1.1 The India Context

About 90 million of the arsenic-affected population reside in Bangladesh and West Bengal, India, making them the worst arsenic-affected regions of the world.[23,24] High levels of arsenic in groundwater were first discovered in 1983 within 33 villages of West Bengal, but it was not until 1999 that the devastating effects of this emerging health crisis became evident.[25] In Bangladesh it was found that arsenic exposure through drinking water accounts for 24,000 annual deaths, and

accounts for up to 15% of all adult deaths.[26] A survey of household water samples in 2013 found that 12.4% were arsenic contaminated.[24]

Many attempts to address the public health crisis of arsenic in South Asia have been made over the past three decades. Unfortunately, most of these interventions have failed to provide arsenic-safe drinking water over a prolonged basis. The installed arsenic remediation technologies are often too expensive or too complicated to operate long-term in resource-poor communities with low technical skill. In West Bengal, household- and community-scale arsenic treatment units installed during the past decade typically became dysfunctional within one year of installation.[27] In one of the most seriously arsenic-affected districts of West Bengal, the Murshidabad District, 93% of 70 implemented arsenic removal technologies failed within one to eight months.[28]

1.1.2 The California Context

The United States Geological Survey (USGS) estimates that 2.1 million people rely on private wells with high arsenic concentrations.[29] In California, about 55,000 people rely on public water systems that are out of compliance with regards to arsenic,[30] not including households relying on unmonitored private wells. These systems typically serve rural underrepresented communities of lower socioeconomic status, and lack the technical, managerial, and financial (TMF) capacity to implement and sustain treatment technologies.[31] Like in rural India, communities in rural California have faced challenges in finding suitable affordable, manageable, and effective existing arsenic removal technologies on the market.[32] There is a lack of access to long-term solutions that remove high levels of arsenic to below 10 µg/L. Moreover, although lowering the allowable limit to 0.004 µg/L is a public health goal, it will further add costs to small water systems already struggling with TMF capacity.[33] Moreover, reducing to levels below 10 µg/L also requires lower detection limits of arsenic quantification instruments, which may not be available.[34]

Any California public water system that is out of compliance with water quality norms receives a notification requiring compliance by a given deadline. The water providers, in turn, are required to notify their customers of their failure to meet EPA standards. However, oftentimes these notifications underplay the magnitude of the problem and do not accurately present the implications of consuming water with unhealthy concentrations of arsenic. The notice template simply states that there is no emergency and that customers "do not need to use an alternative water supply," but that they may consult a doctor if necessary.[30]

Public water systems, regardless of their type or size, must consistently provide safe water for human consumption. Human consumption is defined as more than just for drinking, and specifically as "the use of water for drinking, bathing or showering, hand washing, oral hygiene, or cooking, including but not limited to, preparing food and washing dishes."[35] In California, the daily average household water use per capita is 146 gallons, or 553 liters.[36] To be able to provide such volumes of arsenic safe water, small public water systems need to acquire the TMF capacity. However, their economies of scale do not allow them to spread out costs to install and maintain such large treatment facilities, especially without any financial support granted from government entities. Rural communities in California are disproportionately affected by arsenic contamination. Thus, this problem has been cited as an environmental justice issue as most out-of-compliance small water systems serve poor, Latinx and African American communities.[31,37]

When a small water system is deemed out of compliance with respect to arsenic, there are currently several ways to address the problem. Through consolidation, small water systems can be connected to a large, centralized treatment facility operated by a larger utility. However, rural communities are often isolated and lack sufficient infrastructure to connect their water lines to a major utility. As such, consolidation is rarely affordable. Well replacement or well deepening may solve the problem if the local geology and hydrology is fully understood. This process is cost intensive, and improved water quality from new or deepened wells is not guaranteed. Moreover, bottled water purchases for drinking and cooking reduce arsenic exposure but are not deemed an affordable or sustainable solution. Current commercial arsenic removal technologies, as described in Section 1.3, include ion exchange (IE), reverse osmosis (RO), and adsorption media. The performance of these technologies may be adversely affected by changes in groundwater quality (i.e., pH or salinity), or by the oxidation state in which arsenic is present. These systems may often be installed as household Point of Use (POU) treatment devices, as opposed to centralized plants, but may not always be deemed as an acceptable small system compliance technology.[11]

Small water systems face challenges of having to adopt technologies designed for larger systems, facing a higher cost burden.[6,38] Thus a sustainable system requires simplicity, low capital and operating and maintenance costs, and appropriate management of residual wastes from treatment to avoid any reintroduction of harmful contaminants back into the environment.

1.2 Arsenic in Groundwater

Although there are anthropogenic sources of arsenic contamination in drinking water (e.g., mining and smelting, coal burning, pesticides), arsenic is typically mobilized under natural hydrogeochemical processes.[7] While arsenic may exist in the -3, -1, 0, +3, and +5 oxidation states in the natural environment, it most commonly occurs as inorganic oxyanions arsenite (H_3AsO_3) or arsenate (H_3AsO_4) in groundwater.[14,39] Arsenite refers to trivalent As(III) arsenous acid, and arsenate refers to pentavalent As(V) arsenic acid. As seen in Figure 1.3, As(III) and As(V) occur as their dissociated or non-dissociated forms as a function of pH. The dissociation constants, or pKa's, for As(III) are 9.23, 12.13, and 13.40, and for As(V) they are 2.20, 6.97, and 11.53.[40]

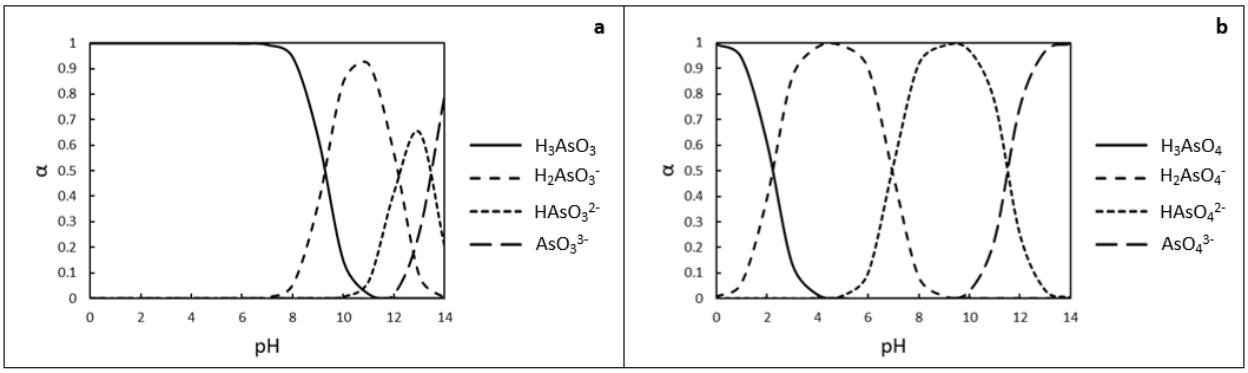


Figure 1.3 Speciation of trivalent arsenite (a) and pentavalent arsenate (b) as a function of pH. The points where the curves intersect represent the pKa of each species, where α represents the fraction of each species of arsenous acid (a) and arsenic acid (b).

In addition to pH, the speciation of arsenic relies on the redox potential (Eh) of the water. As seen in the Pourbaix diagram (Figure 1.4), As(V) is thermodynamically stable under oxidizing conditions, whereas As(III) predominates in moderately reducing anoxic environments. In oxic

environments, at relevant groundwater pH levels between 6.5 and 8.5, As(V) will be dominantly present as ionized $H_2AsO_4^-$ and $HAsO_4^{2-}$. Under reducing conditions, the neutral form of As(III), H_3AsO_3, will predominate.

The proportions of As(III) and As(V) in groundwater vary across diverse geochemical conditions. In both oxic and anoxic conditions at relevant groundwater pH levels, arsenic species have high solubility and can become readily mobilized. The solubility of oxyanionic arsenic increases as pH increases, which can lead to concentrations up to mg/L levels.[14,34] For example, arsenic is released from minerals after reduction of iron phases or with oxidizing sulfites.[41] If under oxic conditions the pH increases above ~8.5, As(V) adsorbed to metal oxides will desorb. Under reducing conditions, arsenic may become mobilized after dissolution of soluble minerals on which arsenic was initially adsorbed.

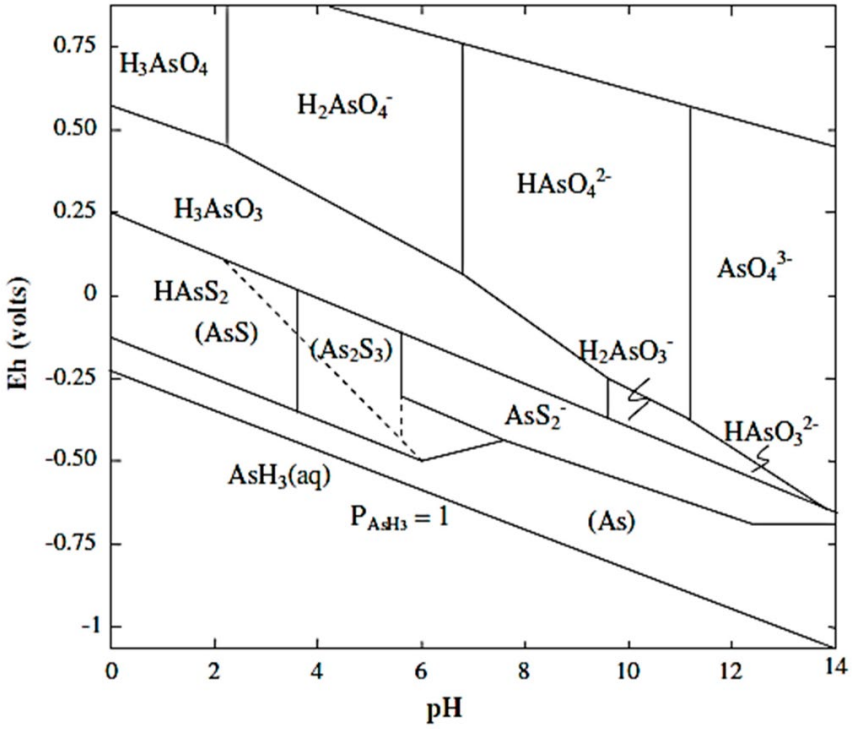


Figure 1.4 Eh-pH diagram for arsenic in As–O_2–H_2O system at 25 ºC and 101.3 kPa. Image from Nicomel et al., 2015.[42]

Inorganic arsenic occurs naturally in minerals and ores that contain sulfide, iron, zinc, copper, or lead. It forms inorganic compounds by combining with oxygen, sulfur, and chlorine, or through microbial processes in soils or sediments.[6] Although organic arsenic species, such as monomethylarsonate and dimethylarsinate may occur, their contributions to total arsenic concentrations in drinking water sources are insignificant (occurring at less than 1 µg/L).[7] The organic forms are about 100 times less toxic than the inorganic forms, with inorganic As(III) being the most toxic.[34]

1.2.1 Impacts of Climate Change

Climate change is predicted to continue exacerbating current groundwater quality problems. In the future decades, surface water sources are anticipated to greatly decline in many

areas including California while water demand increases, which will result in a higher use of groundwaters.[43] In addition to depleting resources, climate change will impact the hydrological cycle, affecting water quantity and quality. Although the impact of climate change on the geochemistry of naturally occurring arsenic in groundwater is still being investigated, it is predicted that recharge rates of groundwater aquifers and fluid flow dynamics will be affected.[43] As geogenic arsenic contamination is prevalent in fractured bedrock aquifers, rural communities relying on these sources for drinking water will be impacted. Adaptive actions and mitigation efforts may result in land use changes, which may further mobilize arsenic in bedrock groundwater. Also, long and intense drought periods are potentially correlated with increased arsenic concentrations.[43]

1.3 Existing Technologies

The main techniques that exist to remove arsenic include adsorption, co-precipitation, ion exchange, and membrane separation. They are described in the following sections.

1.3.1 Adsorption

Existing adsorption systems have been deemed as relatively low-cost methods with high removal efficiencies, being easy to operate, and not generating a sludge.[7] In this technique, arsenic binds electrostatically to charged surfaces or chemically to the sorbent. The term "sorbent", however, is generally applied for arsenic capture through either adsorption, precipitation, or co-precipitation. Conventional adsorbents for arsenic removal include hydrous metal oxides (e.g., that of iron, aluminum, titanium or zirconium), activated carbon (AC) and ion exchange resins.[41,44] AC is typically the most affordable and robust process. There are a variety of sources to create these adsorbents, such as from coal and coconut shells. The two forms of commercial ACs are powdered activated carbon (PAC) and granular activated carbon (GAC). While PAC is characterized by a larger active surface area, its separation from treated water is more challenging.[41]

Different adsorbents require different operating modes for most effective arsenic removal. Activated Alumina (AA), for example, involves the use of a porous and granular media with ion exchange properties secured as a pressurized flow-through bed. To optimize arsenic removal efficiency, a pre-oxidation step is often required if arsenic in the source water is found as As(III). Also, to operate below the adsorbent's point of zero charge (PZC), pH adjustment is also necessary.[11] The limitation of AA, a fixed adsorbent, involves its maintenance. The adsorption media must be regenerated with NaOH and a subsequent HCl rinse for positive charge restoration on the surface. However, only 50 to 80% of arsenic is displaced and there is loss of the adsorbent media in the process. Moreover, the alumina adsorbent media carries about 18 times less capacity than iron oxide sorbents.[45]

The limitations of adsorption processes includes the presence of competitive anionic species typical of water sources, such as phosphate, chloride, sulfate, or natural organic matter (NOM), which take up sorption sites and decrease overall arsenic removal efficiency.[41,42] For example, effective As(V) removal is challenging when sulfate concentrations are greater than 50 mg/L.[45] Also, adsorption columns will experience irreversible fouling after a few regeneration cycles, and thus the sorbent material will need to be entirely replaced. The disposal of the media poses a challenge due to its toxicity from the bound contaminants.[41] Also, As(III) is not effectively

removed by activated alumina. Lastly, clogging will occur if suspended solids are not removed through a pre-treatment process.[44] For example, if a high concentration of dissolved Fe(II) is present in the groundwater, a pre-treatment is required to prevent Fe(II) from oxidizing to Fe(III) and fouling the column when pumped through the system.[34]

1.3.2 Co-precipitation

Co-precipitation includes coagulation-filtration processes that require the addition of a coagulant. The coagulant acts as a catalyst for suspended, dissolved and colloidal solids to be agglomerated to form flocs, which are subsequently removed from water through gravity settling or filtration.[6,7,42] Common coagulants include ferric chloride, ferric sulfate, or aluminum sulfate. The mechanism involves adsorption and co-precipitation of As(V) to an aluminum or ferric hydroxide precipitate. The added coagulant precipitates as a ferric or aluminum hydroxide, onto which As(V) adsorbs or co-precipitates with. The aggregation of particles into flocculated precipitates is a result of the surface charge alteration from the coagulant added.[11,34]

Precipitation causes insoluble arsenic compounds to form, whereas in co-precipitation soluble arsenic species are incorporated into a polymerizing metal oxyhydroxide.[34] Increasing the coagulant dose will yield more effective arsenic removal. The advantages of chemical precipitation are that the chemicals are typically available, it is low-cost and simple to operate. The disadvantages are the generation of arsenic-laden sludge (and related disposal costs), as well as pre-oxidation requirements and post-pH adjustments. Additional post-coagulation sedimentation and filtration steps are also necessary.[7]

These coagulation-flocculation processes are well-known arsenic removal methods, but the typical coagulants used are more effective at removing As(V) than As(III). Thus, oxidation of As(III) is required to maximize removal efficiency. Oxidants such as chlorine or manganese dioxide can be applied as a pre-treatment step. Ozone is an effective oxidant but can react with NOM to yield unfavorable products. Permanganate is also effective, but requires additional post-oxidation adsorbents to remove the color it gives to treated water.[34] Additionally, this oxidation step may lead to disinfection byproduct formation or introduction of taste and odor compounds.[41] The parameters that impact performance of coagulation and precipitation processes include pH and competing ions like phosphate or silicate. Factors contributing to costs in coagulation/filtration include the coagulant type, total coagulant dose, pH and energy consumption from mixing.[11] Moreover, the selected coagulant species will govern the optimal operating mode of the system.[41]

1.3.3 Membrane Separation

Membrane separation occurs through microfiltration (MF), ultrafiltration (UF), nanofiltration (NF) or reverse osmosis (RO), which are pressure-driven processes. Depending on the pore size of the membrane, removal is achieved either through filtering out arsenic that is bound to particles, electrostatic repulsion on the charged membrane surface, or through size exclusion of hydrated ions.[45,46] RO removes salts, microorganisms, dissolved minerals, organic carbon, and color. As(V) removal rates using RO have been greater than 95%.[45] Prior to passing through a membrane, the treated water may need to be coagulated/flocculated to enhance separation, especially in MF and UF.[42]

Membrane separation can more effectively remove As(V) than As(III), at up to 99% removal as opposed to 61 – 87% removal.[7] Oxidation of As(III) to As(V) could be incorporated into the treatment train prior to the membranes, but use of oxidants such as chlorine can damage the membrane.[41] There is no selectivity of other dissolved solids over arsenic, which means that a feed water can have high complexity without it impacting arsenic removal performance. Typically membranes have a negative charge that allow for high rejection of anionic As(V) as compared to uncharged As(III).[41] The reason that MF and UF technologies also work for arsenic removal is that arsenic can be found in various size ranges, those of dissolved solids (less than 3 kDa), colloidal particles (size between 3 kDa and 0.45 μm), and particulate matter (greater than 0.45 μm). In surface waters the particulate and colloid fraction ranges from 10 to 60% whereas only up to 20% in groundwaters.[41]

The disadvantages of membrane processes include high costs due to high operating pressures, and the production of large residual volumes that contain hazardous concentrations of arsenic, and of other contaminants that remain in the reject stream.[7,11] Additionally, the degradation, or fouling, of the membrane is another limitation of the technology. Membrane fouling mitigation efforts include maintaining optimal pH levels.[11] Handling of the waste adds costs either from additional treatment of the brine or from its disposal at a sanitary sewer.

1.3.4 Ion Exchange

Ion exchange is a physical-chemical process in which a solid resin is used so that an anion, like arsenate, is exchanged with an anion on the resin phase.[11,44] Typically the solid resin will consist of a three-dimensional hydrocarbon network onto which ionizable groups are electrostatically bound.[7] Ions in solution of similar charge with a higher selectivity for the resin will exchange for existing ions bound to the resin. As(V) removal will require the use of a strong-base anion exchange resin, to exchange for bound chloride or hydroxide. This exchange will produce an effluent water with lower As(V), but higher Cl^- concentration than the feed water. The resin becomes exhausted when the exchange sites become occupied by arsenic, and other anions present in the water source, with higher exchange affinities. Sodium chloride solution is used to regenerate the exhausted resin.[7]

The limitations of ion exchange include the ineffective removal of As(III), signifying the need for a pre-oxidation step if arsenic is present as As(III). As with membranes, if residual oxidant is not quenched prior to entering the ion exchange vessel, the resin itself can become damaged. Moreover, competing anions in the influent can impact As(V) removal efficiency, especially sulfate ions which have a higher selectivity on the resin. Nitrates present in the source water can also impact performance, as well as pH and the selection of the resin itself. Also, arsenic removal will be impacted when water is brackish or contains high levels of total dissolved solids (TDS), especially above 500 mg/L.[7,38] Lastly, the generated brine is a hazardous waste that requires costly disposal methods.[11,44]

Table 1.1 summarizes the advantages and disadvantages of the various arsenic removal methods discussed above.

Table 1.1 Summary of advantages and disadvantages of existing arsenic removal technologies.

Technique	Advantages	Disadvantages
Co-Precipitation	-Low cost and simple operation -Availability of chemicals -High As(V) removal efficiency -If Fe(II) salt used, As(III) is partially oxidized -Chemical dose is easily adjusted according to water quality	-Arsenic-laden sludge management required -Pre-oxidation step may be required
Adsorption	-Many commercially available units and types of media	-Presence of co-occurring ions (e.g., SO_4^{2-}, PO_4^{3-}, organic carbon) worsen arsenic removal -pH adjustment required -Pre-treatment of suspended solids required to prevent media clogging -Generation of hazardous caustic liquid waste from regenerating media -Regular media replacement required -Management of As-laden solid media
Ion Exchange	-Commercially available units -High As(V) removal efficiency	-Presence of co-occurring ions (e.g., SO_4^{2-}, NO_3^-, F^-, TDS) worsen As removal -Not effective for As(III) removal -High capital and operation and maintenance costs -Post pH adjustment required -Effluent may contain high levels of Cl^- -Potential for breakthrough of adsorbed arsenic on resin media -Generation of high volumes of hazardous sludge
Membrane Separation	-Co-occurring contaminants removed without impacting arsenic removal efficiency -High As(V) removal efficiency -No hazardous solid waste is generated	-Not effective for As(III) removal -Membrane damaged by oxidants -High capital and operation and maintenance costs -Rejects a high volume of water

1.4 Need for a Novel Solution

The persistence of the global arsenic problem has shown that a development engineering approach through close collaboration among local communities, governments, non-profit organizations, industry, and researchers is critical to developing a sustainable solution.

The technologies discussed so far face serious disadvantages that have prevented them from serving as effective solutions for the global arsenic problem. One of the issues is scaled up appropriateness of these systems when it comes to the skill level required of operation as well as maintenance and high operation costs. Typically, the challenge is not in acquiring the resource to install the technology, but rather the business model and social placement strategy of technologies, especially in resource-constrained communities. As such, a technology that is low-cost, simple to use, and minimizes pre- and post- treatment steps is required.

In 2015, the United Nations (UN) General Assembly adopted the Sustainable Development Goals (SDGs), setting 17 specific goals and 169 targets to improve the human condition by 2030.[47] One of the goals, SDG 6, is to "ensure the availability and sustainable management of water and sanitation for all".[47] To achieve this goal in the given 15-year time span, Hering et al., 2016 recently concluded that major efforts must be concentrated on putting knowledge into practice,[48] translating technologies from the lab to field while involving key stakeholders and scaling-up for positive impact.

It is becoming increasingly incontestable that technology is not enough to solve the global arsenic problem. The scientific literature contains a plethora of lab-based studies reporting arsenic removal efficiency,[49,50] dose requirements,[51,52] and fundamental adsorbent characterization,[53,54] with perhaps some field studies.[38,55] However, there exists a gap in understanding the necessary strategies for successfully taking a technology from the lab to the field including community engagement and long-term sustainable operation. Such understanding requires the inclusion of socioeconomic aspects of technological deployments within cultural contexts.

1.5 Novel Electrochemical Technologies

1.5.1 ElectroChemical Arsenic Remediation

An emerging arsenic removal technology invented by researchers in 2006 at the University of California, Berkeley (UCB) and Lawrence Berkeley National Laboratory (LBNL) is called ECAR (ElectroChemical Arsenic Remediation).[56] ECAR is based on iron electrocoagulation (Fe-EC), in which a sacrificial iron anode is electrolytically dissolved to aqueous Fe(II) ions, which migrate from the electrode to the bulk solution. In the bulk solution, Fe(II) is oxidized by dissolved oxygen (DO) to Fe(III), forming reactive intermediate byproducts (i.e., Fe(IV) or $^{\bullet}OH$)[57] which serve to transform As(III) to As(V), the more readily adsorbed form of arsenic. After adsorption through inner-sphere surface complexation onto the generated Fe(III)(oxyhydr)oxides,[58] the solids are separated through gravity settling and/or filtration, producing arsenic-safe drinking water.[23,59]

ECAR holds many advantages as compared to other iron-based systems (e.g., zero valent iron, ferric or ferrous salts, oxidation of naturally present Fe(II)), such as its faster and more effective arsenic removal efficiency. This system is also very amenable to the specific water quality of each location as the operating conditions can be easily adjusted, such as by changing the applied galvanostatic current, I (mA), as well as increasing or decreasing the electrolysis time (t_e).

This means that the total coulombic dose can be optimized accordingly. The chemistry (i.e., production of H_2 gas at the cathode) of ECAR also gives it the advantage of pH buffering ability, as compared to conventional chemical coagulation which typically results in a product water of lower pH that then requires the addition of more chemicals to meet drinking water pH standards. ECAR produces the Fe coagulant in-situ with no need for external chemical addition. ECAR is also easy to operate, is amenable to automation, does not demand high levels of maintenance, and produces small amounts of sludge.[23] The generated sludge is also characterized as non-hazardous according to the Toxic Characteristic Leachate Protocol (TCLP) through EPA Method 1311. This means that the sludge, with an arsenic loading of 20 mg-As/g-Fe, is allowed to be disposed of at a municipal landfill in the United States. The amount of arsenic leached was 160 µg/L, much below the regulatory limit for wastewater of 5000 µg/L.[59]

The research conducted on Fe-EC over the past decade has demonstrated how effective the system is in removing high levels of arsenic in contaminated drinking water, both in the laboratory and in the field. Amrose et al., 2013 tested the arsenic removal efficiency of ECAR in a coulombic dosage rate (CDR) range of 0.06 – 18 C/L/min, corresponding to an iron production rate of 0.02 – 5.2 mg-Fe/L/min in a synthetic Bengal groundwater with initial total arsenic concentrations of 90 – 3000 µg/L, containing 50% As(V) and 50% As(III).[23] The arsenic removal efficiency (ARE) is defined as the mass of arsenic removed per unit mass of Fe(II). It was found that CDR is an important operating parameter that impacts ARE (µg-As per mg-Fe(II)). Lastly, the study showed that the ARE increased by almost an order of magnitude as the initial arsenic level increased from 90 to 3000 µg/L, a practical finding for field optimization and sustained operation.

In terms of daily operation, field trials of 100-L and 600-L systems in rural India confirmed that polarity switches of the electrodes could mitigate rust build-up. Minimizing passivation on the anode is critical to allow for the migration of Fe(II) ions to the bulk solution, which is where the arsenic removal processes take place. The 100-L field test demonstrated that ECAR can consistently remove 245 – 343 µg/L of initial arsenic to below 5 µg/L at a CDR of 2.7 C/L/min for a coulombic dose of 350 C/L.[23] The 600-L field test demonstrated continuous arsenic removal over a 3.5 month period in rural India. The ECAR product water also met WHO limits for iron (0.3 mg/L) and for aluminum (0.2 mg/L) – aluminum levels were monitored as the coagulant used was aluminum sulfate – with only gravitational settling as the separation method.

Amrose et al., 2013 also demonstrated that ECAR can effectively remove arsenic to below the MCL in groundwaters containing phosphate and silicate, which are known to compete for adsorption sites. This was verified across diverse aquifers from Bangladesh and Cambodia, reducing 760 µg/L of arsenic to below 1.1 µg/L. In terms of molecular scale mechanisms, van Genuchten et al., 2013 found that the presence of bivalent cations (i.e., Ca^{2+}, Mg^{2+}) improves arsenic removal efficiency when the iron precipitates are generated in the presence of oxyanions (i.e., PO_4^{3-}, SiO_4^{4-}). Additionally, the otherwise stable colloids that are electrolytically generated in complex groundwater matrixes can become destabilized and have improved settleability, meeting <1 NTU turbidity after 1 hour of settling.[60] Also, although increasing current density (mA/cm^2) typically decreased arsenic removal efficiency, van Genuchten et al., 2012 found that the structure of the electrolytically generated Fe(III) (oxyhydr)oxides is not significantly altered when changing this operating parameter.[58]

In addition to technical efficacy, ECAR has been developed with a socially integrated business model. Since 2010, UCB and LBNL researchers have collaborated on the social

embedding of ECAR with the Global Change Program (GCP) of Jadavpur University (JU), and later on, a local private industry group in India. ECAR was effectively deployed within the cultural context of rural India and the first large-scale plant has been in operation since 2016. This iteration of improving the technology and business model together has been a part of the ECAR development project since the beginning. As such, the technology has been designed to support a model that would facilitate rapid scale-up while integrating outreach and feedback systems along the way. For ECAR to be qualified as successful, it would need to (1) consistently produce arsenic-safe drinking water meeting local and international MCLs, (2) produce arsenic-safe water in a low cost manner to distribute at an affordable price, (3) ensure ease-of-use and robust performance in the field, (4) prevent any secondary environmental risks and low operator risk, and (5) be socio-culturally acceptable to the local community.[59]

1.5.2 Air Cathode Assisted Iron Electrocoagulation

Although ECAR has been deployed in India, it is inherently technically limited for wide adoption in the U.S. because of slow chemical kinetics.[23] The first large-scale ECAR plant only produces arsenic safe water for drinking water purposes for about 5,000 people, while taking up a 1,400 ft^2 spatial footprint. In the U.S., municipal water systems must provide the same quality of water to households for all uses including drinking, preparing food, bathing, washing clothes, household cleaning, and toilet use.[61] For a small community water system (serving 10,000 or fewer people) in California, the average demand is 1.4 million gallons per day (MGD).[38] Also, adsorbent based processes tend to be favored as flow-through column filters[38] as opposed to large batch reactors, like ECAR.

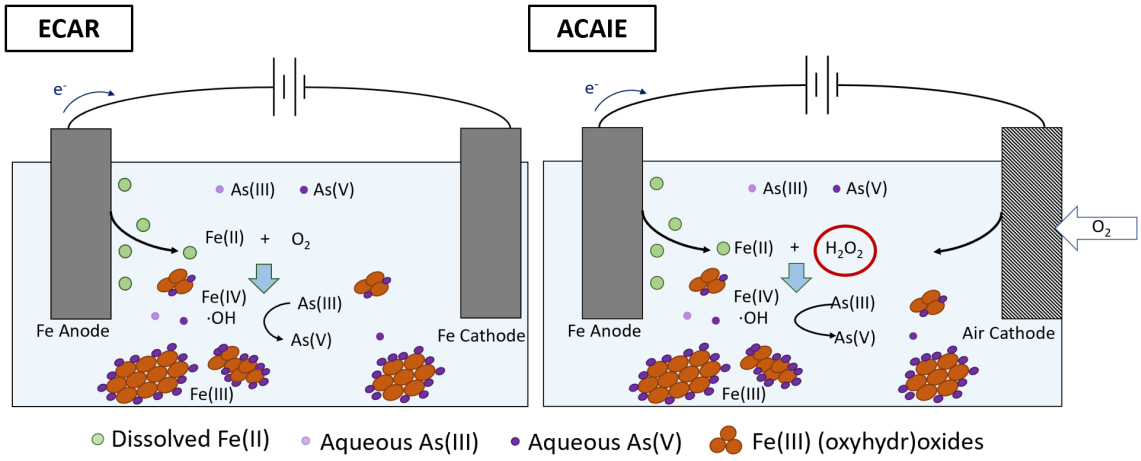


Figure 1.5 Schematics of ECAR and ACAIE. The major difference is the oxidant reacting with Fe(II). ECAR relies on the recharge of oxygen into the bulk solution. ACAIE does not depend on DO because the system generates H_2O_2 in-situ, which reacts more quickly with Fe(II), or by four orders of magnitude.[62] Owing to its faster chemical kinetics, ACAIE reactor is also more compact relative to ECAR reactor for the same throughput rate of treated water.

Our recent research to improve ECAR has led us to discover the superior performance of carbon-based air-diffusion cathodes[63] that speed up the reactions of Fe-EC towards removing arsenic from contaminated water while reducing the energy consumption of the process. The resulting treatment systems are more compact,[64] and ultimately avoid requirements of large space and energy intensive aeration. This next-generation ECAR system is called ACAIE (air cathode assisted iron electrocoagulation). The ability of ACAIE to achieve high throughput rates and meet

water demands in California is dependent on its fast chemical kinetics. To understand why ACAIE can be designed as a more compact system than ECAR, the chemical processes of the systems are compared side by side in Figure 1.5. Both ECAR and ACAIE are based on the electrolytic dissolution of a sacrificial iron anode, but only ECAR relies on the presence of dissolved oxygen (DO) for subsequent reaction pathways to take place. The limiting step of ECAR is:

$$1.\quad Fe(II) + O_2 \rightarrow Fe(III) + O_2^{\cdot -}$$

The diffusion rate of O_2 from the atmosphere dictates how fast ECAR can be operated, or how high of a CDR can be applied to quickly generate Fe(II) ions. Amrose et al., 2013 demonstrated that arsenic removal efficiency declines in ECAR as the CDR increases above 0.06 C/L/min (i.e., poor performance at 2.2, 10, and 18 C/L/min). Generating Fe(II) at a faster CDR in ECAR leads to accumulation of Fe(II) ions in the bulk solution, depleting DO.[57] The accumulated Fe(II) also competes with As(III) for reactive intermediates (i.e., Fe(IV) and $^{\bullet}OH$) leading to a decrease in arsenic removal efficiency. As a result, a higher total coulombic dose (D), or greater concentration of Fe(II), is necessary to decrease arsenic to safe levels when attempting to operate ECAR at a faster throughput rate.[23] D is proportional to the concentration of Fe(II) generated in the system (in mol/L), or during electrolysis, through Faraday's Law:

$$2.\quad [Fe(II)] = \frac{D}{n*F}$$

where D is the coulombic dose in C/L, n is the number of transferred electrons (n = 2 for this system), and F is Faraday's constant of 96,485 C/mol. While the reduction reaction at the cathode in ECAR is H_2 evolution (which is beneficial in maintaining a pH buffered system), ACAIE utilizes the cathode to overcome ECAR's limiting step through the oxygen reduction reaction (ORR) and generate hydrogen peroxide. The relevant half reactions at the Fe anode and carbon-based air diffusion cathode, respectively, are listed below:

$$3.\quad Fe(0) \rightarrow Fe(II) + 2e^-$$
$$4.\quad O_2 + 2H^+ + 2e^- \rightarrow H_2O_2$$

The replacement of H_2O_2 for DO from the atmosphere as the oxidant allows Fe(II) oxidation kinetics to be accelerated by nearly four orders of magnitude.[65] Thus, ACAIE achieves rapid Fe(III) (oxyhydr)oxide generation directly in water without the need for aeration (leveraging for a compact reactor) or subsequent mixing steps. Bandaru et al., 2020 demonstrated the efficacy of arsenic removal from synthetic Bengal groundwater at circumneutral pH using ACAIE as a 0.5 L batch system.[66] ACAIE consistently lowered high initial As(III) concentrations of 1500 µg/L to much below 10 µg/L in as short as 30 second treatment times. ACAIE was also tested as a 60 liter per hour (LPH) system in the field treating 100 L of real California groundwater, reducing initial 118 µg/L of arsenic to below 0.5 µg/L. The short resident time of ACAIE indicates the potentially much smaller capital costs for the system as compared to ECAR, and its capacity to serve low-income, rural communities facing arsenic contamination in their groundwater.

1.6 Outline of Remaining Chapters

The organization of the remaining chapters in this dissertation is as follows.

Chapter 2 identifies and explains the key strategies in taking ECAR from the lab in Berkeley to the field in rural India. A new term, the Critical Effort Zone (CEZ), is introduced and

defined as the efforts exerted as part of an international, multidisciplinary team while commissioning the first large-scale ECAR plant. The high-priority efforts undertaken in this time period include ensuring a context-sensitive technology design, bridging the knowledge divide between researchers and the community, creating local job opportunities, and following specific local regulations. The lessons learned from the 6-month field work, but as of a larger culmination of 12 years of technology development, are discussed for broader application to other projects. Lastly, the implications of ECAR scale-up towards the Sustainable Development Goals (SDGs) are addressed in this chapter.

Chapter 3 elucidates the arsenic (As) and manganese (Mn) removal performance of ACAIE in wide pH and coulombic dosage rate ranges in a complex synthetic California groundwater matrix based on samples from the Central Valley and from publicly available data. We utilized X-ray Absorption Spectroscopy (XAS) to characterize the electrolytically generated reaction products. By collecting As, Fe, and Mn K-Edge X-ray Absorption Near Edge Spectroscopy (XANES) spectra we determined oxidation states as well as quantified the presence of each species through Linear Combination Fits (LCFs) with appropriate reference spectra. Using the As and Fe K-Edge EXAFS (Extended X-ray Absorption Fine Structure) spectra, we analyzed the data through shell-by-shell fits. This allowed us to determine the local coordination geometry of sorbed As onto the highly disordered iron (oxyhydr)oxide phase.

Chapter 4 focuses on the performance of the carbon-based air diffusion cathode in ACAIE after repeated use. The Faradaic Efficiency of H_2O_2 production is employed as a key metric for overall system efficiency. Moreover, various characterization techniques (i.e., X-Ray Diffraction (XRD), Scanning Electron Microscopy (SEM), X-ray Photoelectron Spectroscopy (XPS), and Raman Spectroscopy) elucidate morphological changes, elemental composition, and the catalytic sites on the cathode surface that promote the oxygen reduction reaction. These results provide molecular-scale insights to degradation mechanisms and inform approaches to increase the lifespan of the electrode during field testing.

Chapter 5 summarizes the key finding of this dissertation and highlights how community outreach efforts are key components to the technology development and deployment process. This chapter also points towards remaining research questions that would provide greater understanding of ACAIE technology, as well as the broad applications of electrochemical technologies for decentralized uses in small and rural communities.

Chapter 2. Strategies for Successful Field Deployment in a Resource-Poor Region: Arsenic Remediation Technology for Drinking Water

Adapted with permission from Hernandez, D.; Boden, K.; Paul, P.; Mypati, S.; Roy, A.; Amrose, S.; Roy, J.; Gadgil, A., Strategies for successful field deployment in a resource-poor region: Arsenic remediation technology for drinking water. *Development Engineering* **2019**, 4, 100045. DOI: 10.1016/j.deveng.2019.100045

2.1 Introduction and Background

Drinking water is deemed unsafe if it contains more than 10 parts per billion (ppb) of arsenic.[4] Even at this provisional guideline value, or maximum contaminant level (MCL), the excess cancer risk from lifetime exposure to arsenic is 700 per 100,000 people.[13] This lifetime cancer risk is about 60 times larger than the next highest lifetime cancer risk, which is linked to ethylene dibromide, in rank-ordered risks from consuming water with carcinogens permitted in water at their respective MCLs. Besides cancer, other health impacts of chronic exposure to arsenic include skin lesions, gangrene, cardiovascular diseases, and possible reduction in children's IQ.[3] Health damages resulting from chronic exposure to high levels of arsenic add a huge health-cost burden on resource-poor communities in West Bengal, India.[67]

Despite large expenditures by multilateral, bilateral, and national government programs[68], previous technology-based efforts to address the arsenic problem proved unsustainable in resource poor communities such as rural South Asia. This devastating fact emerged from research which looked at arsenic remediation technologies employed in one of the most arsenic-affected districts of West Bengal: the Murshidabad District. In this district, 93% of seventy implemented arsenic removal technologies failed within one to eight months.[28] Household- and community-scale arsenic treatment units installed in West Bengal, India during the past decade typically became dysfunctional within one year of installation due to multiple reasons.[27] In a water supply program for arsenic mitigation in Bangladesh, attempted solutions included dug wells, pond sand filters, rainwater harvesting, deep tube wells, piped water, and arsenic removal filters. The installed household arsenic removal filters were ineffective in removing arsenic and were abandoned after a few months.[69]

Technologies do not work in a vacuum. They have dozens or may be hundreds of threads connecting them to invisible social constructs such as belief systems, expectations, institutions and cultural norms, systems of incentives and disincentives, competing resource demands, and priorities of political and social hierarchies. Although external agencies were often willing to invest in remediation projects in resource-poor regions, those invested solutions proved to be unsustainable because they were not installed with a corresponding long-term sustainable societal placement strategy.[27,70] While proximate reasons for project failure include lack of maintenance, improper operational training, and cultural insensitivity, ultimate or deeper reasons include partisan politics, lack of genuine public consultation, lack of understanding of legal structures, and absence of sustainable business model-frameworks.[27,71,72]

Such continued poor results, despite the continued expenditure of effort and funds, suggest that scholarly research may shed light on what goes wrong with such efforts and why such failures

continue to be repeated. The progression of ElectroChemical Arsenic Remediation (ECAR) from an effective bench-top laboratory beaker at University of California-Berkeley (UCB) and Lawrence Berkeley National Laboratory (LBNL), to a prototype in small field tests in West Bengal, India in collaboration with Global Change Program of Jadavpur University (GCP-JU), to a full-scale pilot plant with additional collaboration with a local industry partner, offers a case study of addressing some common challenges that arise during the advanced stage of the innovation chain. During this advanced stage, the technology needs to be scaled-up for an intended community for long-term sustenance, which requires social acceptance of the new technology.

The deployment of ECAR addresses the major global health crisis resulting from arsenic exposure in contaminated drinking water. Moreover, the United Nations has created a set of sustainable development goals (SDGs) which seek to meet milestones for human well-being.[47,73] Addressing and mitigating the detrimental health and socioeconomic effects of arsenic will ultimately help meet the SDGs by the intended deadline of 2030. Thus, the deployment of ECAR, and this unique social placement strategy contribute to several of the 17 SDGs.

This paper presents the technical and social obstacles that were overcome during the case study to deploy the most recent and largest version of ECAR—a pilot plant with 2,500-liter reactors, with the capacity to produce 10,000 liters per day (LPD) of safe, affordable drinking water in a rural village in India. It is important to note that this is a case study, not a hypothesis testing effort. The latter requires a randomized trial with a large number of controlled experiments, and has its own value. In contrast, a single case-study can be hypothesis-generating, based on observations and experiences of the researchers from intense long-term efforts such as the one reported here.

2.2 ECAR: From Lab to Field

ECAR was invented in 2006 at LBNL and from 2008 onward developed at UCB. Information gathered during the past 13 years of the ECAR scale-up project, some of it in collaboration with Indian scientific collaborators, has resulted in a deep understanding of the process.[59,74–76] This technology has matured, scaling-up in successfully larger designs from a 0.2-liter beaker (in 2006) to a 10,000-LPD pilot plant (in 2016), as illustrated in Figure 2.1.

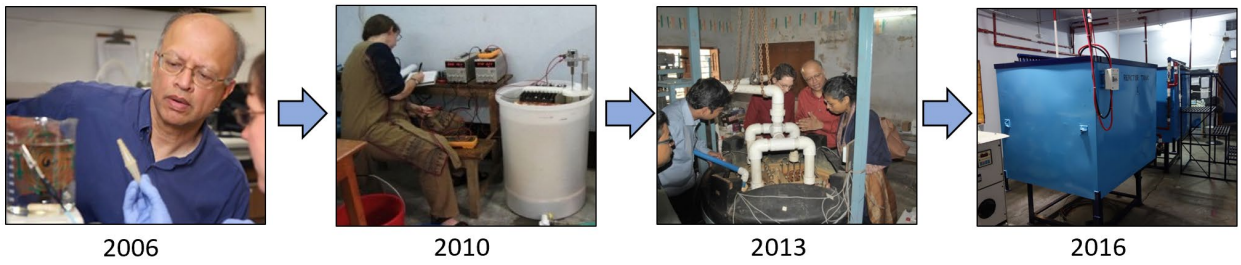


Figure 2.1 Over the course of 10 years, ECAR scaled successfully and progressively from a 0.2-liter beaker, to 100-liter and 600-liter prototypes, to a 10,000-LPD capacity field pilot plant.

During the ECAR process, a small voltage applied to steel plates immersed in arsenic-contaminated groundwater leads to the anodic dissolution of Fe(0), to produce Fe(II) ions. These ions then diffuse into the water being treated. In the water, the Fe(II) ions react with dissolved oxygen (DO) and convert into insoluble oxyhydroxides of Fe(III). Before completion, however, this complex oxidation process forms an intermediate byproduct: highly reactive intermediate

oxidants (Fenton-type products). These effectively oxidize non-ionic As(III) to readily adsorbed As(V) oxyanion.[23,57,62,74] The insoluble Fe(III) ions polymerize *in situ*, producing Fe(III) (oxyhydr)oxides with a high affinity for binding As(V).[58] In a subsequent step, the As-laden precipitates are separated from treated water by flocculation and sedimentation. In previous work in laboratory and field environments, ECAR reliably lowered initial arsenic concentrations between 90 and 3,000 ppb in typical synthetic and real groundwater matrices from Bangladesh, India, and Cambodia[23] to below the World Health Organization (WHO) guideline value of 10 ppb. Further fundamental science on ECAR will not be repeated in this paper, which focuses on the holistic aspects of implementation in the field.

2.2.1 The First Large-Scale ECAR Plant

The pilot plant has a spatial footprint of 1,400 ft^2 and is situated in a classroom on the south end of Dhapdhapi High School in West Bengal, India. The plant is set up in two adjoining sections: the ECAR Room and the Tube Settler Room (Figure 2.2). A control board (Figure 2.4b) in the Tube Settler Room supplies power to all parts of the plant.



Figure 2.2 Digital photographs of the 10,000 LPD capacity pilot plant at Dhapdhapi High School. a) ECAR Room: Contains the two ECAR reactors in which electrolysis occurs b) Tube Settler Room: Contains the tube settler, flocculation chamber, and subsequent tertiary treatment systems for particle separation.

The schematic below depicts the treatment train at the pilot plant (Figure 2.3). The influent water has an average arsenic concentration of 252 ± 29 ppb and is pumped from the school's shallow tubewell of 32 meters in depth.

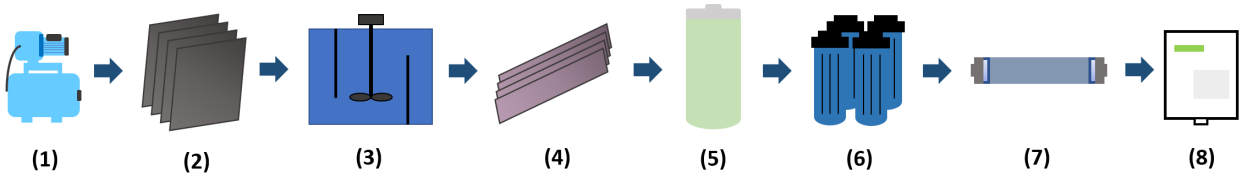


Figure 2.3 Schematic representation of the treatment process at the Dhapdhapi pilot plant: 1) raw water pump, 2) ECAR reactors, 3) flocculation chamber, 4) tube settler, 5) rapid sand filter, 6) micron filters, 7) ultraviolet disinfection system, 8) automatic dispensing unit.

The arsenic-bearing groundwater flows into two 1,250-liter tanks where the ECAR process occurs. After delivering a specified Coulombic dose to the water using a custom-designed power

supply (Figure 2.4a), treated or iron-dosed water is transferred to the first holding tank. A flocculation chamber aids in floc formation and agglomeration, and a subsequent tube settler allows the floc to settle out as the water flows up through angled media. Under normal operation, the tube settler achieves less than 5 nephelometric turbidity units (NTU) in the effluent water. Subsequent tertiary treatments include a rapid sand filter, a set of polishing filters and a disinfection step with an ultraviolet light. The final processes ensure that ECAR product water is both aesthetically pleasing and free of any potential biological contaminants. The process from groundwater pumping to ultraviolet (UV) disinfection consumes about 2.3 kWh of energy per m^3 of water treated. Finally, water is transferred to overhead tanks in the school courtyard where automatic dispensing units (ADUs) are placed for water access by students, teachers, and staff. The water access is based on an understanding made with the school authorities at the start of the pilot project, that if the project is successful, in exchange of permission granted for use of indoor and outdoor space for the ECAR plant, the school's students, teachers and staff will all receive free arsenic-safe potable drinking water.

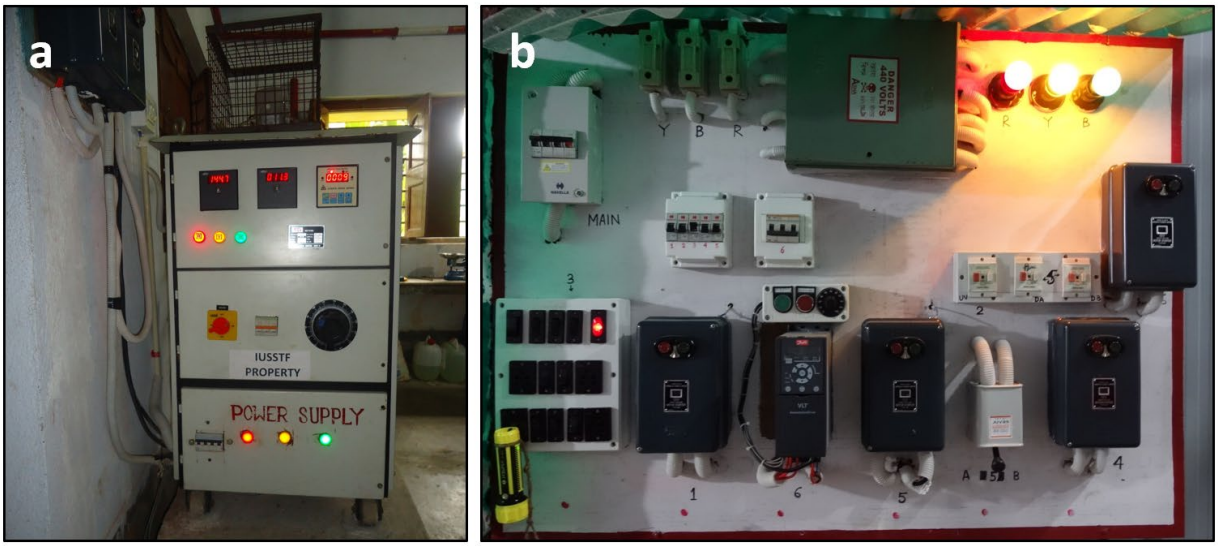


Figure 2.4 a) ECAR Power Supply: Supplies the current to the two ECAR reactors in order for electrolysis, or the dissolving of the iron anodes, to occur. b) Main Circuit Board: Located in the Tube Settler Room, the main electrical board provides power to the entire plant.

The Dhapdhapi plant was operated consistently by local operators, employed by the industrial licensee (Livpure Ltd), under technical supervision from UCB field engineers, five days a week, from April 2016 to January 2017. Previous field trials of ECAR in India had demonstrated that a semi-skilled person (with high school education) can effectively operate the plant after appropriate training from the technical staff.[59] During the April 2016 – January 2017 period, bi-weekly samples of raw and product water were collected and sent to UCB to test for arsenic and other relevant elements using inductively coupled plasma atomic emission spectroscopy (ICP-OES), and ICP-OES with hydride generation for arsenic levels below 10 ppb. Raw water parameters, including the ion concentrations relevant for arsenic removal efficiency, are shown in Table 2.1. Phosphate and silicate are known to compete with arsenic for adsorption sites on iron oxides, while calcium and magnesium aid in arsenic removal.[58,77] Moreover, the effects of pH and

redox potential on arsenic removal are not investigated in this paper, but such conditions and mechanistic understanding are found in previous literature.[78,79]

Table 2.1 Raw water average element concentrations as tested by ICP-OES at UC Berkeley.

Element	Concentration	Unit
As	250 ± 14	ppb
Fe	15.5 ± 0.4	ppm
P	0.61 ± 0.9	ppm
Ca	80.4 ± 3.5	ppm
Mg	40.8 ± 1.0	ppm
Si	17.2 ± 0.5	ppm

To comply with local norms necessary for obtaining national accreditation in India for technology operation, weekly product water samples were collected and measured for arsenic by two National Accreditation Board Laboratories (NABL), both of which used ICP-MS, and each of the laboratories had been earlier separately validated by sending them calibrated unlabeled samples. Product water samples were also tested monthly to ensure compliance with the full Indian Standard IS10500:2012 for drinking water for all physical, biological and chemical properties in the standard.[22] Throughout the entirety of this period, ECAR's field performance showed reduction in arsenic concentrations from initial 252 ± 29 ppb, to final arsenic well below 10 ppb, and often below 5 ppb (average 2.9 ± 1 ppb) as seen in Figure 2.5. After five months of ensuring the water met consistently all drinking standards, the water was made available to the 2,500 students, staff, and teachers of Dhapdhapi High School. Currently (as of October 2019) the plant continues in stable and active operation under control of the industrial partner (Livpure Ltd), serving arsenic-safe water daily through a financially viable business model to the local community.

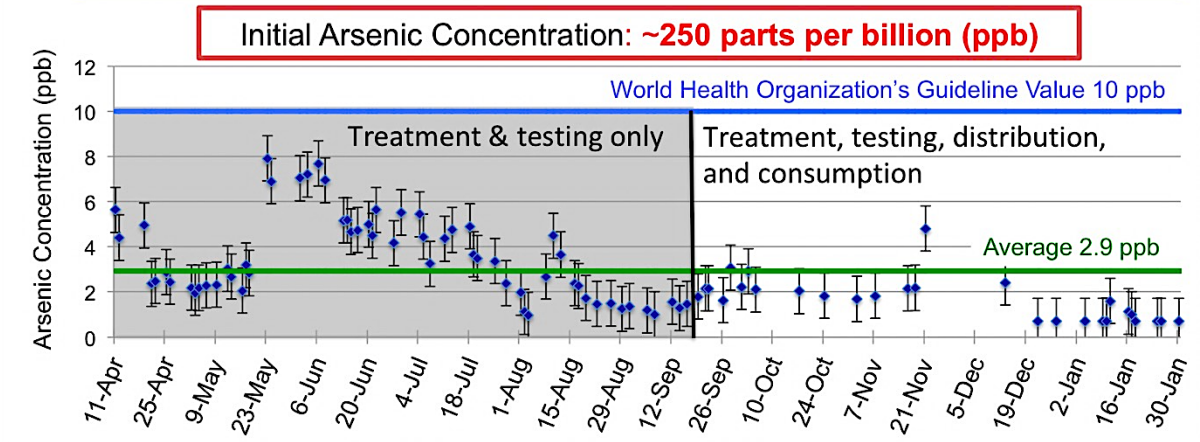


Figure 2.5 Results from the plant in West Bengal, India, from April 2016 to January 2017, depicting continuous effective arsenic removal to less than 10 ppb during both pilot and distribution phases. The spike in arsenic concentration around 23-May and excellent performance after 1-Aug are explained in Section 2.4.1.

2.3 Critical Effort Zone

Deploying the 2,500-liter ECAR pilot plant as a community-scale water access technology within rural India required persistent experimentation within the socio-cultural context. The concept of the "Critical Effort Zone" is introduced as part of the innovation chain that is commonly defined, and both are shown in Figure 2.6. The Critical Effort Zone matches the period in the innovation chain for which the expected cash flow of a project reaches its largest negative value. In the social embedding process of technology maturation, this zone requires intense efforts for trust building with key social actors, and ultimately, for acceptance of the technology by the society that will use the innovation. These efforts require understanding of human behavior, strategic planning and deep scientific understanding of the local social context. If efforts during this period are unsuccessful, the innovation can stagnate or perish. In contrast, if the efforts are successful, the technology may move towards commercialization and scale-up. The Critical Effort Zone necessitates the participation of a locally reputed and trusted scientific partner. The team can then deploy and implement strategies to build local capacity beyond the large prototype phase, and aim for long-term sustainability of the project beyond the pilot plant completion.

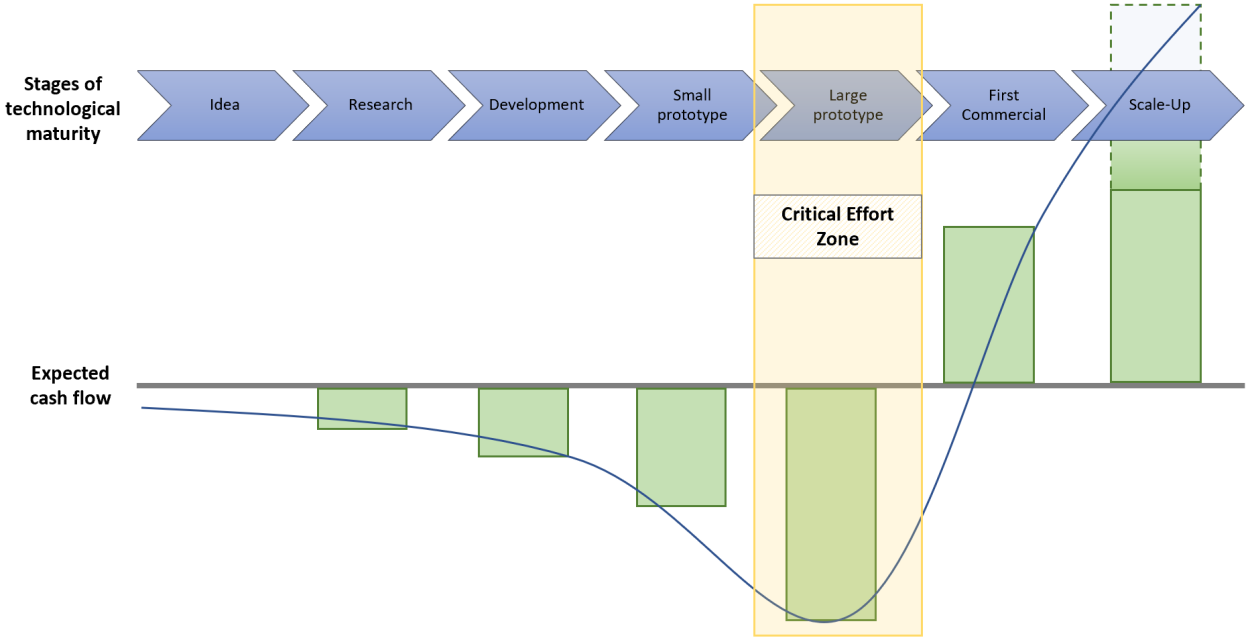


Figure 2.6 Navigating the innovation path. The Critical Effort Zone requires more than technology efficacy—acceptable social placement within unique environmental contexts is also necessary. This figure is modified from a presentation to the United Kingdom parliament[80] and public presentations about technology-maturation programs at the U.S. Department of Energy.

As one might expect, the duration of the Critical Effort Zone varies from project to project, but it is generally concluded with the demonstration of the first large-scale prototype. The Critical Effort Zone consists of successful operation of the field pilot, well designed communication to the public by the scientists in field operations, and flexibility towards any technology redesign needed to fit cultural practices. The actions taken during this zone must ensure good fit of the technology to the market needs, or "Product – Market Fit",[81] and must build the technical, managerial, and financial (TMF) capacity for a transition to commercialization. For this project, the Critical Effort Zone stretched just over 4 years (Dec. 2012 – Jan. 2017), during which the project team with its own secure project funding worked closely with a rural community in India suffering from arsenic contaminated groundwater to deploy and socially embed the first ever large-scale ECAR pilot plant, and deliver arsenic-safe drinking water to the first few thousand people daily for long-term health security.

Based on the team's decades-long experience, a prerequisite to cross the Critical Effort Zone requires secure financial support, and formal agreements documented indicating full commitment among the technology's inventor(s), local scientific partner(s), and the local industrial partner/commercial license holder. Commitment among partners includes transparency, knowledge sharing, sharing of financial costs, and field work time. Manufacturing and project objectives are agreed upon by all parties and preceded by multiple virtual and face-to-face meetings to clarify doubts and queries, and to build trust among partners avoiding false promises. In the ECAR project, all parties needed to be involved together in the larger-scale design and address all anticipated threats and opportunities. UCB provided adequate training about ECAR fundamentals and operation to the local science-technology partner and the industry partner. A 600-liter ECAR prototype pre-tested in the field[59] was re-installed in the scientific partner's

laboratory for day-to-day training, capacity building, and to generate teaching and research interest in the technology. The industry partner (Livpure Ltd) in this project was an integral part to the commercialization of affordable, arsenic-safe drinking to the local community surrounding the pilot plant.

The first step in the Critical Effort Zone was selecting an acceptable site with promise for long-term hosting of the water treatment plant if it was successfully installed. Based on past[27] and field experience[59,75] the team determined four criteria for an ideal location: 1) measured high arsenic concentration in the groundwater, 2) absence or serious inadequacy of piped municipal water supplies, 3) clear and strong support from the school administration and governing council as local champions for the project, and 4) in-kind support through allocation of sufficient space and other resources (i.e., water, electricity, and security) to conduct the work. A previous school site had proven unsuccessful because the location was too far to maintain daily visits from collaborators based in Jadavpur University (JU) in Kolkata. In addition, the team lacked at this time an industry partner, and the school administration lacked the patience to support the project experimentation. As the demands of those school officials could not be met, the ECAR prototype was removed and reinstalled at the JU laboratory.

A school in Dhapdhapi—a village outside of Kolkata, in West Bengal, India—met the above four criteria for project location. Over a year of water testing at the NABL-certified facility of the Public Health Engineering Department (PHED) demonstrated a clear need for groundwater remediation—arsenic concentrations ranged between 150 – 300 ppb. Other reasons for choosing this site location included: 1) the local research team's familiarity with the geographical region and cultural practices, 2) positive political will (created through formal and informal articulation of the IUSSTF project expectations, and funding availability) among the stakeholders at various levels in the school, surrounding community and local government administration from top to bottom, and 3) confirmation of interest obtained through consultations, focus group meetings, and pre-tested formatted questionnaires. The JU research team practiced patience and care while introducing the ECAR project and surveying the community. Communities in arsenic exposed districts of West Bengal confirmed the economic benefit and individual interest in purchasing arsenic-safe water[67,82] that ECAR could provide.

Lessons from past projects indicated that grant-funded projects fail quickly after funds are spent, unless there is long-term financial viability built *a priori* into the project structure beyond the initial grant period.[27] In the business world, the conceptual framing of a financially viable business operation is captured into a "business model". For this ECAR project, the team developed a business model to achieve financial sustenance beyond the IUSSTF-funding period (which ended in 2016). In this model, the potable water produced would be provided free of charge to the students, staff, and teachers of Dhapdhapi high school in exchange for indoor space and access to resources (i.e., electricity, raw water, and security). After the hand-off of the plant from the research team to the industry partner, the industry partner would sustain plant operation and maintenance costs by selling the excess water at an affordable price to the surrounding households (at less than 1 cent per liter). The latter was determined through an on-site survey of the community's willingness to pay (WTP) under the project, and through comparison with observed household spending on safe drinking water.[82,83] The industrial partner acquired a license for the patented ECAR technology from the University of California — to have a legal basis for commercial use of the technology, and its future commercial expansion. Thus, from the start, the

industrial partner had "skin in the game" and was exposed to some financial risk if the project failed or stood to gain if the project succeeded.

2.4 Critical Effort Strategies

This paper presents four critical effort strategies to address the penultimate barriers to successful social placement of community-scale technologies. Critical effort strategies that address contextual challenges during the Critical Effort Zone are termed as 1) appropriate design of community-scale technology, 2) increasing economic opportunity, 3) bridging the scientific knowledge divide, and 4) local legal compliance. All four activities were conducted in parallel, not sequentially.

2.4.1 Community-Scale Technology Design

In resource-poor areas of developing countries, a community-scale technology such as ECAR requires social trust and acceptance to be sustainable.[71] To gain this trust and acceptance, the local research team repeatedly visited the site and formally explained the project objectives. As a community is made up of diverse individuals with diverse interests, behavioral response patterns become equally diverse. These behavior patterns must be in alignment for a technology to be accepted. This condition is different from a private-sector technology buy-in that is focused on the individual or household consumers. Individual technologies (e.g., mobile phones) target individual behavior for incentives and promotion materials. Community-scale technologies, on the other hand, demand greater social placement efforts than an individual-scale technology.

The technical field trial was separated into three phases: 1) design, fabrication, assembly, and testing of pilot plant, 2) pilot plant continuous operation and testing of product water, and 3) pilot plant continuous operation and distribution of arsenic-safe water for consumption as drinking water. Interdisciplinary collaboration was necessary for effective integration of the ECAR project into the Dhapdhapi community. The three partners (UCB, GCP-JU, and industry partner) contributed insights into socio-cultural nuances at the site location, legal issues, marketability of ECAR, and the technology development itself. Manufacturing ECAR reactors was assigned to a trusted third-party small-scale manufacturer under close and direct supervision of field engineers from Berkeley. Researchers (both international and national) and the industrial partner oversaw installation and necessary modifications. The ECAR plant was commissioned using locally sourced materials and trained local plumbers as plant operators, offering a sustainable approach to safe water access.

This ECAR field trial served as a social placement experiment while simultaneously resolving engineering problems that were not anticipated from laboratory-scale studies. At lab-scale, ECAR is operated under controlled conditions (e.g., fully controlling the pH, dissolved oxygen, initial arsenic concentration and co-occurring ions) with a reliable supply of electricity. In the field, ECAR must be capable of operating with many unknowns, such as intermittent power supply and week to week variability in raw water quality (e.g., with rainfall or dry weather, and seasonal temperature swings). The temperature in West Bengal, India reaches high levels in the summer, accompanied by heavy rain and high humidity. Winter is moderate and dry. Such extreme seasonal variation influences the performance of the treatment train in the ECAR pilot plant.

After a year of completing the manufacture and installation of the pilot plant, the electrical components of the ECAR reactors and power supply experienced overheating and occasional

melting. The electrical connections to the electrode plates in the ECAR reactors became loose, which induced overheating and burning of the plastic on the wires (Figure 2.7). The aluminum nuts, bolts, and lugs that had been used for connecting the cables to the busbars were replaced with copper material insulated with heat shrinkable rubber sleeves. Secondly, the busbars, which distribute current from the power supply to the ECAR electrode plates, made of aluminum had to be replaced with electrical grade copper busbars.

Third, to ensure future ease of cable replacement, all cables were dug out from underground conduits and re-installed near the ceiling on a cable tray (Figure 2.8, Figure 2.9, and Figure 2.10). These cables were initially routed via underground piping to avoid tripping hazards and protect them from wear and tear. However, we observed repeated burning or melting of their plastic insulation at the connection point to the polarity switch – this was caused by contact resistance from corrosion that developed at the connection point. This turned out to be a maintenance challenge since the cables had to be repeatedly trimmed to remove the corroded ends and became shorter than the required length. About 16 meters of cable tray was hung above the power supply unit to allow an overhead path for the power cables to connect to reactor tanks 1 and 2 via two trays, which avoids keeping the wires tightly bound together. The tray continues to serve as a tripping hazard prevention and avoids cable wear and tear from traffic. The results were a reduced voltage drop in the electrical system and reduced heat generation in the wires and at the polarity switch junction.

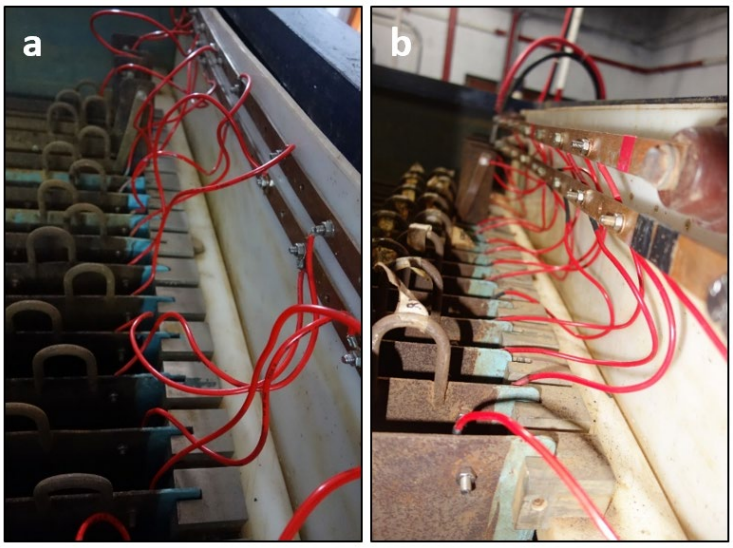


Figure 2.7 a) The busbar connections of the 6-mm wires, each wire connecting one of the 16 plates (total 32 plates in total 2 reactors) to a busbar, were all initially placed facing away from the reactor wall, thus, making them susceptible to daily accidental yanks and pulls while electrode plates were brushed, and therefore causing fraying at the connection to the busbar. b) After rewiring for improved performance, the connection of each wire is now placed facing the reactor wall, avoiding direct physical pull on the connection, and avoiding any sharp angles that would cause stress at the wire ends.

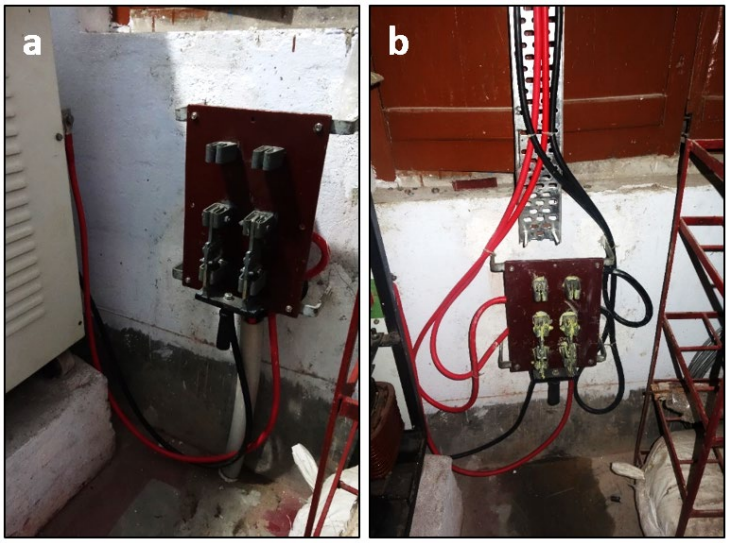


Figure 2.8 a) The red and black cables connect the polarity-reversal switch to the miniature circuit-breakers of the reactor tanks 1 and 2. b) In the reviewed layout, new black and red cables connect the polarity-reversal switch to the reactor tank miniature circuit breakers. Excess wiring was given in case of future heat damage that may also require trimming the cables and securing them again with a new copper lug. However, that has not happened owing to the corrosion inhibitor that has been applied to the folded copper busbars.

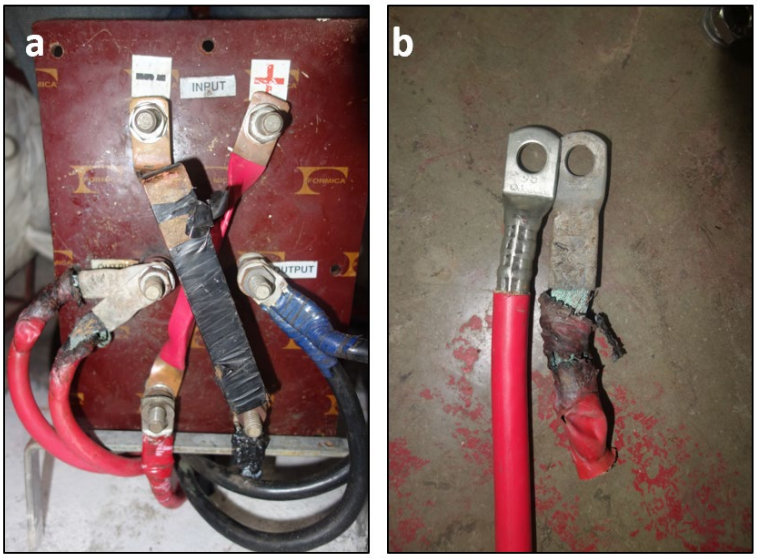


Figure 2.9 a) Components of the polarity switch showing burned insulation from overheating. b) A new lug (left) compared to the previous burnt-insulation lug (right). On the burnt insulation, the (green) corrosion of the copper wires is visible. New copper 95 mm lugs were placed on the 70 mm^2 wires, and new heat shrinkable rubber slip tubes of higher quality were placed on the two cross-over bars in the back (not pictured).

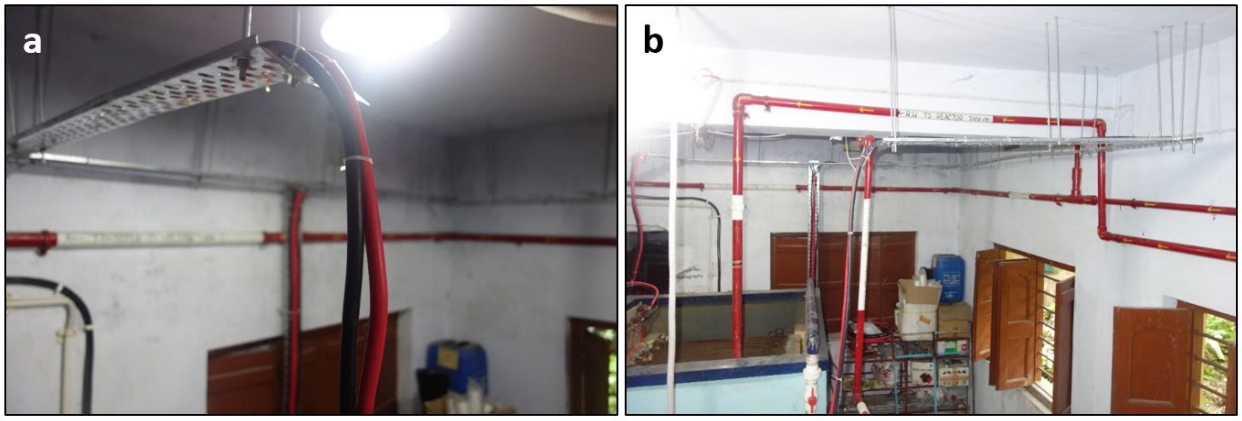


Figure 2.10 a) Cable tray leading towards reactor tanks. b) Red and black wires guided down from the cable tray to the miniature circuit breaker of reactor tank 1, and to the polarity switch where the wires from reactor tanks 1 and 2 meet.

The plant also experienced numerous power outages during the summer and monsoon seasons. Although ECAR's arsenic removal efficiency is resilient to intermittent power supply, outages do cause delays in water production. This was mitigated by installing adequate storage capacity for ECAR product water. Storage tanks were installed at a height to allow adequate gravity flow to the distribution points (Figure 2.11).



Figure 2.11 The two white-colored holding tanks were placed directly above the automatic dispensing units where drinking water is collected.

During normal plant performance, the tube settler produces water at less than 5 NTU. However, as the weather cools down in autumn through winter, the effluent turbidity from the tube settler unexpectedly reached levels as high as 30 – 50 NTUs. This was discovered through regular monitoring of the water for various parameters through multiple sampling ports. In winter, groundwater is warmer than the ambient-temperature water stored overnight in the tube settler. The inverted temperature gradient inside the tube settler caused a short circuiting of the settling flocs. To alleviate this issue, the scientific research team determined that during winter the groundwater must be pumped the night before and stored in the ECAR reactors as to cool it down to ambient temperatures. This avoids the unexpected failure of the tube settler operation.

Although the plant produced water meeting all drinking water quality parameters by the end of 2015, the research team resisted pressures to immediately distribute water for human consumption. The research team needed to first acquire extremely high confidence in long-term operation of the plant by monitoring final arsenic concentration over a ten-month period. Starting April 2016, product water was monitored weekly for arsenic, and monthly for all drinking water parameters (IS:10500:2012), i.e., physical, chemical, and biological contaminants. Samples were sent to UCB and NABL labs in India. In the second month of monitoring, the research team observed an unexplained spike in arsenic concentration of 7.9 ppb on 23-May-2016 (Figure 2.5). After several weeks of effort, the spike was traced to the operator shutting down the recirculation pumps in the ECAR reactors blaming the high level of pump noise interfering with the operator's personal cell phone calls. After this problem was resolved, the arsenic levels declined, but remained higher than expected (though always below 10 ppb). The research team traced this to lack of deep cleaning of electrodes since start of operations in 2014. Deep cleaning is a regular maintenance process performed semi-annually which involves removing the electrode plates from the reactors and mechanically removing the surface layers. This is different from regular cleaning of the plates, which is performed daily with hard wired brushes between the electrodes in each reactor. After deep cleaning the electrodes in late July 2016, the arsenic levels in the finished water returned to the expected level.

Only in mid-September 2016, the research team allowed the water for distribution to school children, teachers, and staff. Everyone could now receive 30 liters of free arsenic-safe water per month, after submitting proper written signed consent forms, either self-filled (for adults), or filled and signed by the guardian (for students). The finished water continued to be monitored and data is shown in Figure 2.5 until January 2017 when the plant's operation was fully handed over to the industrial partner. Since then, the industry partner sustains the plant financially by operating the plant for 22 days a month, and selling water at INR 6 per 10 liters to the nearby community. The partner reports that selling 10,000 liters of water per day at this price for 22 days a month would yield a monthly profit of INR 100,000. For water quality monitoring, the industrial partner sends monthly water samples to a NABL accredited laboratory to test for arsenic, and the results are displayed at the ECAR plant, and earlier were shared with UCB and JU.



Figure 2.12 This figure shows a) sample of the cards distributed to the students and teachers of Dhapdhapi. In Bengali, the card says, “Let us keep our health and our family’s health safe by accessing arsenic-free water from arsenic-safe sources," b) school girl who has just received her own card with spaces for name, grade level, roll number, and water card number, c) automatic dispensing units installed, and d) water queue formed during first water distribution.

The water distribution phase had its own challenges. Water distribution was scheduled to start mid-September, with the monsoon season over but temperatures still high. The ECAR plant was connected to an existing pipe network at the school and pumped to storage tanks placed on top of the school building. The layout exposed the dark green water distribution pipes and the storage tanks directly to the blazing sun. Thus, the water became extremely hot and unpleasant for drinking in the hot weather by the time it reached the automatic dispensing units and end users. Furthermore, an unexpected precipitate of white particles started appearing in the dispensed water, which caused additional concerns to everyone. The research team discovered that the high temperature of water caused precipitation of calcium carbonate through decreased solubility. To mitigate this issue, the water pipes were relocated to an underground trench, allowing the drinking water to stay naturally cool while minimizing the formation of the white precipitates. The overhead tanks were placed directly above the dispensing units, reducing solar exposure while maintaining the gravity flow to the tap. The overhead tanks were also retrofitted with a port at the bottom where settled calcium carbonate precipitates could be flushed out each morning. As a result, the drinking water maintained an appropriate temperature and was free of precipitates.

Placing a water treatment plant and distribution point at a school may promote daily student attendance. Similar to the mid-day meal lunch programs implemented in schools in India, clean water availability through the automatic dispensing units (ADUs) may contribute to education and gender equality.[84] Although Dhapdhapi High School was practicing the mid-day meal program, access to reliable arsenic-safe drinking water had not been ensured. Students demonstrated great enthusiasm on the day that water distribution began, with long lines at the ADUs (Figure 2.12). A total of four ADUs were installed, with two each designated separately for girls and boys at request of the school. The ECAR water distribution may potentially increase school attendance of young

girls who otherwise may have been required to collect good quality water for their families.[85] The fact that additional long walks are not needed to collect drinking water, and that children can attend school and still return home with (some) arsenic-safe drinking water, are major benefits to both the child's education and health (SDG 4 and SDG 5).

Upon distribution of drinking water to the school, the research team initiated the transfer process of the plant to the industrial partner. This necessitated the preparation of clear technical instructions in the form of written operations and maintenance manuals, both in English and Bengali. The research team also prepared an engineering manual to explain the detailed engineering logic behind the maintenance and operations manuals to the management of the industry partner. The preparation of manuals by the inventor is necessary for effective knowledge transfer. The technical challenges that were encountered early in the pilot phase allowed the research team to establish an operation manual and a maintenance schedule, foreseeing methods to mitigate potential problems, to ensure long-term performance beyond the IUSSTF funding phase.

2.4.2 Increasing Economic Opportunity

Dhapdhapi High School is located at a central point within the Dhapdhapi village. Rickshaw-pullers transport mothers and children to the school, and local "*cha*" or tea makers sell snacks and tea to students and teachers. The influence of the ECAR plant on the local economy depended on the design of the technology. In the United States, a fully automated plant would have significantly lower operating costs; in rural India, a labor-intensive design was optimal due to the much lower cost of labor relative to cost of capital. Two local operators with less than formal high school training were hired to work at the plant. Anecdotally, they perceived the opportunity as a new decent job (SDG 8) that also enhanced their social acceptability and status. This contextual engineering design promoted a modest amount of economic development through job creation, demonstrating that technology deployment is much more than the technology itself. Additional local employees who were hired to support the project included a guard and an electrician. This level of manual labor did not cause a financial hardship for the industry partner, while improving the livelihoods of the employed workers who took interest in promoting the commercialization process locally. In addition to earning a living wage, their pride in working at an arsenic remediation plant to provide water to the community contributed to the project's acceptance in the community, and eventual success.

2.4.3 Bridging the Knowledge Divide

Prior literature in this field discusses the social stigma associated with visible signs of arsenic poisoning.[27,28] In Bangladesh, for example, arsenic poisoning is considered contagion or a curse. Case studies have shown that awareness campaigns have helped reduced the negative social stigma associated with arsenic poisoning.[86] In this project, educating the community about the harmful effects of arsenic consumption and its natural causes were critical to alleviate such social stigma, and improve the social acceptance of the ECAR-treated water based on sound understanding of arsenic-exposure through drinking water.

Before knowledge can be effectively disseminated, building community trust is critical.[71] In social science literature, trust is considered as social capital,[87] especially for an area that has experienced numerous unkept promises and failed intervention projects. In order to overcome immediate suspicion or cynicism, intervention groups need to patiently earn the trust of the local community. Some heavily arsenic-exposed villages in West Bengal have become cynical owing

to numerous international groups visiting to study their conditions and then leaving never to return or share their findings, and without bringing positive change in the lives of the affected. Communication between academics and arsenic-prone communities is often poor, and an unwelcoming attitude can result due to growing frustrations from a problem that is being studied but not solved.[27] Given the historical context, groups planning interventions must not make any false promises, exaggerate statements of likely benefits, or underestimate costs.

ECAR is most suited for a local economy where there is at least partial reliance on arsenic-contaminated water and the community is already seeking a safe water source. For example, in Dhapdhapi area, a business was selling untreated mechanically-filtered water at 30 INR per 20 liters. The school was buying this drinking water for its teachers and staff under the belief that its quality was better than their own borewell water. General ignorance about arsenic is also common. For example, in our interactions with the school community, it became clear that even the science students did not know that boiling or simple filtration of water does not remove arsenic. In such conditions, introducing an effective, affordable arsenic-remediation technology (such as ECAR) may give rise to hostility and resistance from incumbent business interests that feel threatened. For example, during public meetings held during this project, business interests tried to compromise the community's perception of the ECAR project objectives. They questioned the efficacy of ECAR and quality of the product water. Other challenges came from political interests in a multi-party democratic social system. These groups—that sometimes have hidden agendas—sowed suspicion in the public regarding the actual severity of the problem.

The project team did not ignore any of these questions and actively listened to the concerns of the community. For example, the local community were led to believe by some scientifically unfounded hearsay that the proposed water treatment plant would be too much of a drain on the village groundwater aquifer, leading to drying out of nearby private wells. This concern was allayed by research partners investing in a hydrogeological study on the region's aquifer. Hydrogeologists of highest repute were hired with full remuneration to assess whether pumping groundwater at a rate of 10,000 LPD would deplete the aquifer for nearby wells, and for future generations. The experts submitted a written report explaining the method of their third-party verifiable study, and the team shared it with the public to maintain transparency. The team and the community gained confidence in the process through transparency of the scientific assessment that the local aquifer would not be depleted. The community was convinced that the environment would be preserved while improving public health through safe water access.

Outreach meetings with stakeholders were held by the project team 3 to 4 times a year starting from December 2012, which is considered as start of the Critical Effort Zone. Some of the meetings included active participation from the technology inventor Professor Gadgil and local social scientist partner Professor Roy. The community was invited to public meetings which were open to all and organized within school premises on multiple occasions. With support of the School's Student Assembly, and the school administration, the ECAR team held general student body meetings, smaller meetings for student leaders from each class, and separate meetings exclusively for all the teachers in the school. In addition, multiple meetings were held with student groups preparing posters about arsenic for display in the school, and with student teams working on science projects about ECAR for the annual district-level science fair. From the team's perspective, all meetings were crucial for the community understanding and acceptance of ECAR, and to ensure clear communication of the science to the rural community. Moreover, as the ECAR product water was tested for a 10-month period, NABL reports on product water quality were

printed monthly, and posted on the walls of the plant in public view, for the community to check, discuss, and disseminate the results among all those interested.

On January 31, 2017 at Dhapdhapi High School, Professor Gadgil and Professor Roy, leaders of U.S. and Indian research teams, respectively, and the VP from the industrial partner together signed a plant handover agreement, with the public as witness, signaling the formal hand-off of the ECAR plant to the industry partner for provision of arsenic-safe drinking water to students, teachers, and staff. This event provided one more opportunity for the community's questions to be heard and answered by the experts about sustainable operation of the plant beyond the project lifetime.

2.4.4 Compliance with Local Regulations

A final, but crucial, hurdle for successful technology implementation is compliance with local regulations. This project required compliance with hazardous waste management standards set by the Government of India, which are adopted and enforced by the state government via the State Pollution Control Board. Complying with regulations also required the involvement of Ramky Group, an environmental management group recognized by the state government for handling hazardous wastes. The project's industry partner signed a contract with Ramky to collect sludge once the distribution and commercialization process began. Prior to this, the local scientific partner, the Civil Engineering Department at JU, collected sludge for their use in a research project experimenting with successful immobilization of arsenic sludge in concrete.[88]

Prior to commercialization of ECAR water, the industry partner needed to obtain a trade license from the local government authorities. The two licenses, Consent to Establish (COE) and Consent to Operate (COO), were acquired from appropriate authorities in West Bengal's government, the West Bengal Pollution Control Board (WBPCB) and District Industries Center (DIC). All such contracts were preceded by multiple, formally organized visits and answers to scientific inquiries by local government agencies, coordinated by the local scientific institutional partner. After transparent, patient, and skillful efforts, and a final submission of written applications, WBPCB and DIC issued the COE and COO licenses to the industry partner. The COE and COO allow the legal operation of a water treatment plant that generates sludge (as occurs in ECAR reactors seen in Figure 2.2a) and follows the specified norms. This permit is received as a "No Objection Certificate" (NOC), for the full operation of the ECAR plant. Working with policy organizations and environmental groups have shaped the ECAR project as a contextual technology capable of adapting to local requirements and regulations.

2.4.5 Addressing Sustainable Development Goals (SDGs)

Iron-based treatment technologies are effective at removing arsenic from drinking water,[23,59,89] but alone cannot improve human well-being. The critical effort strategies discussed in this paper explore the complex nature of human behavior, cultural norms, and political maneuvers in the social integration of ECAR into the community. Thus, deployment of the first large-scale ECAR plant has addressed not only SDG 6 of safe drinking water, but several SDGs as set by the United Nations (Table 2.2).

The careful collaboration between UCB, GCP-JU, and the Indian industry partner financed by IUSSTF, is an ideal example of SDG 17 of setting up an international partnership model which can be emulated by teams addressing different global health issues (e.g., water quality, air quality, birth control, infectious diseases). Specifically, the roles of each partner were clearly established early in the project. Towards the end of the Critical Effort Zone, UCB "handed off" the pilot plant

to the industry partner to enter the commercialization phase. Monthly "all-partner" calls, tackling problems among the three partners, and the development of a "hand-off" folder for the industry partner allowed a successful and continued operation of the ECAR plant and water sales to the villages surrounding the school.

Table 2.2 Actions taken during the Critical Effort Zone to address the UN's SDGs.

SDG	Action towards goal	SDG	Action towards goal
	Affordable arsenic-safe drinking water		Job opportunities at pilot plant
	Educational campaign at rural school		Research of socially impactful electrochemical technology
	Water distribution at co-ed school		Sustainable sludge management
	Distribution of arsenic-safe drinking water		Collaboration across academic institutions and industry (United States and India)

The team's water distribution design was contextual to rural West Bengal, addressing SDGs 1, 4, 5, and 6 (briefly described in Table 2.2). Water distribution at a school provide an avenue for achieving gender equality, since equal access is assured for male and female students. This may also potentially reduce poverty levels by increasing education for rural children. As previous poverty reduction efforts include meal plans at rural schools in India,[90] a similar approach of clean water provision may promote similar outcomes. Establishing the first large-scale ECAR plant also contributed to SDG 8 by hiring local plumbers and electricians to operate the pilot plant. Throughout the project, transparency was maintained with school officials and the surrounding community, regardless of gender, education levels, and economic standing.

Moreover, it is possible to achieve the multiple SDGs, as mentioned above, while benefiting the intellectual endeavors of an academic institution (SDG 9) as well as the industrial objectives (SDG 8) of a commercial partner. Lastly, ECAR was designed to minimize waste generation and negative ecological impacts (SDG 15), which complies with local regulations and strengthens governance. ECAR operates as a Zero Liquid Discharge (ZLD) technology, meaning that the technology does not generate wastewater that must be discharged into surface water bodies or injected into clean aquifers. The only reject material stream is about 40 mg of dry sludge per liter of treated water,[88] and is easily managed without negative ecological impacts.

2.5 Concluding Remarks

The first large-scale ECAR pilot plant at Dhapdhapi High School located in a resource-poor area in rural India provides evidence of an effective commercial community-scale deployment of an arsenic removal technology for the distribution of safe drinking water. The

success of the technology implementation lies in contextualizing the design for community-scale placement and trust building among stakeholders led by the research team. This case study can serve as a template for future arsenic exposure-mitigation projects, and other social placement efforts of community-scale technology. The Critical Effort Zone is defined in this paper as the time period in which simultaneous efforts are required, with close coordination and cooperation among the institutions offering financial support, inventors working with manufacturers, local technology licensee holder, and local social science group. The social science group's active role in creating social capital in the social embedding process, beyond the technology trial itself, is critically important for success.

In scaling-up from lab to field, the ECAR team discovered and overcame new challenges that could not have been previously anticipated. Some of these challenges required redesign (e.g., keeping the water pipes cool by burying them underground) within the cultural and environmental context. All throughout the process, the scientific and technical staff were personally involved and invested in directly communicating with the local rural Indian community. With commitment, skill and patience, the team encountered and overcame infrastructural, regulatory, and political hurdles. During the Critical Effort Zone, the SDG framework was directly addressed by combining technology challenges, economic opportunities, scientific transparency, and legal compliance. The water quality data demonstrate ECAR's technical efficacy in the field implementation, and its social placement success shows promise for commercialization in other arsenic-affected regions of India, and in developing economies across the globe. Given the recorded failures of previous arsenic remediation plants in West Bengal, the success of the ECAR project, and the fact that the Dhapdhapi field trial is the first of its kind established under R&D efforts, the UCB team continued to monitor the technical performance of the plant until the Covid-19 pandemic outbreak of early 2020. They received monthly water quality data and plant operation updates from the industry partner, by working with the local scientific institutional partner GCP-JU. The future work of UCB researchers aims to develop ECAR into a more compact and energy efficient arsenic removal technology. Meanwhile, the industry partner may choose to install additional ECAR plants in India. Beyond the Critical Effort Zone, maintaining the cooperation and community relations built during the project continues to be crucial, and is carried forward through dialogue and transparency, as ECAR projects reach many other arsenic-exposed regions in West Bengal, and world-wide.

Chapter 3. Inverse Trends of As(III) and Mn(II) Removal in Air Cathode Assisted Iron Electrocoagulation

3.1 Introduction and Background

It is estimated that up to 220 million people globally are exposed to high levels of arsenic (As) through contaminated groundwater.[2] In the United States alone, 2.1 million people may be consuming As contaminated water from their domestic wells.[91] Furthermore, an estimated 55,000 people in California rely on public water systems that are out of compliance with respect to carcinogenic As.[30] Low income, mostly minority communities bear a disproportionate burden of As levels in drinking water above the EPA-Maximum Contaminant Level (MCL) of 10 μg/L.[37] A public health goal (PHG) was set to just 0.004 μg/L, the level that results in not more than one excess cancer per one million people consuming two liters of water per day for 70 years at that concentration.[92] In addition, reduced aquifers containing As are often co-contaminated by manganese (Mn), which is regulated in drinking water at 50 μg/L as the EPA secondary MCL due to aesthetic reasons. However, chronic Mn exposure has also been linked to neurological effects on children.[93,94] Effective and affordable As and Mn removal from drinking water is therefore critical to ensure the health and economic well-being of marginalized communities.

Typical techniques for Mn removal include oxidation through chemical addition. This is an autocatalytic process that induces precipitation of colloidal MnO_2 solids, and subsequent Mn(II) adsorption and oxidation.[95] Oxidative filters have also been employed to remove Mn from water matrices. These systems have also been adapted with pre-iron electrocoagulation (Fe-EC) steps, particularly when As is also present in the groundwater.[96] Fe-EC is based on the electrolytic dissolution of a sacrificial iron anode to generate Fe(II) ions that migrate to the bulk solution and react with dissolved oxygen (DO) to generate Fe(III), which is highly insoluble at circumneutral pH.[97] Byproducts of this reaction are reactive intermediates (e.g., Fe(IV) or ·OH) which oxidize As(III) to As(V), the more readily adsorbed form of As.[57,98] Fe (oxyhydr)oxides, and specifically hydrous ferric oxide (HFO), are formed with high sorption capacities.[99] Fe-EC has been shown to be an effective As removal technology that has been scaled-up and commissioned at a 10,000 liter per day capacity plant in rural India.[100] Fe-EC is simple to operate and generates a small amount of dry sludge (~40 mg/L).[88]

However, a limitation of Fe-EC is its rate limiting step of oxygen dissolution into the bulk solution,[101] and thus its reliance on large reactor tanks that need to be aerated which increases both land and energy requirements. The performance of Fe-EC for As removal declines with increasing iron production rates, or equivalently, with increasing coulombic dosage rates (CDRs). Amrose et al., 2013 found that at a low CDR of 0.06 C/L/min, a dose of only 25 C/L was required to meet the WHO guideline level. However, increasing the CDR above 2.2 C/L/min pushed the dose requirement seven times higher to 175 C/L to remove the same amount of As to safe levels. As the Fe-EC process depends on the recharge rate of O_2 into solution, increasing the rate of Fe(II) dissolution into the bulk will quickly deplete the DO and cause the accumulation of Fe(II) in the electrolyte. This results in competition of Fe(II) and As(III) for reactive Fenton-type products as well as the formation of green rust,[66] a mixed valency Fe hydroxide, that has a lower capacity than HFO for As adsorption. The higher amount of Fe dose required to reduce As concentrations to safe levels ultimately decreases operational efficiency.

Moreover, in EC experiments conducted in the absence of As, van Genuchten and Peña, 2017 showed that Mn(II) was oxidized to Mn(III) and incorporated into the resulting Fe(III)(oxyhydr)oxides in a simple electrolyte.[102] It has also been shown that the extent of Mn removal during EC varies with the solution pH and initial oxidant (O_2 versus H_2O_2).[103] Ahmad et al., 2019 found that Mn(II) and Fe(II) co-oxidation resulted in distinct solids dependent on the type of oxidant (i.e., O_2, MnO_4 or HOCl).[104] They found that the presence of strongly sorbing oxyanions led to more colloidally stable suspensions, reduced crystallinity of the Fe(III) solid, and a higher Mn/Fe solids ratio, regardless of oxidant type. However, in their absence, O_2, MnO_4 and HOCl produces Mn(III)-incorporated lepidocrocite, Mn(III)-incorporated HFO, and poorly-ordered MnO_2 and HFO, respectively.[104]

Air cathode assisted Fe-EC ("air-EC") is a novel water treatment method with strong potential for application in rural areas. Similar to conventional Fe-EC, air-EC is partly based on applying a small electric current to an Fe anode to produce Fe(II) in contaminated water. However, instead of using an Fe cathode, air-EC employs a carbon cathode that reduces O_2 in air to produce H_2O_2 in solution (Figure 3.1). Exploiting H_2O_2 for As(III) and Mn(II) removal by air-EC has many key benefits. First, H_2O_2 oxidizes Fe(II) over four orders of magnitude faster than O_2, which substantially decreases treatment time and enables high water throughput.[105] In addition, H_2O_2 reacts rapidly with Fe(II) even at acidic pH, in contrast to O_2, which broadens the possible raw waters that can be treated by air-EC.[62] Most critical for As and Mn removal, the reaction of Fe(II) and H_2O_2 produces the powerful Fenton-type oxidants (i.e., $^{\bullet}OH$, Fe(IV)) that can convert toxic As(III) to the more readily-sorbed As(V) and oxidize soluble Mn(II) to insoluble Mn(III,IV).[57,62,102]

Bandaru et al., 2020 demonstrated that air-EC consistently outperformed conventional Fe-EC in arsenic removal. Whereas Fe-EC only met the WHO-MCL of 10 µg/L for As at 1.5 C/L/min, air-EC achieved that for all CDRs (1.5 to 1200 C/L/min). Moreover, air-EC did not require post-electrolysis mixing to ensure complete oxidation of Fe(II) and As(III), nor for effective As adsorption onto precipitates. The time of treatment was thus greatly reduced to 30 seconds, which would otherwise require over three hours in Fe-EC.[66] However, this study was only conducted at pH 7, and the removal of equimolar Mn(II) was not investigated. Previous Fe-EC studies have indicated the importance of solution pH, co-occurring ions, reactor design and CDR as critical factors governing system performance.[57,77,99] Furthermore, As removal through Fe (oxyhydr)oxides has been shown to be of bidentate inner-sphere surface complexation in simple and complex electrolytes.[53,58] However, surface complexation on HFOs are pH-dependent processes that may present differences in reactions across a wide pH range.[106]

While air-EC has the potential to improve access to safe drinking water, the co-removal of As(III) and Mn(II) in the presence of other relevant groundwater constituents has yet to be studied. In this work, the As(III) and Mn(II) removal using air-EC was investigated over wide CDR (6 to 1500 C/L/min) and pH (4 to 10) ranges. Wet chemical data provided information on residual aqueous As and Mn concentrations, and the reaction products were characterized by X-ray diffraction (XRD), transmission electron microscopy (TEM), and synchrotron-based Fe, As and Mn K-edge X-ray absorption spectroscopy (XAS).

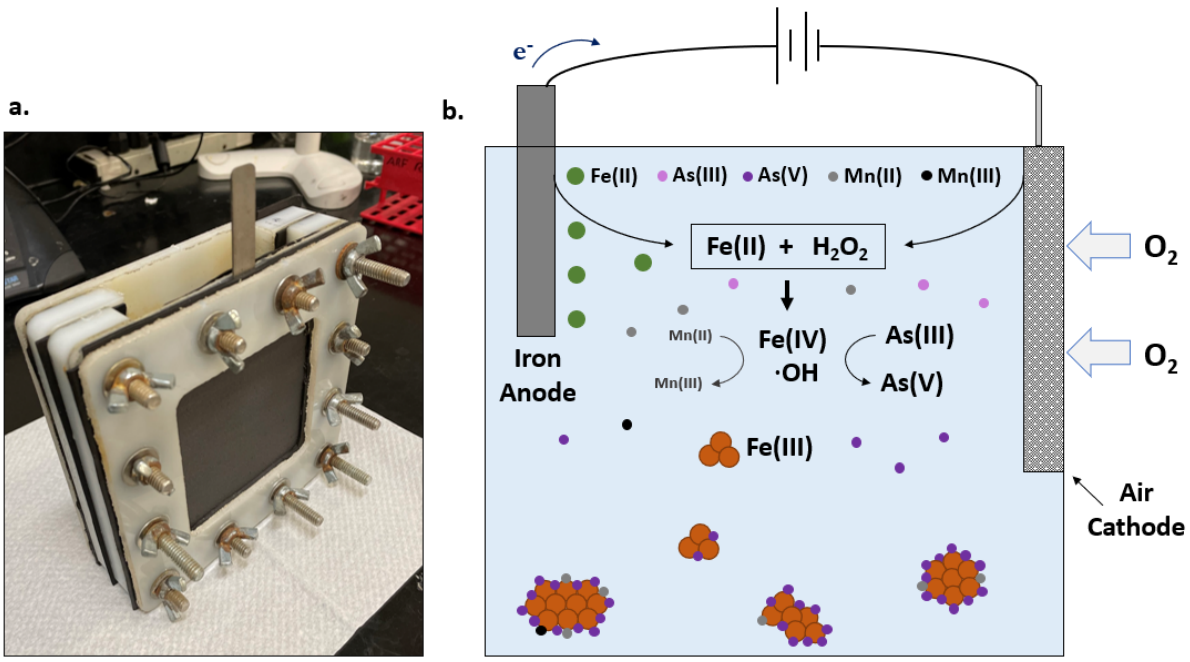


Figure 3.1 a) Digital picture and b) schematic of air-EC. The current supplied to the system oxidizes the Fe(0) in the iron anode to Fe(II), depicted as green circles. At the cathode, hydrogen peroxide (H_2O_2) is generated. In the bulk solution, Fe(II) released from the sacrificial anode reacts with H_2O_2 to form Fe(III), depicted as orange circles, which is highly insoluble at circumneutral pH, and simultaneously generates reactive intermediates, like Fe(IV) and ·OH, which oxidize arsenite, As(III) (light purple circles) to arsenate As(V) (dark purple circles), the more readily removed form of As. To a lesser extent, there is also oxidation of Mn(II) (light grey circles) to Mn(III) (dark grey circles). The Fe(III) captures the As and Mn and the aggregated precipitates settle out of solution, leaving As- and Mn-safe water at the effluent.

3.2 Materials and Methods

3.2.1 Reactor

An electrochemical cell was assembled using high density polyethylene (HDPE) to hold a volume of 250 mL (Figure 3.1). For conventional Fe-EC experiments, a 250-mL beaker was used with two low-carbon steel (1006−1026 steel grade, McMaster-CARR) plates serving as anode and cathode.

In air-EC, a low-carbon steel sheet was used as the anode in all As(III) and Mn(II) removal experiments. The anode had an active area of 7 x 9 cm^2. The maximum percentages of carbon, manganese, phosphorus, silicon, and sulfur in the steel sheets were 0.13%, 0.5%, 0.03%, 0.1%, and 0.035%, respectively. For conventional Fe-EC experiments, the active areas for both anode and cathode were 5 x 6.5 cm^2. For the cathode, a gas diffusion carbon fiber paper with a catalyst coating on the "water-facing" side, and a hydrophobic coating on the "air-facing" side was used, which was cut into 10 x 10 cm^2 squares. To fabricate the air cathode, 600 mg of graphite powder (synthetic, conducting grade, -200 mesh, 99.9995% purity, Alfa Aesar) was mixed with 2 mL of a polytetrafluoroethylene (PTFE) preparation 60 wt% dispersion in H_2O (Aldrich, CAS 9002-84-0). This slurry was painted on one side of the carbon fiber paper. This "air facing" side of the carbon paper was dried at room temperature for 20 minutes, followed by 40 minutes of sintering at 350

ºC. After 20 minutes of cooling, the "water-facing" side was prepared by painting on a mixture of 150 mg of carbon black (Black Pearls 2000, Cabot, CAS 1333-86-4), 83 µL of PTFE solution, and 2.917 mL of 1-propanol (Acros Organics, CAS 71-23-8). Once again, the cathode air dried for 20 minutes and was then sintered for 40 minutes at 350 °C. This preparation method is described in Barazesh et al., 2015. The air cathode is allowed to cool to room temperature before experiments. The active area in experiments was 8 x 8 cm^2.

3.2.2 Groundwater Synthesis

A synthetic California groundwater (SCaGW) was prepared by mixing the appropriate stock salt solutions in Milli-Q deionized water (18.2 mΩ·cm at 25 °C). The P stock solution was prepared by adding 3.58 grams of Na_2O_4P (Acros Organics, CAS 10039-32-4) to 1 L of Milli-Q water to create a 10 mM stock. The Ca stock solution was prepared by adding 14.70 grams of $CaCl_2{\cdot}2H_2O$ (Fisher Chemical, CAS 10035-04-08) to create a 100 mM stock. The Mg stock solution was prepared by adding 20.33 grams of $MgCl_2{\cdot}6H_2O$ (Acros Organics, CAS 7791-18-6) per 1 L of Milli-Q. The HCO_3^- stock solution was prepared by adding 16.80 grams of $NaHCO_3$ (Fisher Chemical, CAS 144-55-8) to 1 L of Milli-Q for a 200 mM stock. The Si stock solution was prepared by adding 2.12 grams of $Na_2O_3Si{\cdot}5H_2O$ (Aldrich Chemistry, CAS 10213-79-3) to Milli-Q to create a 10 mM stock.

Appropriate amounts of 200 mM HCO_3^- ($NaHCO_3$) stock solution was added, followed by appropriate amounts of 100 mM Ca^{2+} ($CaCl_2{\cdot}2H_2O$), 10 mM P (Na_2O_4P) and 100 mM Mg^{2+} ($MgCl_2{\cdot}6H_2O$) stock solutions. The pH was lowered to <6 by bubbling CO_2 into solution. Subsequently an appropriate amount of stock solution of 10 mM of Si ($Na_2O_3Si{\cdot}5H_2O$) was added, followed by 10 mM NO_3^- ($NaNO_3$), 1000 mM SO_4^{2-} (Na_2SO_4), and 10 mM Mn^{2+} ($MnCl_2$) stock solution volumes. For a final concentration of 3 mg/L of NOM (fulvic acid, IHSS Suwannee River NOM, RO Isolation 2R101N)), an appropriate amount of previously dissolved and filtered fulvic acid solution was added. A TOC Analyzer was used to analyze the organic carbon content of the stock solution.

Table 3.1 Solution Chemistry of Synthetic California Groundwater.

	Ca	**P**	**Si**	**Mg**	**Mn**	**HCO_3^-**	**NO_3^-**	**SO_4^{2-}**	**NOM**	**As**
mg/L	30	10	15	25	1	122	3.6	1000	3	1.5
mM	0.75	0.32	0.53	1.03	0.02	2.00	0.06	10.41	0.01	0.02

3.2.3 Batch Experiments

Prior to electrolysis experiments, the electrocoagulation (EC) electrodes were prepared by first sanding the iron electrode to remove existing rust layers and rinsing with DI water. The electrode was immersed into the previously prepared synthetic California groundwater (SCaGW). The solution was adjusted to the selected pH (4, 7, or 10) with either base (1 M NaOH) or acid (1.1 M HCl). The applied current and experiment time were selected according to the CDR (6, 600, or 1500 C/L/min) and total volume (including total base or acid added) and equated to a total Coulombic dose of 600 C/L for all experiments. The interelectrode distance was ~1 cm. The initial As(III) concentration for all experiments was 1500 µg/L (Alfa Aesar Sodium arsenite, 0.1 N

Standard, Liquid, $NaAsO_2$, CAS 7784-46-5). The solution was mixed during electrolysis with an overhead stirrer (Thermo Scientific Orion Dual Star pH/ISE Meter). Experiments were conducted at room temperature and open to the atmosphere. Measurements for pH, conductivity, and dissolved oxygen (DO) were taken using a Thermo Scientific Orion Star A Series meter before and after electrolysis (pH probe Orion 8107BNUMD ROSS Ultra pH/ATC Triode; conductivity probe Orion 013010MD Conductivity Cell; DO probe Thermo Scientific Rugged Dissolved Oxygen Orion 087003).

The pH range of 4 to 10 was selected to probe the efficiency of air-EC and to elucidate potentially different As(III) and Mn(II) removal mechanisms occurring in this system. All experiments were started by applying a constant current to the cell. The total Coulombic dose for each experiment was selected as 600 C/L, based on Bandaru et al., 2020, corresponding to a total iron concentration of 173 mg/L (3.1 mM), according to Faraday's law. The selected CDRs of 6, 600 and 1500 C/L/min correspond to iron production rates of 0.03, 3.11, and 7.77 mM/min, respectively. For 600 C/L, these rates correspond to experiment durations of 0.4, 1, and 100 min. The initial solution ratio of As/Fe and Mn/Fe was 0.6 mol%.

3.2.4 Chemical Measurements

At the end of each experiment, unfiltered aliquots were collected and acidified with 1.1 M HCl to measure total Fe using inductively coupled plasma optical emission spectroscopy (ICP-OES). Filtered samples using a 0.2 µm nylon filter (Inorganic Membrane Filter, Whatman™ Anotop™) were also taken to measure residual As, Mn, and dissolved Fe in solution using inductively coupled plasma mass spectrometry (ICP-MS). These samples were acidified with 0.5% HNO_3 and 1% HCl prior to analysis. The As(III) and Mn(II) removal was calculated by subtracting the residual concentration in the filtrate from their initial concentrations.

3.2.5 Solid Phase Characterization

3.2.5.1 Sample Preparation

A volume of the iron slurry at the end of the experiment was collected and filtered using a vacuum filter (MF-Millipore, 0.22 µm MCE Membrane). The solids on the membrane filter were placed in the freezer until XRD analysis. For XAS analysis, the volume filtered was selected based on the mass requirements for the absorption length of Fe to be less than 1.0 for transmission measurements (with one absorption length signifying 37% of photons being transmitted).[107,108] The filter paper containing the sample was then cut into three strips, which were stacked and taped onto the sample holder using Kapton tape. To prevent unwanted oxidation before XAS data collection, the iron samples were coated with glycerol. The samples were placed in a freezer (-18 °C) until further analysis at the synchrotron facility.

3.2.5.2 Data Collection and Reduction

The X-ray diffractograms were collected on a PANalytical X'Pert PRO MPD using a Co X-ray source. TEM was carried out at the UC Berkeley Electron Microscope Lab with a FEI Tecnai 12 transmission electron microscope operated at 120 kV. XAS data at the Fe, Mn and As K-edges were collected at Beamline 4-1 of the Stanford Synchrotron Radiation Lightsource (SSRL, Menlo Park, USA). The As data were collected under liquid nitrogen temperatures (~80 K) in fluorescence mode to k of 13 $Å^{-1}$. The beam was calibrated using an Au foil to the maximum of the first derivative (11.919 KeV). The Mn data were also collected in fluorescence mode up to a

reciprocal space value of 11.3 $Å^{-1}$. For Mn data collection, the beam was calibrated to a Mn foil (6539 eV). Fluorescence measurements were performed using either a solid-state passivated implanted planar silicon (PIPS) detector or a 30-element Germanium (Ge) detector. The Fe data were collected in transmission mode calibrated to a Fe(0) foil (7112 eV) up to a reciprocal space value of 13 $Å^{-1}$.

Spectra were aligned, averaged and background-subtracted using SixPACK software[109] following standard methods described in van Genuchten et al., 2012. The Fe and As EXAFS spectra were extracted using k^3-weighting. For both Fe and As, the Fourier transform was done using a Kaiser-Bessel window with dk of 3 $Å^{-1}$, over the *k*-range of 3 to 13 $Å^{-1}$.

3.2.5.3 Data Analysis

Linear combination fits (LCFs) of the Fe K-edge EXAFS spectra were performed to obtain the fraction of lepidocrocite (Lp), two-line ferrihydrite (2LFh) and hydrous ferric oxide (HFO) of the electrolytically generated precipitates. Based on previous work, Lp and HFO were selected as the most and least crystalline end members, respectively, as expected for the solid products in the air-EC system.[66] The Fe K-edge LCFs were performed over the *k*-range of 2 to 10 $Å^{-1}$. The sum of the components was set to 1. LCFs of the As K-edge XANES spectra were performed to obtain the fraction of As(III) and As(V) sorbed to the EC precipitates. The LCFs were performed over the energy range of 11860 to 11890 eV using the spectra for As(III) and As(V) adsorbed to 2-line ferrihydrite as references. The percentage of Mn(II), Mn(III) and Mn(IV) species was also quantified with LCFs. The normalized Mn K-edge XANES spectra were fit from 6525 to 6600 eV using aqueous Mn(II), bixbyite (α-Mn_2O_3), and birnessite (δ-MnO_2) as components. Following previous approaches, negative fit-derived fractions were not allowed in the fit and the sum of the components was constrained to 1 for Mn but were unconstrained for As.[110] This approach allowed for a lower R-factor, which was used as the goodness-of-fit metric.[107]

Shell-by-shell fits of Fe EXAFS K-edge was completed using SixPack, which functions through algorithms derived from the IFEFFIT library. The structure of goethite (α-FeOOH) was used to calculate with FEFF6 the phase and amplitude functions of Fe–O and Fe–Fe single scattering paths. This allowed us to obtain coordination number and bond length values of the highly disordered electrolytically generated precipitates. Shell-by-shell fitting was done in addition to LCFs to compare the results from two analysis techniques. To determine the coordination environment of As adsorbed to the EC samples and the reference material, shell-by-shell fitting was performed with SixPack software using the structure of scorodite ($FeAsO_4 \cdot H_2O$) for As–O, As–O–O, and As–Fe paths.[111] Algorithms derived from IFEFFIT[112] were used to perform the fits from 1 to 4 Å in R+ΔR-space for As shell-by-shell fits. The parameters that were varied in the fits were interatomic distance (R), coordination number (CN), mean squared atomic displacement parameter (σ^2) and change in threshold energy (ΔE_0).

3.3 Results

3.3.1 Mn Removal

The initial Mn(II) concentration in the SCaGW was 1008.6 ± 39.3 µg/L. As seen in Figure 3.2, the removal of Mn during air-EC treatment depended strongly on pH, with a smaller dependence on CDR. Mn removal was highest at pH 10, with final concentrations of 3.4 ± 3.3 µg/L, 0.8 ± 0.1 µg/L, and 1.0 ± 0.2 µg/L at CDRs of 6, 600 and 1500 C/L/min, respectively. The

poorest performance was observed at pH 4, in which final Mn concentrations were 1199.5 ± 326.2 µg/L, 1047.5 ± 128.7 µg/L, and 1090.0 ± 105.1 µg/L for CDRs of 6, 600 and 1500 C/L/min, respectively. At this low pH there was no removal. The removal of Mn at pH 7 was intermediate between pH 4 and 10 and displayed a general trend of increasing removal efficiency with increasing CDR. The remaining Mn at 6, 600 and 1500 C/L/min was 458.8 ± 64.0 µg/L, 311.5 ± 63.4 µg/L, and 275.3 ± 138.5 µg/L, respectively.

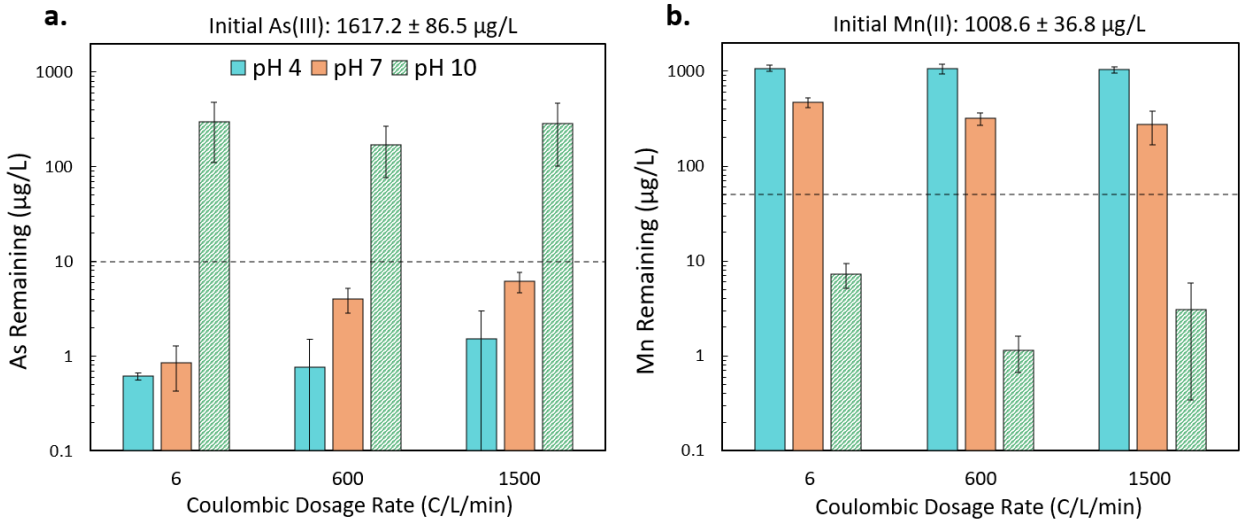


Figure 3.2 As(III) and Mn(II) removal from synthetic California groundwater as a function of CDR and pH. The total Coulombic dose was 600 C/L. The dashed line refers to either a) the primary MCL for As of 10 µg/L or b) the secondary MCL for Mn of 50 µg/L.

In terms of Mn uptake onto the electrolytically generated Fe precipitates, as seen in Figure 3.3, the Mn:Fe solids ratio increased from ~3.8 µg/mg to ~5.8 µg/mg when the pH increased from 7 to 10. At pH 7, the Mn/Fe solids ratio was 3.1 ± 0.4, 4.0 ± 0.3 and 4.2 ± 0.6 µg/mg at CDRs of 6, 600 and 1500 C/L/min, respectively. In conventional Fe-EC experiments, the final Mn concentration was ~500 µg/L at pH 7 at 600 C/L/min. The secondary EPA-MCL of 50 µg/L for Mn was met for all dosage rates at pH 10, but not for any CDR at pH 4 or 7. For all CDRs at pH 10, the Mn concentration was up to 50 times lower than the secondary MCL. At pH 10, no trend with CDR was observed. The uptake remained the same across CDRs at pH 10 due to the nearly complete Mn removal in each of these experiments.

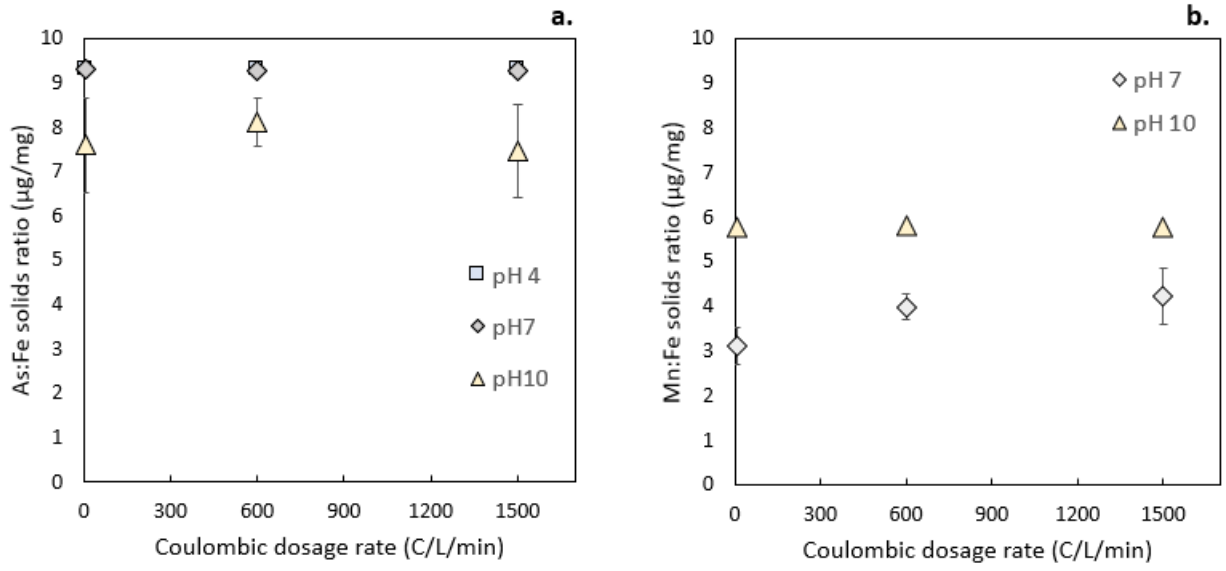


Figure 3.3 As:Fe and Mn:Fe ratios of adsorbed species onto electrolytically generated iron (oxyhydr)oxides for total of 3.1 mM Fe.

Table 3.2 Solids ratio of adsorbed As and Mn species onto Fe solids.

CDR	pH 4		pH 7		pH 10	
	As:Fe (µg/mg)	Mn:Fe (µg/mg)	As:Fe (µg/mg)	Mn:Fe (µg/mg)	As:Fe (µg/mg)	Mn:Fe (µg/mg)
6	9.3 ± 0.0	---	9.3 ± 0.0	3.1 ± 0.4	7.6 ± 1.0	5.8 ± 0.0
600	9.3 ± 0.0	---	9.3 ± 0.0	4.0 ± 0.3	8.1 ± 0.5	5.8 ± 0.0
1500	9.3 ± 0.0	---	9.3 ± 0.0	4.2 ± 0.6	7.5 ± 1.1	5.8 ± 0.0

3.3.2 As Removal

The initial As(III) concentration in the SCaGW was 1617.1 ± 86.5 µg/L. The best As removal efficiency in air-EC was found at pH 4, at which the final As concentrations at 6, 600 and 1500 C/L/min were 0.6 ± 0.1 µg/L, 0.6 ± 0.6 µg/L, and 1.6 ± 1.5 µg/L, respectively. These correspond to a As:Fe solids ratio of 9.3 µg/mg across CDRs. The poorest As removal efficiency was observed at pH 10 for which the residual As concentrations were 231.6 ± 207.6 µg/L, 160.0 ± 62.6 µg/L, and 225.0 ± 108.0 µg/L at 6, 600 and 1500 C/L/min, respectively. No trend in As removal with CDR at pH 10 was observed. At pH 10, the As:Fe solids ratio was ~7.7 µg/mg across CDRs (Table 3.2). At pH 7 the final As concentration at 6, 600 and 1500 C/L/min was 0.9 ± 0.4 µg/L, 4.0 ± 1.2 µg/L, and 6.2 ± 1.5 µg/L, respectively. At this pH, there was a modest trend with CDR, with decreased removal efficiency as CDR increased. Despite this trend, the EPA-MCL of 10 µg/L was achieved at all CDRs at pH 7. The EPA-MCL was also met for all CDRs at pH 4. The uptake of As onto the iron precipitates remained at ~9.3 µg/mg across all CDRs at pH 4 and 7 because of the nearly complete As removal in these experiments. However, the MCL was not met for any CDR at pH 10. Conventional Fe-EC at pH 7 did not meet the MCL of 10 µg/L, with a

final concentration of about 60 µg/L, six times higher than the MCL. For pH 4 and 7 at a CDR of 6 C/L/min, as well as at pH 4 at 600 C/L/min, the final As concentration was below 1 µg/L in air-EC.

3.3.3 Removal of Competing Species

The removal of P and Ca were also tracked, which are known to be competitive ions for adsorption sites on Fe(III) (oxyhydr)oxide surfaces.[77,104] The initial P concentration in the SCaGW was 11.2 ± 0.2 mg/L. In air-EC, P removal was found to be about the same at pH 4 and 7. At pH 4, the final P concentration at 6, 600 and 1500 C/L/min was 0.11 ± 0.14 mg/L, 0.03 ± 0.04 mg/L, and 0.04 ± 0.04 mg/L, respectively. At pH 7, the final concentrations were 0.05 ± 0.05 mg/L, 0.07 ± 0.07 mg/L, and 0.05 ± 0.05 mg/L, at 6, 600 and 1500 C/L/min, respectively. These correspond to P:Fe solids ratio of ~64 µg/mg at pH 4 and 7, and ~54 µg/mg at pH 10. The poorest P removal efficiency was observed at pH 10 for which the residual P concentrations were 2.2 ± 1.0 mg/L, 1.7 ± 0.7 mg/L, and 1.9 ± 0.8 mg/L at 6, 600 and 1500 C/L/min, respectively. No trend in P removal with CDR at pH 10 was observed. In conventional Fe-EC at pH 7 and at a 600 C/L/min CDR, the final P concentration was ~300 mg/L.

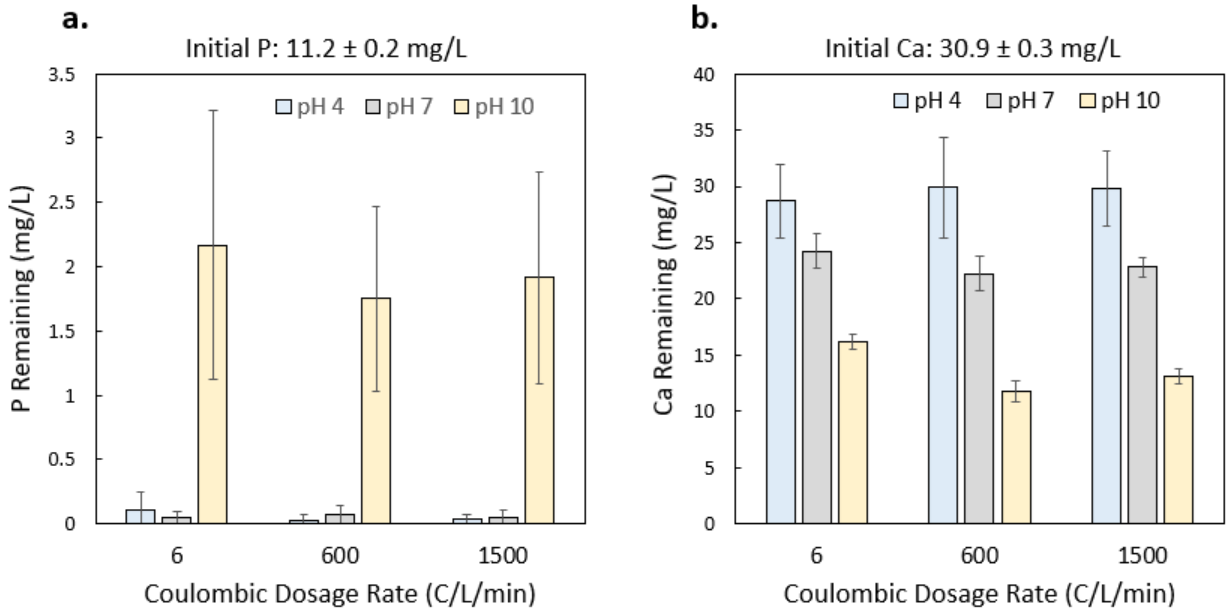


Figure 3.4 P and Ca removal from SCaGW as a function of CDR and pH. The total Coulombic dose was 600 C/L.

The initial Ca concentration in the SCaGW was 30.9 ± 0.3 mg/L. As seen in Figure 3.4, the removal of Ca during air-EC treatment depended strongly on pH, with a smaller dependence on CDR at pH 7 and pH 10. Ca removal was highest at pH 10, with final concentrations of 16.2 ± 0.7 mg/L, 11.8 ± 0.9 mg/L, and 13.1 ± 0.7 mg/L at CDRs of 6, 600 and 1500 C/L/min, respectively. The poorest performance was observed at pH 4, in which final Ca concentrations were 28.7 ± 3.3 mg/L, 29.9 ± 4.5 mg/L, and 29.8 ± 3.3 mg/L for CDRs of 6, 600 and 1500 C/L/min, respectively. The removal of Ca at pH 7 was intermediate between pH 4 and 10 and displayed a general trend of increasing removal efficiency when increasing from 6 to 600 C/L/min. Removal did not improve when increasing from 600 to 1500 C/L/min. At pH 7, the remaining Ca at 6, 600 and 1500 C/L/min was 24.3 ± 1.6 mg/L, 22.3 ± 1.5 mg/L, and 22.8 ± 0.8 mg/L, respectively. In terms of Ca uptake

onto the electrolytically generated Fe precipitates, as seen in Figure 3.5, the Ca:Fe solids ratio increased from ~8 µg/mg to ~99 µg/mg when the pH increased from 4 to 10. At pH 7, the Ca/Fe solids ratio is 38.3 ± 13.7, 49.9 ± 13.8 and 46.7 ± 13.5 µg/mg at CDRs of 6, 600 and 1500 C/L/min, respectively. In conventional Fe-EC experiments, the final Ca concentration was ~28 mg/L at pH 7 at 600 C/L/min. As seen in Table 3.3 there is variability in the Ca:Fe solids ratio across pHs and CDRs, with a clear trend with greater uptake at highest pH, but no consistent increase or decrease with CDR. Previous studies have shown competition of Ca with Mn for sorption sites on oxyanion-rich HFO.[104]

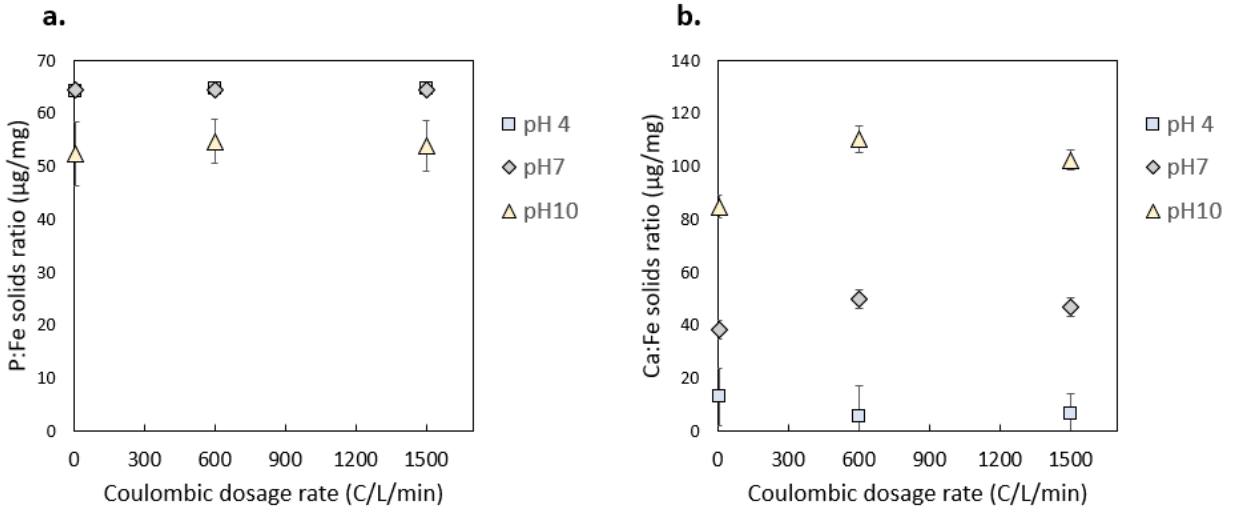


Figure 3.5 P:Fe and Ca:Fe ratios of adsorbed species onto electrolytically generated iron (oxyhydr)oxides for total of 3.1 mM Fe.

Table 3.3 Solids ratio of adsorbed P and Ca species onto Fe solids.

CDR	pH 4		pH 7		pH 10	
	P:Fe (µg/mg)	Ca:Fe (µg/mg)	P:Fe (µg/mg)	Ca:Fe (µg/mg)	P:Fe (µg/mg)	Ca:Fe (µg/mg)
6	64.2 ± 0.8	12.8 ± 10.9	64.5 ± 0.3	38.3 ± 13.7	52.3 ± 6.0	84.7 ± 4.1
600	64.6 ± 0.2	5.7 ± 11.6	64.4 ± 0.4	49.9 ± 13.8	54.7 ± 4.1	110.2 ± 5.0
1500	64.6 ± 0.3	6.4 ± 7.6	64.5 ± 0.3	46.7 ± 13.5	53.7 ± 4.8	102.3 ± 3.9

Table 3.4 Initial molar ratios of various elements to Fe content (3.1 mM) in SCaGW.

As/Fe	Mn/Fe	P/Fe	Ca/Fe	Si/Fe	Mg/Fe
0.006	0.006	0.103	0.242	0.171	0.332

3.3.4 X-ray Diffraction of Fe Precipitates

The X-ray diffractograms (Figure 3.6) **s**how that at all CDRs and pHs tested, air-EC generated highly disordered nanocrystalline iron precipitates. The peak present near 41º 2θ for all conditions is typical for ferrihydrite. The broad peaks for solids generated at 1500 C/L/min for pH 4 and 7 are expected for nanocrystalline particles, which indicates that the short experimental time scale (24 seconds) did not allow for proper crystallization. The sharpest peaks were found for the pH 10 sample, including another peak at about 75º 2θ. This second peak was also found for the pH 7 samples, but was not as distinct. The more resolved peaks in the pH 10 samples may be explained by the lower amount of As uptake (~7.7 µg As/mg Fe). The lower amount of surface poisoning by oxyanions in the water matrix may allow for more Fe(III) polymerization.[77] The sample analyzed from a conventional Fe-EC experiment at pH 7 also showed a relatively sharp peak at 41º 2θ, indicating a more crystalline precipitate than the air-EC samples at the same pH.

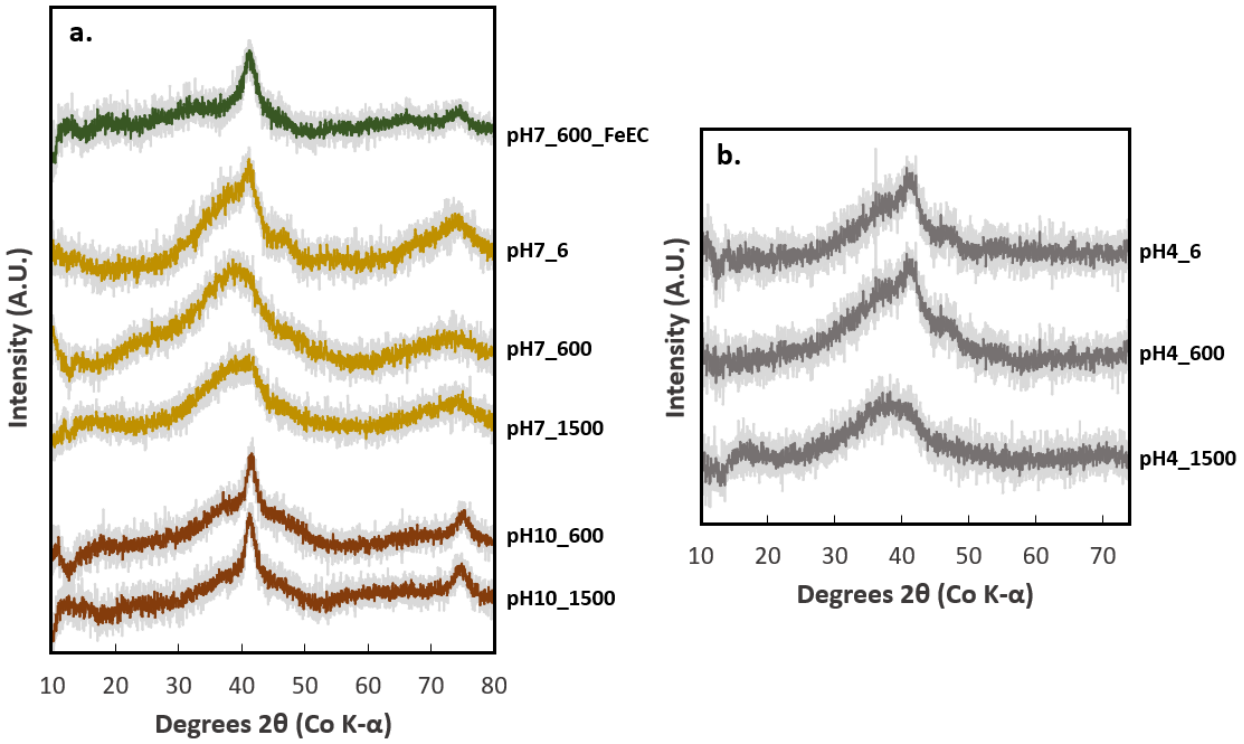


Figure 3.6 XRD of precipitate samples generated in a range of CDRs at a) pH 7, pH 10, and b) pH 4.

3.3.5 Transmission Electron Microscopy of Fe particles

The TEM images (Figure 3.7 and Figure 3.10) show the agglomeration state of the electrolytically generated Fe(III) precipitates. Particle coagulation into more linear chain-like flocs is apparent in panels a and b of the electron micrographs. As shown in panels c and d in the figure below, some of the individual particles appeared to exhibit an angle of ~120 degrees. These hexagonal platelets are characteristic of two-line ferrihydrite (2LFh), and exhibit slightly coarser surface texture than typical of HFO particles.[113] This degree of coarseness observed in the precipitates may indicate some level of long-range order, which is also supported by the LCFs as discussed in the next section. Previous TEM showed the morphology of the particles generated in air-EC as smooth spheres with diameter sizes of about 100 nm (Figure 3.8 and Figure 3.9). As

discussed in previous studies, particles with smooth surface texture indicate nanocrystallinity.[113] There is no presence of lath-like particles, which are representative lepidocrocite (Lpd). As discussed below, the Fe K-edge EXAFS support the absence of Lpd in the Fe solids.

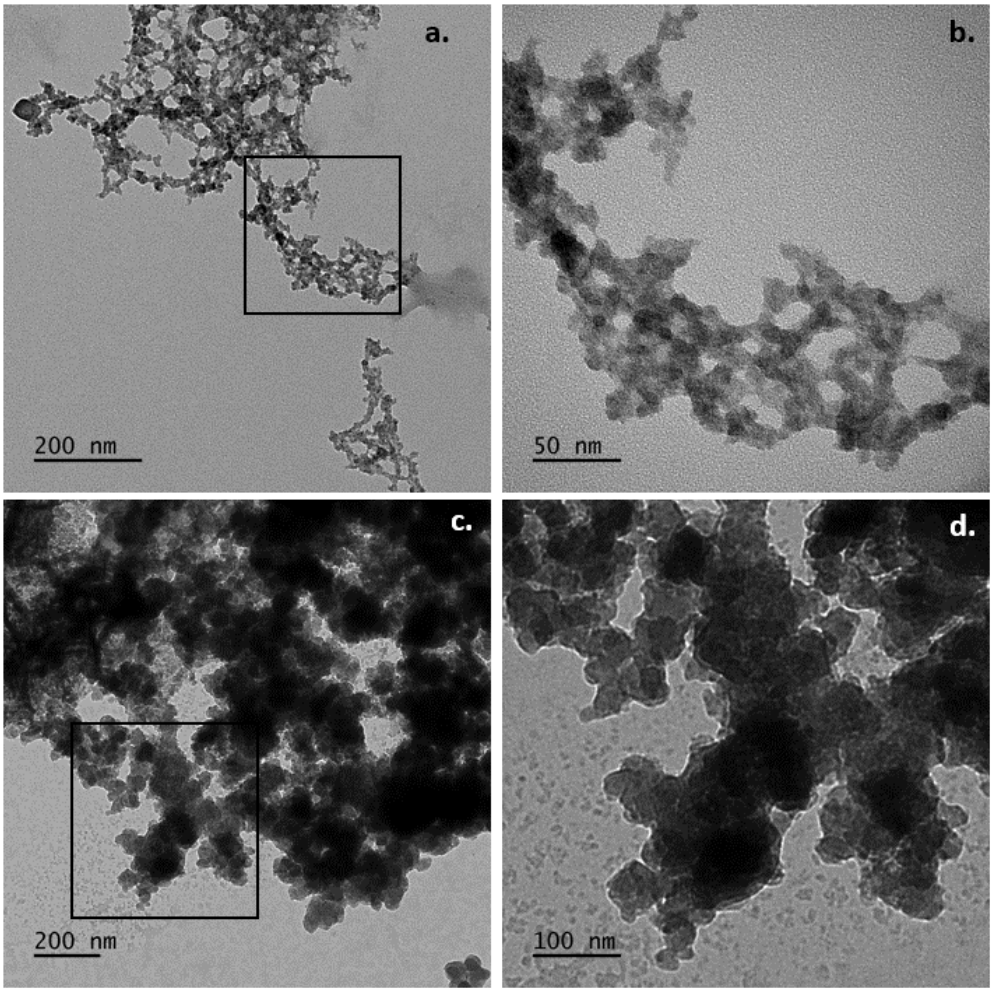


Figure 3.7 TEM of samples from air-EC experiments conducted at a) pH 7 and 600 C/L/min, and c) pH 4 and 6 C/L/min. Panels b and d are the magnified regions outlined in panels a and c, respectively.

The TEM below shows the iron spherical particles that are rounded and smooth, as opposed to coarse or lath shaped. The smoothness indicates the low crystallinity of the particles, which characterizes them as HFO. A more crystalline phase like lepidocrocite would not appear spherical. Two-line ferrihydrite would appear coarser with its greater crystallinity than HFO. The presence of phosphate and silicate, particularly phosphate, impedes greater polymerization. These result in mostly edge-sharing linkage Fe-octahedra, as shown in the XAS. These particles that are round and smooth indicate a lack of long-range order.[113]

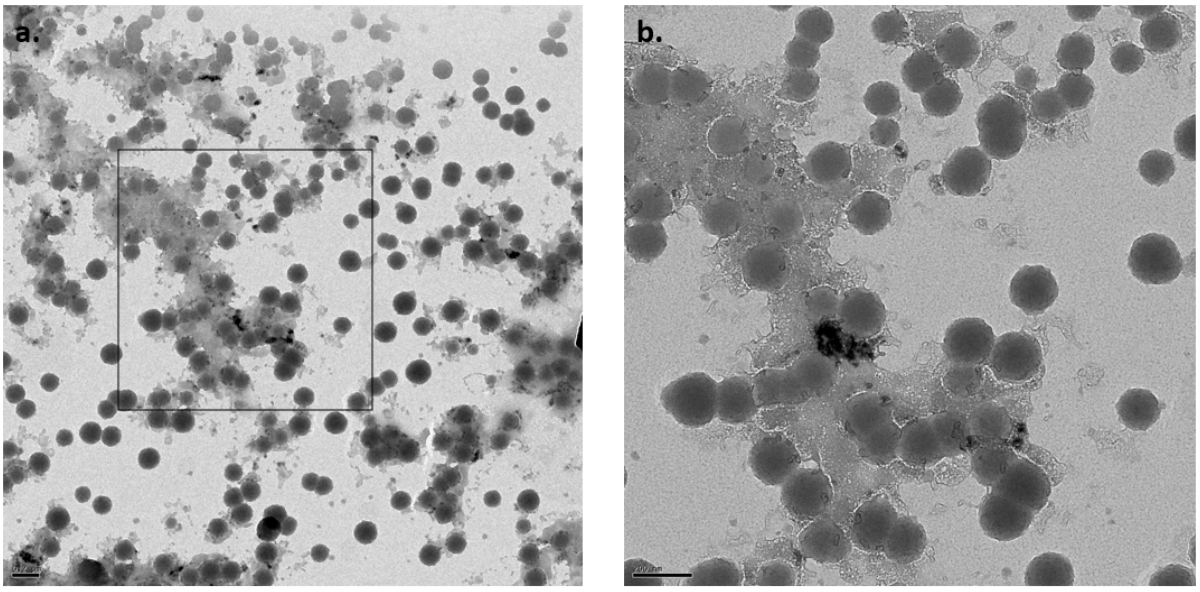


Figure 3.8 TEM of samples generated in a Synthetic Bengal Groundwater (solution matrix described in Delaire et al., 2015)[114]. The scale bar for both micrographs is 200 nm. The smoothness of the spherical particles indicates a highly disordered Fe(III) state.

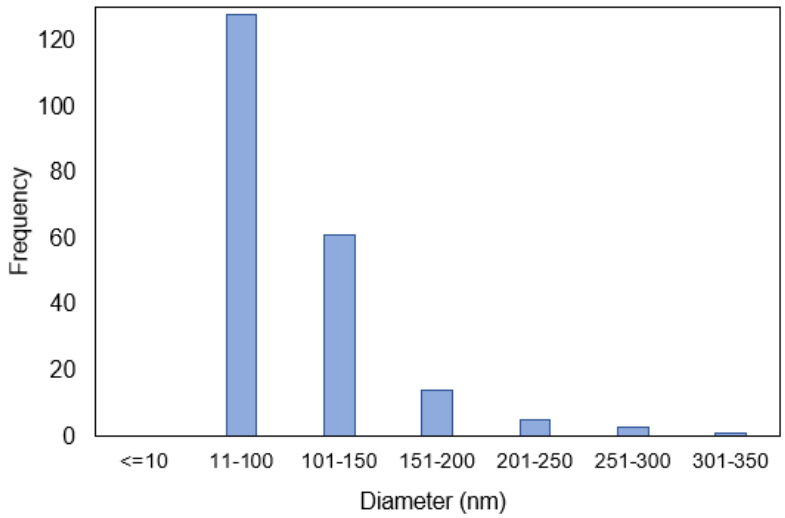


Figure 3.9 Size distribution of particles as determined using ImageJ software.

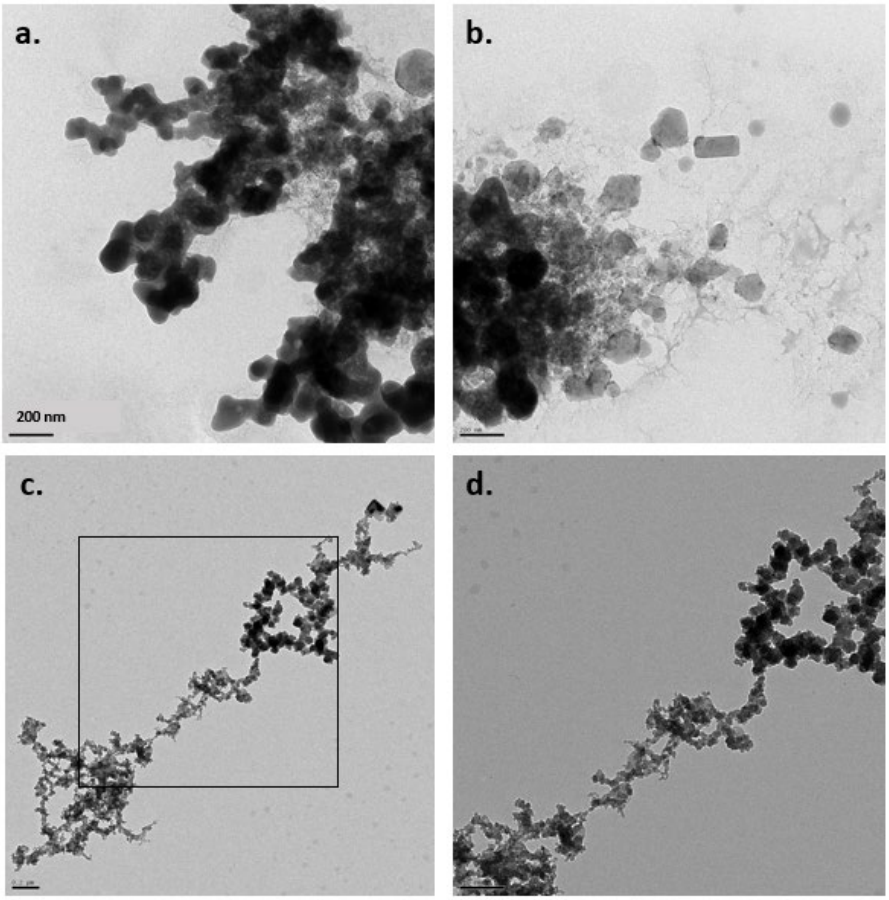


Figure 3.10 Additional TEM micrographs of particles depicting morphology and chain-like aggregation in Synthetic Bengal Groundwater. The scale bar across micrographs is 200 nm.

3.3.6 Fe K-edge EXAFS and LCFs

Figure 3.11 shows the Fe K-edge EXAFS spectra for samples generated in pH 7 and 10 conditions at CDRs of 6, 600 and 1500 C/L/min, as well as reference spectra for Lpd, 2LFh, and HFO. The Fe K-edge EXAFS showed no major effect of CDR on the shape of the EXAFS spectra. All precipitates appeared to be poorly ordered Fe(III) (oxyhydr)oxides, with much less order than Lpd. The oscillation at around 4 $Å^{-1}$ of all samples follows a similar shape as that of HFO, as opposed to the more asymmetric peak of the 2LFh reference spectrum.

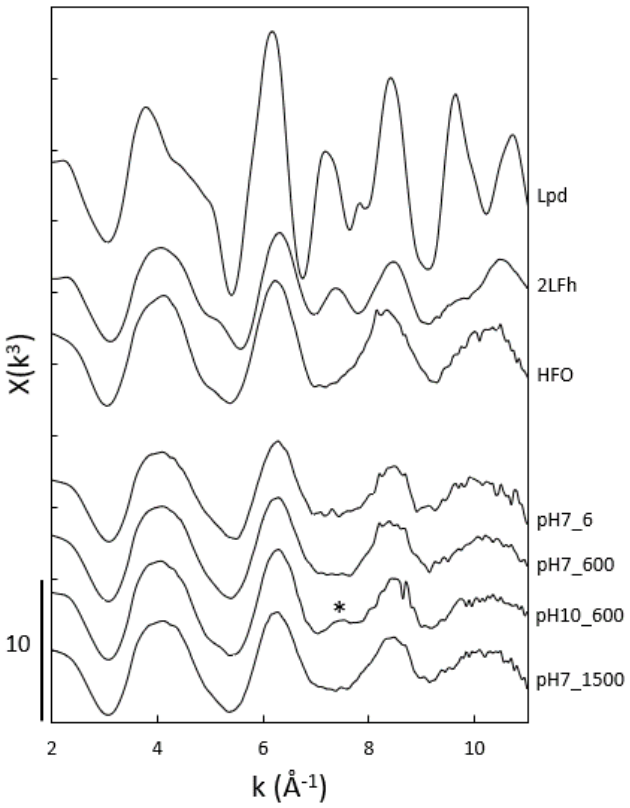


Figure 3.11 Fe K-edge EXAFS spectra for selected samples at pH 7 and 10.

HFO is characterized by reduced corner sharing and edge-sharing linkages of Fe-octahedra compared to 2LFh and Lpd.[115] The Fe polyhedra of 2LFh contain octahedral edge-sharing, octahedral corner-sharing, and tetrahedral corner sharing with a range of structural coherence near 2 nm.[60] None of the pH 7 samples contain the characteristic Lpd peak around 7.5 $Å^{-1}$. However, there is a small peak at about 7.5 $Å^{-1}$ (indicated by an asterisk in the figure) in the pH 10 sample. As seen in the wet chemical data (Figure 3.3 and Figure 3.5), oxyanion uptake (As and P) was the least at pH 10. At lower pHs, the oxyanions present in the water matrix would otherwise interfere during Fe(III) polymerization, leading to surface poisoning as those species bind corner-sharing Fe surface sites.[77] The resulting precipitate is characterized by a deficiency in corner-sharing Fe.[60] The spectral feature unique to the pH 10 sample may indicate less crystal growth poisoning, as compared to the pH 7 samples. However, the LCFs (Table 3.5) indicated that across CDRs at pH 7, the solids had a structure consistent with 50% HFO and 50% 2LFh. The same fractions were found at pH 10 at 600 C/L/min. Despite the subtle peak at 7.5 $Å^{-1}$ for the pH 10 spectrum and its absence in the pH 7 spectra, the LCFs did not yield a major difference among samples.

Table 3.5 Results of LCFs using the Fe K-edge Chi data.

Sample ID	Fraction 2LFh	Fraction HFO	Fraction Lp	R-Factor
pH7_1500	0.51	0.49	0	0.05
pH7_600	0.51	0.49	0	0.05
pH7_6	0.54	0.46	0	0.06
pH10_600	0.53	0.47	0	0.03

3.3.7 Fe K-edge EXAFS Fourier Transform Shell-by-Shell Fits

Fits of the first-shell peak of the pH 7 samples generated by air-EC returned $R_{Fe\text{-}O}$ values of 1.97 – 1.98 Å and $CN_{Fe\text{-}O}$ values between 5.6 and 5.9 (Figure 3.12 and Table 3.6). The $R_{Fe\text{-}O}$ value for the pH 10 sample was the same, but the $CN_{Fe\text{-}O}$ value was slightly higher at 6.7 ± 0.6. However, this variation was not significant enough to indicate a difference in the structure of the Fe(III)-precipitate. While the shell fits showed Fe–O coordination values of ~6 for all samples (Table 3.6), the $N_{Fe\text{-}Fe}$ for the precipitates generated in the pH 10 and 600 C/L/min experiment was significantly different than the other samples. This sample showed a higher N of ~2.5 (while ~2.0 for the other samples at pH 7), suggesting a higher degree of Fe–Fe polymerization at pH 10. This result is also consistent with the more resolved peaks in the XRD pattern of the pH 10 sample (Figure 3.6). Qualitatively, the second-shell peak of the Fourier-transformed EXAFS spectra also appears to have a higher amplitude for the pH 10 sample, which is representative of higher Fe–Fe polymerization. However, for all samples the second shell peak (Fe–Fe) is dampened relative to Lpd, which was also observed in a study examining the structure of Fe(III) precipitates generated by Fe(II) oxidation by chemical additions of H_2O_2.[102] The shell-fits of the second peak of all samples are not consistent with the presence of Fe–Fe corner sharing linkages, which would be characterized by a ~3.4 Å bond length.[60]

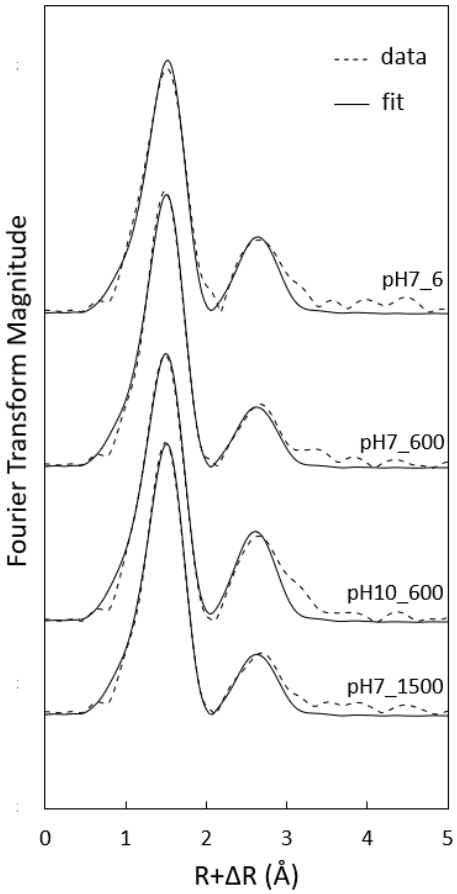


Figure 3.12 Fourier-transformed EXAFS spectra and shell fits of selected samples. Dashed lines represent data and solid lines represent the fit.

Table 3.6 Summary of shell-by-shell fitting results.

Sample	Atomic Pairs	N	R(Å)	σ^2 (Å^2)	ΔE_0 (eV)	R-factor
pH10_600	Fe–O	6.7 (0.6)	1.98 (0.01)	0.010 (0.001)	-4.4 (1.1)	0.016
	Fe–Fe	2.5 (0.3)	3.03 (0.01)	0.012		
pH7_600	Fe–O	5.9 (0.4)	1.97 (0.00)	0.009 (0.001)	-5.0 (0.9)	0.01
	Fe–Fe	1.8 (0.2)	3.05 (0.01)	0.012		
pH7_6	Fe–O	5.6 (0.5)	1.98 (0.01)	0.009 (0.001)	-3.3 (1.1)	0.017
	Fe–Fe	2.2 (0.3)	3.05 (0.01)	0.012		
pH7_1500	Fe–O	5.9 (0.4)	1.97 (0.00)	0.009 (0.001)	-4.5 (0.9)	0.01
	Fe–Fe	1.8 (0.2)	3.05 (0.01)	0.012		

3.3.8 Mn K-edge XANES and LCFs

The Mn K-edge XANES spectra of pH 7 and pH 10 samples generated at 600 C/L/min are shown in Figure 3.13 along with reference materials. The pH 4 samples were not included as there was no uptake of Mn under those experimental conditions. While the peak of the absorption edge for all samples align with the Mn(II) reference spectrum, the shoulder at higher X-ray energies in the samples are consistent with the presence of high-valent Mn species (i.e., Mn(III)). The LCFs indicated that Mn was taken up primarily as Mn(II), with a lower fraction of Mn(III), at 59% and 41%, respectively, at pH 7 and 600 C/L/min. These values were similar at pH 10 and 600 C/L/min with 56% and 45% for Mn(II) and Mn(III), respectively. No Mn(IV) was detected by the LCFs for any sample. The LCFs of the conventional Fe-EC sample (coded as "pH7_600_EC") indicated poorer Mn(II) oxidation, with only 28% present as Mn(III), consistent with the higher oxidizing environment in air-EC.

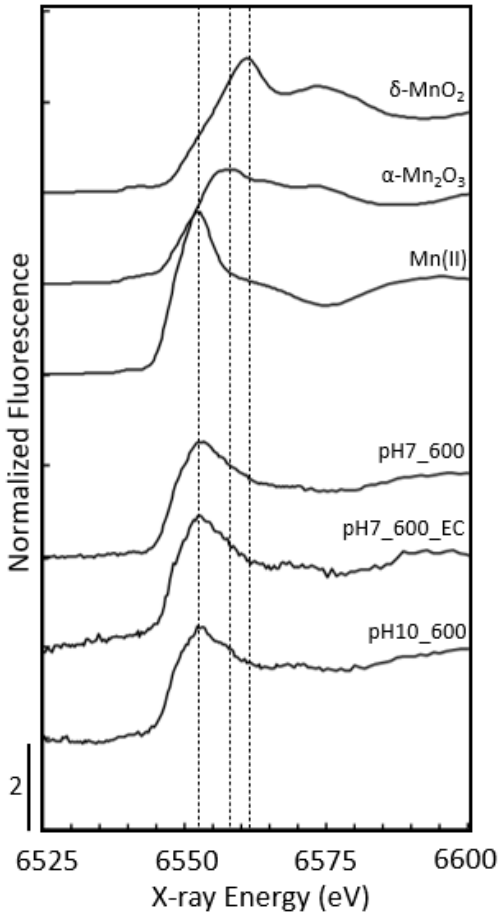


Figure 3.13 Mn K-edge XANES spectra. Vertical dashed lines are placed on the absorption maximum of each reference mineral spectrum.

Table 3.7 Summary of the Mn K-edge XANES LCFs.

Sample ID	Fraction Mn(II)	Fraction Mn(III)	Fraction Mn(IV)	R-Factor
pH7_600	0.59	0.41	0.00	0.032
pH7_600_EC	0.72	0.28	0.00	0.005
pH10_600	0.56	0.45	0.00	0.031

3.3.9 As K-edge XANES and LCFs

The As K-edge XANES spectra are shown in Figure 3.14. The position of the absorption maximum of the samples match that of As(V) adsorbed to 2LFh. As such, the spectra indicate that in the air-EC experiments at all pHs and CDRs, As(III) was effectively oxidized to As(V). However, in conventional Fe-EC (coded as "pH7_600_EC") complete As(III) oxidation was not achieved, as can be observed by the two peaks aligning with both As(III) and As(V) reference spectra. The LCFs (Table 3.8) indicated that in air-EC, most of the surface-bound As (~100%) existed as As(V). In conventional Fe-EC, the majority of As was present as As(III) at 62%, with only 39% present as As(V). Regarding As oxidation state, there were no significant deviations with pH or CDR when using air-EC.

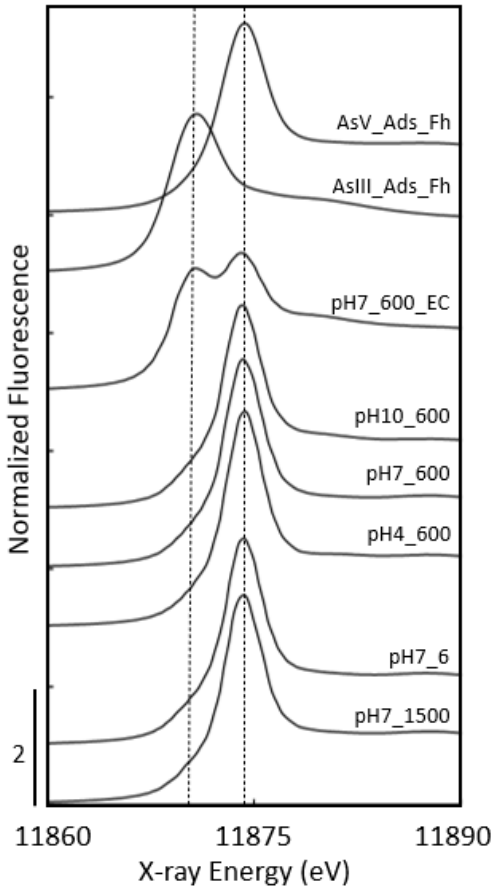


Figure 3.14 As K-edge XANES spectra. Vertical dashed lines are placed on the absorption maximum of each reference spectrum.

Table 3.8 Summary of the As K-edge XANES LCFs.

Sample ID	Fraction As(V)	Fraction As(III)	R-Factor
pH7_600_EC	0.39	0.62	0.001
pH7_600	1.03	0.00	0.002
pH10_600	0.99	0.02	0.002
pH4_600	1.04	0.00	0.004
pH7_6	1.01	0.00	0.002
pH7_1500	1.03	0.00	0.002

3.3.10 As K-edge EXAFS Fourier Transform Shell-by-Shell Fits

All the samples across pH and CDR values were similar in terms of coordination number and interatomic distances for the As–O and As–Fe shells (Figure 3.15). The $N_{As\text{-}O}$ was ~5 and the $R_{As\text{-}O}$ was ~1.70 for all samples, as shown in Table 3.9. For the second shell, the $N_{As\text{-}Fe}$ was ~2.5 for all samples. While the pH 10 sample had a lower fit-derived $N_{As\text{-}Fe}$, this value was not low enough to be considered statistically different than the other samples. For all samples the $R_{As\text{-}Fe}$ was ~3.3 Å, although there were some subtle differences in the longer $R_{As\text{-}Fe}$ of the pH 10 sample (3.32 Å) compared to the pH 7 samples (3.25 – 3.26 Å). An $R_{As\text{-}Fe}$ near 3.3 Å has been identified in previous studies to be due to As(V) bound in a binuclear, bidentate inner-sphere complexes with the electrolytically generated Fe(III) (oxhydr)oxides.[58]

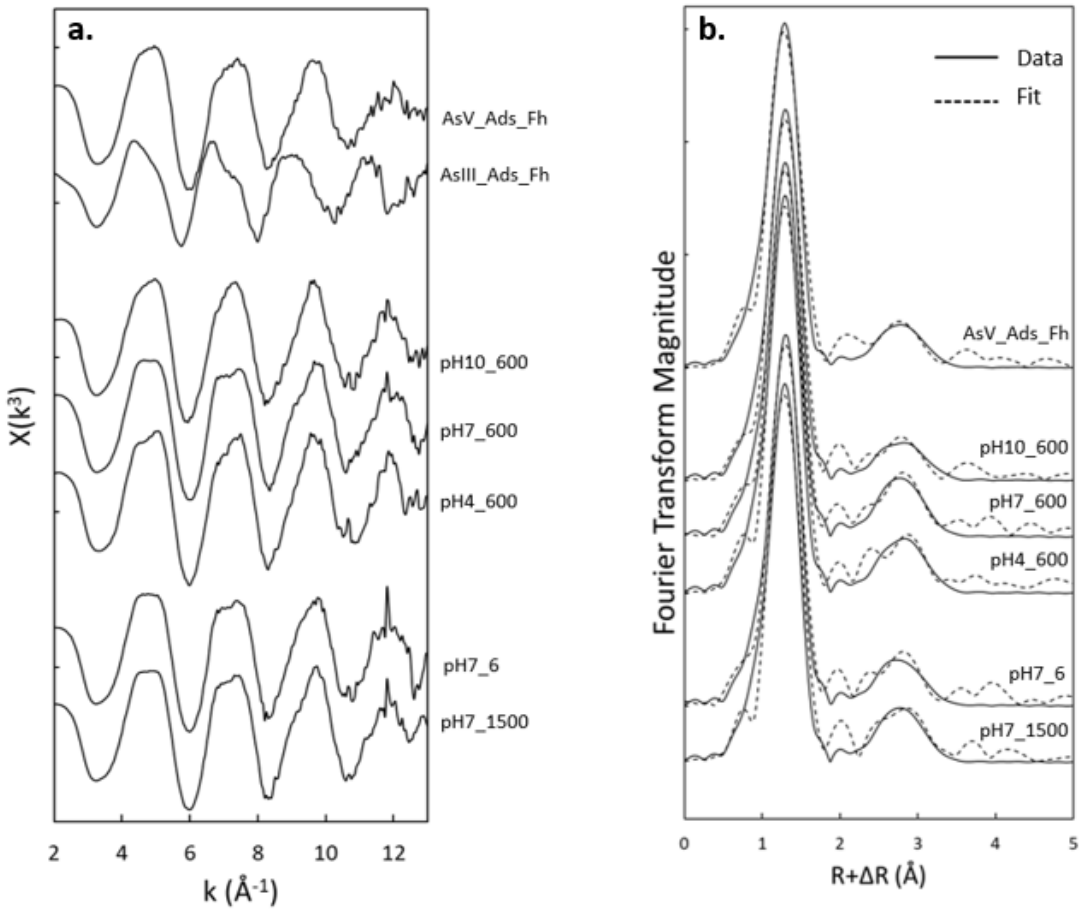


Figure 3.15 As K-edge a) EXAFS and b) Fourier Transform.

Table 3.9 Summary of shell-by-shell fitting results for As.

Sample	Atomic Pairs	N	R(Å)	σ^2 (Å^2)	ΔE_0 (eV)	R-factor
2-Line Ferrihydrite Adsorbed As(III)	As–O	3.4 (0.4)	1.79 (0.00)	0.003 (0.001)	11.0 (0.1)	0.036
	As–O–O	6	3.26	Sig (As–O)		
	As–Fe	1.5 (0.4)	2.94 (0.02)	0.01		
2-Line Ferrihydrite Adsorbed As(V)	As–O	5.2 (0.5)	1.69 (0.01)	0.005 (0.001)	5.3 (1.7)	0.021
	As–O–O	12	3.08	Sig (As–O)		
	As–Fe	1.9(0.6)	3.28 (0.02)	0.01		
pH10_600	As–O	5.0 (0.4)	1.70 (0.01)	0.004 (0.001)	5.3 (1.5)	0.018
	As–O–O	12	3.09	Sig (As–O)		
	As–Fe	1.7 (0.6)	3.32 (0.03)	0.01		
pH7_600	As–O	4.9 (0.4)	1.69 (0.00)	0.003 (0.001)	5.2 (1.5)	0.016
	As–O–O	12	3.08	Sig (As–O)		
	As–Fe	2.7 (0.6)	3.25 (0.02)	0.01		
pH4_600	As–O	5.2 (0.5)	1.69 (0.01)	0.003 (0.001)	5.4 (1.6)	0.020
	As–O–O	12	3.08	Sig (As–O)		
	As–Fe	2.5 (0.7)	3.29 (0.02)	0.01		
pH7_6	As–O	4.7 (0.4)	1.69 (0.00)	0.003 (0.001)	5.6 (1.5)	0.016
	As–O–O	12	3.09	0.003		
	As–Fe	2.2 (0.6)	3.26 (0.02)	0.01		
pH7_1500	As–O	5.2 (0.5)	1.69 (0.01)	0.004 (0.001)	4.1 (1.8)	0.023
	As–O–O	12	3.08	Sig (As–O)		
	As–Fe	2.5 (0.7)	3.26 (0.02)	0.01		

3.4 Discussion

3.4.1 Fe Phase Generated in SCaGW as a Function of pH and CDR

The Fe K-Edge EXAFS spectra (Figure 3.11) showed a subtle qualitative difference in line shape (small peak at 7.5 $Å^{-1}$) for the pH 10 sample spectrum, as compared to the pH 7 spectra. However, the LCFs (Table 3.5) indicated that there were no significant differences across the samples. The slightly higher CN_{Fe-O} for sample 10 (~6.7 as opposed to 5.6 to 5.9) was also not sufficiently significant to describe different Fe(III) precipitate structures. For the Fe data, only poorly ordered solids were observed as a result of polymerization in the presence of a complex groundwater containing bivalent cations and oxyanions.[77,115] This disorder is also indicated by the characteristic broad peaks in the XRD (Figure 3.6) representative of HFO across pH 4, 7 and 10 samples at all CDRs. At pH 10 the diffractograms exhibit more resolved peaks with a noticeable peak at around 80º 2θ. These features were not observed in the other pHs, which indicates a less disordered structure at pH 10.

However, the high concentration of Fe (3.1 mM) dosed into the system yielded ratios of oxyanions and bivalent cations that were quite small. Phosphate and silicate, which typically inhibit polymerization and yield oligomers, were not present at a high enough ratio with respect to the total solid that would significantly impact the structure. Kaegi et al., 2015 had found that HFO was formed at Si/Fe ratios >0.5.[113] In this present study, the maximum ratio was 0.2 (Table 3.4). These smaller ratios may allow for a lower degree of nanocrystallinity, as can be seen in the LCFs of the Fe EXAFS (Table 3.5), in which there is a significant presence of 2LFh in addition to HFO. As such, these results indicate the presence of the less nanocrystalline structure, 2LFh, in addition to highly disordered HFO.

The wet chemical data show much less As adsorption onto the solids, with up to a 19% decrease in the As:Fe solids ratio from pH 4 to pH 10 (Figure 3.3). The decrease in As removal can be explained by the change in the surface charge of the Fe(III) precipitates past its reported point of zero charge (PZC), which has been reported as 7.8.[116] Consistent with the behavior of As removal, P removal worsened from pH 4 to pH 10 (Figure 3.4), with the P:Fe solids ratio decreasing from 65 to 54 µg/mg (Table 3.3). It has been reported in previous studies how the presence of oxyanions like As(V) and P will disrupt polymerization of Fe(III) precipitates, resulting in nanocrystalline shorter-ranged structures.[60] As such, with less adsorption of As onto the solids at pH 10, a more-ordered average Fe bonding environment (but still highly nanocrystalline) was expected.

Lower efficiencies of H_2O_2 production at low CDRs[66] indicate that Fe(II) may not only be oxidized by H_2O_2, but also by the dissolved oxygen. This low CDR signifies a longer treatment time of 100 minutes for the 600 C/L dose. As such, there is a greater reliance on dissolution of atmospheric O_2 during Fe(0) electrolysis. This was a major difference between the Fe precipitates generated at faster CDRs of 600 and 1500 C/L/min, for which the reaction times were only 1 min and 24 sec, respectively. Another influence from the long reaction time would be higher CO_2(g) equilibration, especially at pH 4 at which CO_2(g) exsolution would be higher. CO_2(g) dissolution and exsolution at the higher CDRs is not expected to be significant at such short electrolysis times.

Moreover, the Fe(II) production rate is directly affected by the CDR of 6 C/L/min, which corresponds to 0.03 mM/min, a rate that is about 100 and 250 times slower than the production

rates at 600 (3.11 mM/min Fe(II)) and 1500 C/L/min (3.11 mM/min Fe(II)), respectively. The fast rate of Fe(II) production and such fast oxidation kinetics also does not allow for ordered species (600 and 1500 CLM occurred within 1 min and 24 seconds, respectively). When compared to Fe(II) oxidation by DO, the presence of H_2O_2 speeds up the reaction by over four orders of magnitude.[62,105,117] Previous studies showed that highly disordered Fe(III) phases are generated from Fe(II) oxidation with H_2O_2. This was observed in previous studies in the difference between the Fe precipitates being generated when Fe(II) oxidation relies on H_2O_2 instead of O_2.[102,103,118]

3.4.2 Effect of pH and CDR on Mn removal

The XANES data (Figure 3.13) showed that the Mn in the solid phase was found mostly as Mn(II) phase at ~60%, but with also a large component of Mn(III) at ~40% at pH 7 and 10 (Table 3.7). Compared to the complete oxidation of As(III), these results indicate that Mn(II) is not a strong competitor for the reactive oxidant species generated in the system. The increase in Mn(II) removal efficiency with increasing pH (and lack of removal at pH 4) can be explained by concurrent surface phenomenon as well as by the role of the reactive intermediates across pH levels. The type of oxidant can be attributed mostly to ·OH at pH 4, and more dominantly by Fe(IV) at pH 7 and 10.[102] The negative surface charge above the PZC of the oxyanion-rich Fe(III) solids enhances the removal of positively charged Mn(II) at high pH. However, the same fractions of Mn(II) and Mn(III) at pH 7 and pH 10 indicate that the reactive intermediates generated are able to oxidize a fraction of Mn(II) in solution.

As a result of incomplete Mn(II) oxidation, Mn(II) sorption onto Fe(III) precipitates appears to be a dominant removal mode in air-EC. This interpretation is justified by the data showing increased removal with increasing pH, where surface-bound Mn would be highest. This removal mode is enhanced even more in conventional Fe-EC where only ~30% of Mn(II) was oxidized to Mn(III). A previous study investigating the reaction products of electrocoagulation systems found Mn(III) to be partially incorporated into electrolytically generated Fe(III) precipitates in solutions containing bivalent cations and oxyanions, when Mn(II) was oxidized by O_2 and HOCl.[104] A separate study also suggested Mn removal through Mn(III) substitution for Fe(III) octahedra in the Fe(III) coprecipitates.[102] Mn(III)-incorporated HFO is a possible partial uptake mechanism in air-EC, but the data presented in this present study does not provide evidence for this local coordination.

In contrast to a previous study that found CDR to play a significant role in Mn(II) oxidation efficiency[102], in air-EC there exists only a subtle trend at pH 7, with Mn(II) removal increasing from 6 to 1500 C/L/min (Figure 3.2b). The previous study also found Mn(II) to be an important sink of reactive oxidants in a NaCl background electrolyte or HCO_3^- buffer. However, in this present study, complete oxidation of Mn(II) was not achieved in the presence of bivalent cations, oxyanions, and NOM. Similar to the previous study, a higher fraction of Mn(II) was oxidized to Mn(III) in the air-EC (which generates H_2O_2 *in-situ*) as opposed to conventional Fe-EC that relies on the modified Fenton reaction. However, the iron production rates in air-EC (30 – 7770 μM/min) were 6 to 155 times higher than operating conditions in conventional EC (where the iron production rates were 5 – 50 μM/min). Also, the total Fe dose in this current study was 3.1 mM, about 16 times greater than the 200 μM dose in the previous study.

3.4.3 Effect of pH and CDR on As removal

The As K-edge XANES data (Table 3.8) indicate that complete As(III) oxidation was achieved for all CDRs and pH, with only As(V) present, suggesting that As(III) more strongly competes for reactive oxidant species than Mn(II). As seen through the wet chemical data (Figure 3.2a), As removal decreased as pH increased. The worse removal at pH 10 cannot be explained by dissolved iron passing through 0.2 μm filters. It was observed that more dissolved iron was present in filtered samples at pH 4, at which As removal was best. The dissolved iron passing through filters was less than 5% of total iron in solution at the end of electrolysis. As argued in the section above, As removal is not as effective at pH 10 likely due to the negatively charged Fe(III) precipitates past its PZC and consequent electrostatic repulsive forces against negatively charged As-oxyanions.

Delaire et al., 2017 found that the CDR in conventional Fe-EC impacts the process limiting As removal (i.e., As(V) adsorption or As(III) oxidation) depending on the pH.[74] At pH 7 there appears to be the most clear trend with CDR. For As removal with air-EC, increasing CDR decreases removal efficiency, despite increases in H_2O_2 production efficiencies with increasing CDR.[66] Regardless, As(III) oxidation does not change across CDR (Figure 3.14). The total dose of 600 C/L is high enough and the adsorption sites are sufficiently available for As adsorption to take place. The Fe, Mn and As XAS data were similar for all samples, suggesting similar removal pathways, regardless of pH and CDR. While the reactive intermediates generated vary according to pH,[57,102] the Fe phase and Mn and As species in the reaction products were consistent across the probed samples.

3.4.4 Technical and Environmental Implications

The results of this study suggest that air-EC is adaptable to the needs of a particular community, whether in rural California or Southeast Asia. The way in which As is adsorbed to the electrolytically generated iron (oxyhydr)oxides does not change across the dosage rates (6, 600, 1500 C/L/min). A system located in a community with intermittent grid power may choose to operate the system at a higher throughput to quickly treat the required volume to serve their community. Alternately, air-EC could be also powered by solar P.V. cells. Under these conditions, the system may be constrained to a smaller current, and thus may be limited to a lower CDR or long electrolysis times.

As(III) was selected as the species of As to remove in order to challenge the system and demonstrate its efficacy across the operating conditions. However, real California aquifers do not typically contain such high concentrations of only As(III). For water systems out of compliance, concentrations may only be slightly higher than 10 μg/L, and the speciation of As may include a significant amount of As(V). In these environments, the As(III/V) species would pose less competition for the reactive oxidant species in the reactor. Moreover, if a groundwater source contains mostly As(V), a low CDR, which has a lower H_2O_2 production efficiency, will still allow for effective removal without dependence on reactive oxidant species. Under these conditions it may also be acceptable to yield a lower residual of H_2O_2 in the product water.

Air-EC is a promising system to treat high levels of As and Mn in drinking water sources. While this study suggests that air-EC can work as an effective modular electrochemical system for removal of both As(III) and Mn(II) removal, the removal efficacies for As and Mn depend on the

pH with inverse trends. These inverse trends of As and Mn removal efficacy suggest that pH levels should be constrained to circumneutral pH levels. Furthermore, treatment at circumneutral pH showed no drift in the pH, which avoids post-pH adjustment steps that would otherwise be required in field treatment. However, a challenge remains at pH 7 in which Mn (starting with 1000 μg/L) was not lowered to below its secondary MCL (of 50 μg/L). Increasing the iron dose may not be the optimal solution, as the increased sludge generation can become a barrier to scale-up. Field testing would require selecting the minimum dose, below the ~170 mg/L of Fe selected for this study, to generate less sludge per treated volume. Additional treatment steps post-electrocoagulation, such as oxidative filtration, may be required to lower Mn concentrations below the standard.

Future work should investigate high Mn(II):As(III/V) ratios to probe the different removal pathways. Reducing the Fe dose may reveal underlying reaction pathways that were not observed due to potential autocatalytic oxidation on Fe(III) surfaces. Furthermore, the stability of the As- and Mn-laden Fe precipitates and leachability in realistic disposal conditions remains to be investigated.

Chapter 4. Investigating Performance of Modified Gas Diffusion Layer in Air-EC

4.1 Introduction

In a new paradigm for water systems, experts have envisioned a decentralized approach to water treatment considering both the individual household and community scale needs.[119] This alternative approach can provide more utility and empowerment to each community facing water quality challenges. Electrochemical water-treatment technologies may accelerate and allow this shift in thinking on water systems. Electrochemical systems can be designed to handle different types of water sources, are easily modularized, and may be integrated within existing treatment trains or function as standalone systems.[120]

In advanced oxidation processes (AOPs) for water treatment, the use of H_2O_2 as an oxidant has various advantages, such as being environmentally friendly with only water and oxygen as decomposition products.[121] However, the primary mode of H_2O_2 production is currently through the anthraquinone process which demands large infrastructure and results in large amounts of organic waste products.[122–124] Another approach to generate H_2O_2 is through directly synthesizing with a hydrogen and oxygen mixture in the presence of catalysts, but is a potentially explosive process.[125] The high volumes of concentrated (70 wt %) H_2O_2 that are transported from centralized facilities also present a safety hazard. A decentralized approach to H_2O_2 production is desirable in order to avoid the use of stabilizers preventing H_2O_2 decomposition, to generate concentrations that are more useful for the particular application (e.g., <0.1 wt% for water treatment), and to minimize accidents during transportation.[126,127]

The electrochemical production of H_2O_2 through a fuel cell configuration, has been explored as a safer and decentralized approach, and has been reported for treatment of acidic wastewaters containing persistent organic pollutants.[128,129] The process follows a two-electron reduction of oxygen (Equation 1), known as the oxygen reduction reaction (ORR), at the cathode to produce H_2O_2 with a standard redox potential (E^o) of 0.68 V/SHE.[130]

$$1.\quad O_2 + 2e^- + 2H^+ \rightarrow H_2O_2$$

However, the materials used as the cathode, such as noble metals like palladium (Pd) and gold (Au), are scarce and expensive. Moreover, carbon-based materials, such as carbon felt, and carbon sponge are abundant and stable throughout operation, but may have low H_2O_2 generation efficiencies.[125,130] For effective water treatment applications, the carbon-based material must be characterized with high selectivity for the $2e^-$ ORR, low amounts of H_2O_2 decomposition, and sustained stability.[130]

Gas diffusion layers (GDLs) using carbon materials have proved to be effective options for high yields of ORR. Prior GDLs relied on the aeration of the electrolyte or direct pumping of oxygen through the electrode, resulting in high energy consumptions and subsequent increased operation costs. While GDLs, or air cathodes, have been reported in Microbial Fuel Cells for wastewater treatment for about the past two decades, their use in geogenic contaminant removal (such as arsenic) has only recently been reported.[129,63,66]

Much of the literature on electrochemical arsenic removal reports on iron electrocoagulation (Fe-EC), which has been shown to be an effective remediation technology both

at bench- and pilot-scale.[59,97,100,131] Field studies of Fe-EC have reported on the formation and growth of macroscopic surface layers on the iron electrodes, which negatively impact the anodic dissolution of Fe^{2+} and subsequent ionic diffusion into the bulk.[76,132] It was found that the formation of a surface layer containing calcite and Fe(III) precipitates caused the Faradaic Efficiency (*FE*) of Fe^{2+} production to decrease to about 10% (while *FE* is reported at >85% in the absence of these surface layers).[133] The presence of Fe and other bivalent cations and oxyanions, may cause similar performance issues at the GDL when adapted to an Fe-EC process.

To exploit the *in-situ* production of H_2O_2 for effective removal of contaminants that rely on Fenton-type reagents, a carbon-based GDL, or air cathode, was incorporated into a Fe-EC system. The GDL was further modified with carbon black (CB) and graphite layers to enhance the favorable catalytic reactions for H_2O_2 production. Also, this air-EC configuration enhances oxygen transfer through its catalytic interface without additional aeration.[123,134] In this work, the impact of air-EC operating conditions in a complex synthetic groundwater matrix on cathode performance was investigated. Various characterization techniques, including Scanning Electron Microscopy (SEM) and Energy Dispersive X-ray Spectroscopy (EDS), were used to elucidate morphological attributes of the GDL base, newly modified- and used cathodes, and respective atomic compositions. Synchrotron-based X-ray absorption spectroscopy and X-ray fluorescence mapping were performed to obtain the elemental distribution and chemical speciation of iron and calcium present on the cathode after use in the air-EC system. Raman Spectroscopy and X-ray Photoelectron Spectroscopy (XPS) were employed to offer potential mechanistic explanations for efficiencies and losses in H_2O_2 production.

4.2 Materials and Methods

4.2.1 Cathode Fabrication

A carbon fiber paper (AvCarb P75T, FuelCell Store) was used as the GDL base for further modification. This material is treated with polytetrafluoroethylene (PTFE) at 13 wt%, and has a nominal thickness of 0.255 nm.[135] The carbon material was cut into 100 cm^2 squares and 600 mg of graphite powder (synthetic, conducting grade, -200 mesh, 99.9995% purity, Alfa Aesar) was mixed with 2 mL of a PTFE preparation, 60 wt% dispersion in H_2O (Aldrich, CAS 9002-84-0). Each modified cathode was prepared as follows. A paint brush was used to cover the prepared slurry on one side of the carbon fiber paper and was allowed to dry for 20 minutes at room temperature. Afterwards, this "air-facing" side was sintered at 350 ºC for 40 minutes. The carbon fiber paper with the applied graphite slurry was taken out of the furnace and allowed to cool for 20 minutes. A mixture of 150 mg of carbon black (CB) (Black Pearls 2000, Cabot, CAS 1333-86-4), 83 µL of PTFE solution, and 2.917 mL of 1-propanol (Acros Organics, CAS 71-23-8) was then painted on to the "water-facing" side, followed by 20 minutes of air drying and subsequent 40 minutes of sintering at 350 °C. This preparation method is described in Barazesh et al., 2015. The air cathode was allowed to cool to room temperature before electrolysis experiments. The cathodic active area in experiments was 64 cm^2.

4.2.2 Faradaic Efficiency Tests

The Faradaic Efficiency (*FE*), or how efficiently the charge transferred is directed towards the desired reaction, of H_2O_2 production was selected as a performance metric for the cathode in air-EC. The *FE* of the air cathodes was determined from the following equation:

$$2.\quad FE = \frac{nFVC_{H2O2}}{It} \times 100\%$$

in which n is the number of electrons (2) transferred for the oxygen reduction reaction (ORR) to occur, F is Faraday's constant (96,485 C/mol), V is the reactor volume in L, C_{H2O2} is the H_2O_2 concentration in mol/L, I is the current (A), and t is time in seconds.

To measure the *FE* of cathodic H_2O_2 production, a 1 mL volume of sample was taken from the catholyte and mixed with 2 mL titanium (IV) oxysulfate solution (Sigma Aldrich, CAS 13825-74-6). Depending on the H_2O_2 concentration, this forms varying degrees of yellow tinted solutions. A colorimetric method, as described in Barazesh et al., 2015, was used to measure the concentration of freshly generated H_2O_2. These measurements were performed with a Hach DR 6000 UV-spectrophotometer and the titanium sulfate method to measure the absorbance at wavelength 405 nm.

The initial and final *FE* of each cathode (at new and used states) were measured at coulombic dosage rates (CDRs) of 6, 600, and 1500 C/L/min as batch processes, corresponding to current densities of 0.20, 20.3, and 50.8 mA/cm^2, respectively. The tests conducted at 600 and 1500 C/L/min were performed for a total dose of 600 C/L, corresponding to electrolysis times of 1 min and 24 sec, respectively. The tests conducted at 6 C/L/min were performed only up to 100 C/L, corresponding to an electrolysis time of 16 min 46 sec, to decrease the contact time of the cathode with the high ionic strength solution as a preventative measure on early precipitation of salts onto the cathode.

4.2.3 Reactor Configurations

The air-EC system was operated as either a two-chamber or single-chamber batch reactor, employing a single modified GDL (as described above) as the cathode. The electrochemical cell (Figure 4.1) was assembled using high density polyethylene (HDPE) plates to hold a total volume of 260 mL with an anion exchange membrane (AEM) (FuMA-Tech, Fumasep FAS-PET-130) separating the catholyte (130 mL) from the anolyte (130 mL).[64] While AEMs are characterized by positively charged functional groups, proton transport can still occur.[136] A titanium frame surrounds the cathode, serving as a current collector. A mixed metal oxide (MMO) electrode composed of Ir-O_2 and Ru-O_2 was selected for its use as an inactive anode and high catalytic activity for water oxidation across wide current densities without substantially increasing cell voltages.[137,138] This two-chamber system was only used to conduct *FE* experiments, to measure cathode H_2O_2 production efficiency at new and used cathode states. Also, the AEM prevents the H_2O_2 generated at the cathode from reacting at the anode. Moreover, an Fe anode was not necessary to be used in the two-chamber system, which would otherwise cause quick fouling of the AEM from the precipitates that would form within the anolyte.

To operate the system as a single chamber system, the AEM was removed and the MMO electrode replaced with a low-carbon steel (1006−1026 steel grade, McMaster-CARR), to allow for the anodic dissolution of Fe and subsequent reactive precipitate formation for contaminant removal, as described in the companion study (Chapter 3). The newly modified- and used cathodes were characterized before and after prolonged use, respectively, in the single chamber system.

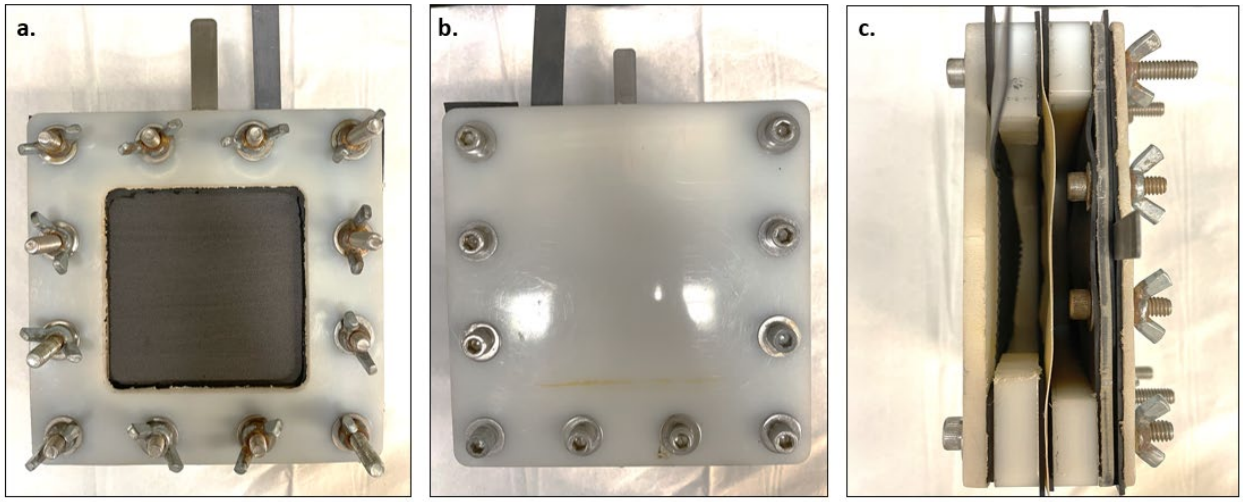


Figure 4.1 Digital photographs of a) front view of air-EC reactor showing the air-facing (graphite layer), the titanium current collector, and 10 bolts, washers, and wing nuts, b) back view of reactor comprised of a HDPE plate fitted with 10 bolts and washers, and the MMO anode, c) top view of reactor showing the modular components tightened together with gaskets between each HDPE sheet to create a leak-proof system. The flexible light-yellow material in the middle is the AEM that creates a two-chamber system.

4.2.4 Electrolyte Compositions

A conductive solution for the H_2O_2 *FE* experiments consisted of 15.6 mM Borate Buffer, 100 mM NaCl, 200 mM $NaClO_4$, and 500 mM Na_2SO_4. A 1.25 M Borate Buffer solution was first prepared by adding 23.84 grams of $B_4Na_2O_7 \cdot 10H_2O$ (Fisher Bioreagents, CAS 1303-96-4) and 61.83 grams of H_3BO_3 (Fisher Chemical, CAS 10043-35-3) in 1 L of Milli-Q water (18.2 mΩ·cm at 25 °C). Additionally, 1 M stock solutions of NaCl (Alfa Aesar, CAS 7647-14-5), Na_2SO_4 (Alfa Aesar, CAS 7757-82-6), and $NaO_4Cl \cdot H_2O$ (Fisher Chemical, CAS 7791-07-03) were prepared. A 30% H_2O_2 solution (Sigma-Aldrich, CAS 7722-84-1) was used as a standard for the calibration curves.

In a companion study (Chapter 3), a series of As(III) and Mn(II) removal experiments using air-EC were performed in a synthetic California groundwater containing 2 mM HCO_3^-, 0.75 mM Ca^{2+}, 0.32 mM P, 1.03 mM Mg^{2+}, 0.06 mM NO_3^-, 10.41 mM SO_4^{2-}, 0.02 mM Mn^{2+}, 0.02 mM As, and 3 mg/L fulvic acid.

4.2.5 Cathode Characterization

Scanning electron microscopy (SEM) was used to observe changes in morphology of the cathode surface before and after the addition of catalysts, and after 40 batch experiments in the synthetic California groundwater. This corresponds to 4260 Coulombs passing through the active area of the cathode (~70 Coulombs/cm^2) exposed to synthetic groundwater, and a total of 6190 Coulombs passing through the electrode (~100 Coulombs/cm^2) including the pre- and post- *FE* testing in the Borate Buffer solution. A Zeiss-EVO scanning electron microscope was used in high vacuum mode at 20 kV, and backscatter electron (BSE) detectors were also used for energy dispersive x-ray spectroscopy (EDS) analyses for better identification of the main elements of each sample. A PANalytical X'Pert PRO MPD with a Co X-ray source was used to collect X-ray diffractograms. Moreover, a Horiba LabRAM Aramis Raman microscope with a 532 nm laser wavelength was used to identify the D and G modes of the cathode samples. X-ray photoelectron spectroscopy (XPS) measurements were performed with a Thermo Scientific K-Alpha XPS

apparatus, monochromatic Al K(alpha) source, and a flood gun for charge compensation. Background subtraction, normalization, and multiple peak fitting of the Raman and XPS spectra were performed using OriginPro 2022b software (OriginLab Co., Northampton, MA, USA).[139]

Synchrotron-based X-ray fluorescence microprobe measurements were conducted at ALS XFM 10.3.2 of the Advanced Light Source (ALS), Lawrence Berkeley National Laboratory (LBNL), Berkeley, CA, USA.[140] Micro-focused X-ray fluorescence (μXRF) mapping of calcium (Ca) and iron (Fe) was performed 100 eV above the Ca and Fe K-edges (4138 eV and 7210 eV, respectively) with the sample placed at 45º to the incident beam. Maps were acquired using pixel sizes of 20×20 μm (coarse mapping) and 5×5 μm (fine mapping) with a dwell time of 0.26 ms. To determine the chemical speciation of calcium, micro-focused x-ray absorption near-edge structure (μXANES) spectra were recorded in QXAS mode on specific regions of the samples, using a Si(111) monochromator. Spectra were calibrated using a gypsum ($CaSO_4$) standard with a main peak set at 4049.77 eV. All data were recorded in fluorescence mode in ambient conditions with a 7-elements silicon drift detector (Canberra/Mirion). All data were processed using a suite of LabVIEW programs (National Instruments, Austin, TX, USA) available at beamline 10.3.2.

4.3 Results and Discussion

4.3.1 Faradaic Efficiencies for H_2O_2 Production

Initial *FE* values of newly prepared cathodes were found to be 81 ± 4%, 80 ± 4%, and 28 ± 1% for CDRs of 1500, 600 and 6 C/L/min, respectively (Figure 4.2). At the highest *FE*, the H_2O_2 concentration was ~2.51 mM, and ~0.87 mM at the lowest *FE*. After performing a series of experiments, the cathode was characterized with efficiencies of 37 ± 3%, 41 ± 3%, and 9 ± 4% for 1500, 600 and 6 C/L/min, respectively. These values correspond to ~0.26 mM to ~1.27 mM H_2O_2 for the lowest and highest *FE*s, respectively. Moreover, these values signify about a 40% decrease in *FE* for CDRs of 1500 and 600 C/L/min, and about a 20% decrease for the 6 C/L/min CDR.

FE results at less than 100% may be due to parasitic reactions at the surface of the cathode, disproportionation of H_2O_2 to O_2 once in the bulk solution, or oxidation of H_2O_2 at the anode.[130] Equation 3 below shows the competitive $4e^-$ reaction that can occur and Equations 4 – 7 below show reduction of H_2O_2 at the cathode surface and the disproportionation reaction:

3. $O_2 + 4H^+ + 4e^- \rightarrow 2H_2O$
4. $H_2O_2 + 2H^+ + 2e^- \rightarrow 2H_2O$
5. $2H_2O_2 \rightarrow O_{2(g)} + 2H_2O$
6. $H_2O_2 \rightarrow HO\cdot_2 + H^+ + e^-$
7. $HO\cdot_2 \rightarrow O_2 + H^+ + e^-$

The much lower *FE*, at both new and used conditions, can be explained by H_2O_2 reduction occurring at the surface of the electrode, as the AEM prevents interactions at the anode. Moreover, at low CDRs, or low potentials, O – O dissociation of H_2O_2 faces a large kinetic barrier.[127] The $2e^-$ reduction pathway includes OOH* as the sole intermediate prior to H_2O_2 formation.[141] The conversion of H_2O_2 to ·OH has been observed as a possible degradation route in previous studies[124], but the data presented here cannot confirm that mode.

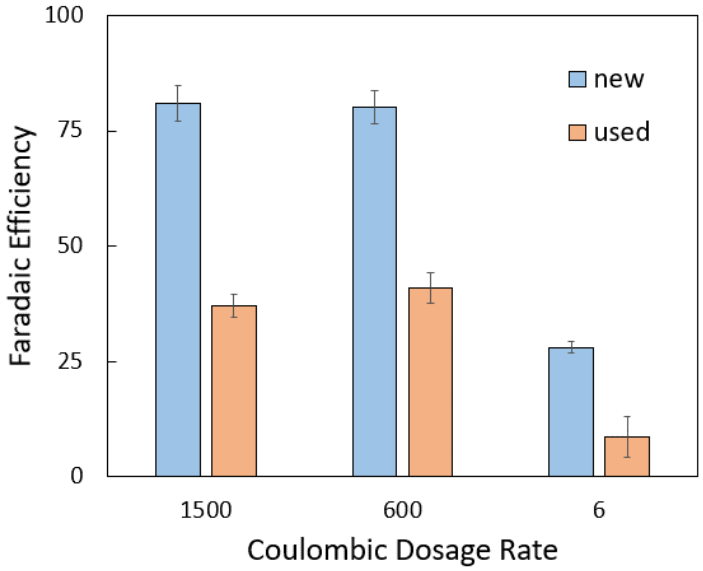


Figure 4.2 Comparison of *FE* for H_2O_2 production in air-EC of new and used cathodes operated at three selected dosage rates (1500, 600 and 6 C/L/min).

The initial pH and DO values of the buffer solution used for *FE* tests were 7.92 ± 0.04 and 9.45 ± 0.51, respectively. As seen in Figure 4.3, in in the new cathode condition, the catholyte pH increased to 8.35 ± 0.01, 8.92 ± 0.03, and 8.91 ± 0.04 at CDRs of 6, 600, and 1500 C/L/min, respectively. A similar change in pH was observed for the used cathode condition. The pH increase was expected as the ORR is a proton consuming process that yields alkaline environments (Equation 1).[142] Also, the maximum final pH recorded was around 9, much below the pK_a of H_2O_2 at 11.64 (with the conjugate base being HO_2^-, hydroperoxide ion).[130] As such, the 1 unit increase in pH would not pose as a detriment to the *FE* due to deprotonation. On the other hand, at 6, 600, and 1500 C/L/min, the anolyte chamber pH decreased to 3.69 ± 0.02, 2.98 ± 0.13, and 3.01 ± 0.02, respectively, for the new cathode condition (Figure 4.3). This behavior was also observed in the used cathode condition, except at 6 C/L/min, at which the pH was almost 4 units higher than the new cathode results. While the catholyte and anolyte chambers become alkaline and acidic, respectively, during regular operation of the air-EC system without an AEM, initial circumneutral pH did not show to fluctuate during treatment.[66]

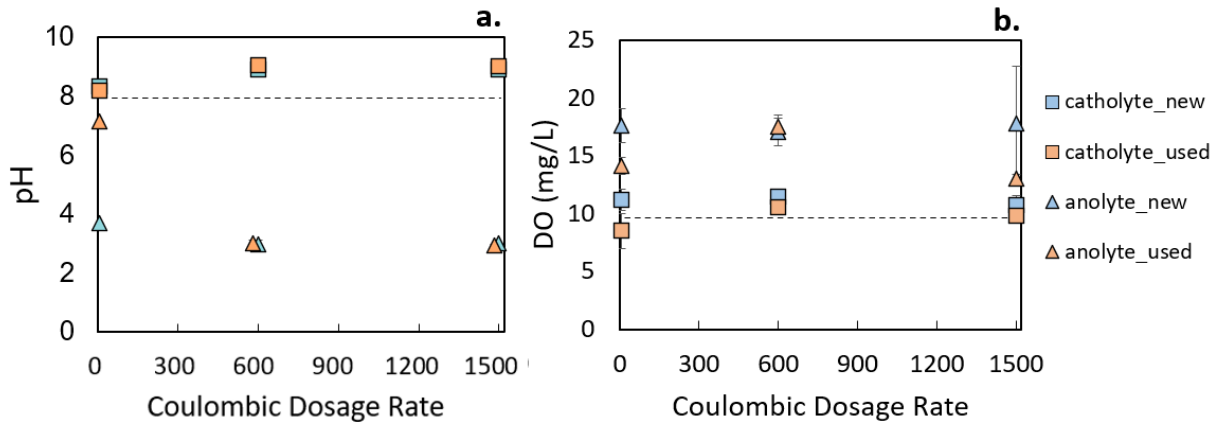


Figure 4.3 pH and DO values of catholyte (squares) and anolyte (triangles) chambers for new (blue-colored markers) and used (orange-colored markers) cathodes at the end of electrolysis. The dotted line represents the initial average pH and DO values of the electrolyte. In panel a, the orange triangle markers are slightly shifted in the x-axis to make the blue markers visible.

Moreover, there was a slight increase in DO from the average initial concentration in both the new and used catholyte chambers, but no trend was observed with CDR. The final DO values for the new cathode condition were 11.23 ± 0.92 mg/L, 11.52 ± 0.12 mg/L, and 10.76 ± 0.86 mg/L for CDRs of 6, 600, and 1500 C/L/min, respectively. This increase in DO can be explained by Equation 3, disproportionation of H_2O_2 on the cathode itself. The final DO values for the used cathode condition were slightly lower at 8.54 ± 1.5, 10.59 ± 0.21, and 9.83 ± 0.19 mg/L for 6, 600, and 1500 C/L/min CDRs. This decrease in final DO may be due to less H_2O_2 production yielding less decomposition into O_2, particularly at 6 C/L/min, which resulted in a final DO less than the initial solution value. The anolyte DO concentration increased to quite high values, above 13 mg/L for all CDRs and in both new and used cathode conditions. An explanation for this increase would be the oxidation of H_2O to form O_2 on the mixed metal oxide anode, which has been observed as a parasitic reaction in Fe-EC systems.[143,144] However, the decomposition of H_2O_2 to O_2 does not offer an explanation as the AEM does not allow H_2O_2 into the anolyte chamber.

4.3.2 Macroscopic Surface Layer Properties

Figure 4.4 shows pictures of the carbon fiber paper purchased as a GDL base, the modified GDL with carbon black (CB) and PTFE post-sintering, and a used cathode. The purchased GDL base had lightweight and flexible qualities, somewhat similar to conventional printer paper. In the process of cutting the larger sheets to smaller area needed for further modification, tearing would occur if insufficient care was taken. The process of applying the additional CB (water-facing side) and graphite (air-facing side) layers made the surfaces somewhat non-uniform. As seen in panel b below, the edges appeared to contain less CB. This was due to the masking tape used to fasten the carbon paper to the bench surface. While the entire cathode was 10 x 10 cm^2, the actual active area exposed to the electrolyte was only 8 x 8 cm^2. As such, the quality of the edges in the picture did not impact performance of the reactor.

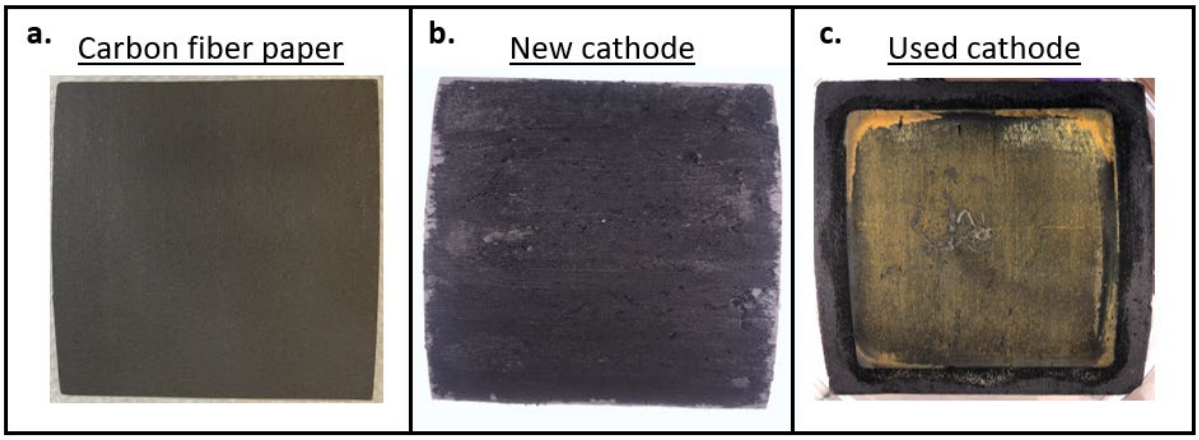


Figure 4.4 Digital photographs of the a) as-purchased carbon fiber paper, b) a newly modified cathode (the CB water-facing side), and c) a used cathode after a 40-experiment series, as representative samples for various characterization techniques.

However, the active area of the cathode visibly showed some heterogeneity due to the application of the CB and PTFE slurry with store-bought paint brushes. The degree of apparent clumps of CB/PTFE may also vary across the prepared cathodes. However, the similar *FE* values across cathodes indicate that our fabrication approach allows for reproducibility of initial cathode performance. Moreover, the used cathode had a visible orange layer, like the color of the iron precipitates generated at the anode during electrolysis (when operating as a single chamber system). There was a greater accumulation of the orange layer at the top corners of the cathode, which are closer to the electrolyte and atmosphere interface. There is a lighter yellow and white tint below the right corner, which suggests a different mineral or salt that has deposited on the material. To a lower degree, there was also accumulation of the orange particles on the lower corners of the cathode. There also appeared to be some scratches in the middle of the cathode, which were likely due to the overhead stirrer used during experiments occasionally grazing the electrode surface. Other than these factors, there was no observed evidence of major mechanical degradation of the used cathode, or of its CB and graphite coatings.

4.3.3 Impact of Modification and Use on Morphology and Atomic Composition

Figure 4.5 shows micrographs of carbon fiber paper, new cathode, and used cathode. The as-purchased carbon fiber paper was shown to comprise disorganized fibers stacked and interwoven to create large pores in the matrix that allow for O_2 diffusion. Applying the CB and PTFE in the modification process caused those macropores to be filled in with the slurry. However, there still appears to be a degree of microporosity to allow O_2 exchange from the atmosphere. The used cathode is characterized by different topographic regions. In the center of the SEM image in panel c, the original CB layer is visible, but is surrounded by new deposits.

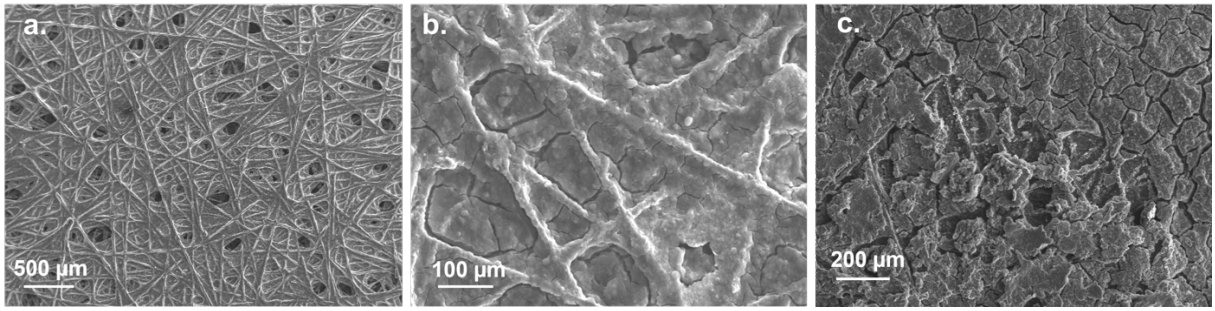


Figure 4.5 SEM images of a) as-purchased carbon fiber paper, b) newly modified cathode (the CB water-facing side), and c) used cathode.

Figure 4.6 shows the cross-sections of the carbon fiber paper, new cathode, and used cathode. In panel a, the disordered carbon fibers are shown to be protruding at the edges and surrounded by a soft matrix. The image shows two sheets of the carbon fiber matrix with a gap in between the layers. The diameter of the carbon fibers was found to be about 6.5 to 6.7 µm. In the image of the new cathode, the air-facing graphite layer appeared to dampen the extrusions of carbon fibers and soft matrix, creating more of a homogeneous surface. No carbon fiber protrusions through the graphite layer were observed. However, the water-facing CB layer appears to not inhibit the disorder as much as the graphite layer achieves. There were no obvious changes in the cross-sectional views between the new and used cathodes.

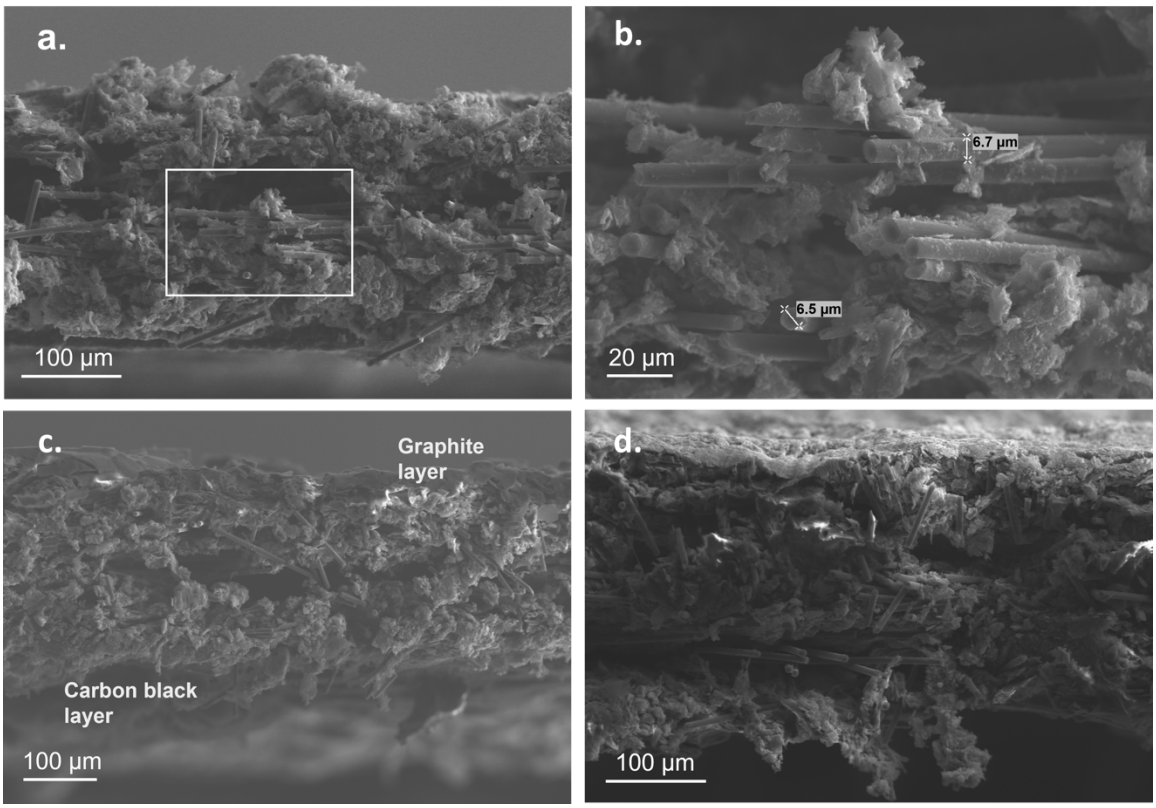


Figure 4.6 Cross-sectional SEM images of a) carbon fiber paper, b) magnified region as indicated by the white boxed region in panel a, c) new cathode, and d) used cathode.

Figure 4.7 offers a closer look at the heterogeneity of the new cathode water-facing CB side. Whereas the SEM image in Figure 4.5b shows mostly a single layer of CB on top, with some intrusion of the slurry into the macroscopic pores of the GDL, it also became apparent that clumping of the CB/PTFE slurry would occur and deposit on top of the existing layer. However, the air-facing graphite side appeared more homogenous. The cross-sectional SEM image above also indicates that the graphite layer creates a smoother surface with less topographical features than the CB layer. Through EDS, it was determined that the CB layer is composed of about 90% C and 10% F. For the graphite layer, the C and F content corresponds to about 70% and 30%, respectively. The SEM and EDS did not show any changes in the air-facing graphite side of the cathode. Throughout the experiment series, the cathodes did not appear to lose water-repellency, and no water leakage (flooding) of the GDL electrodes in the reactor was observed. The hydrophobicity of PTFE, which contributes to the F content, has been shown to be effective in preserving and expelling H_2O_2 from the cathode.[124]

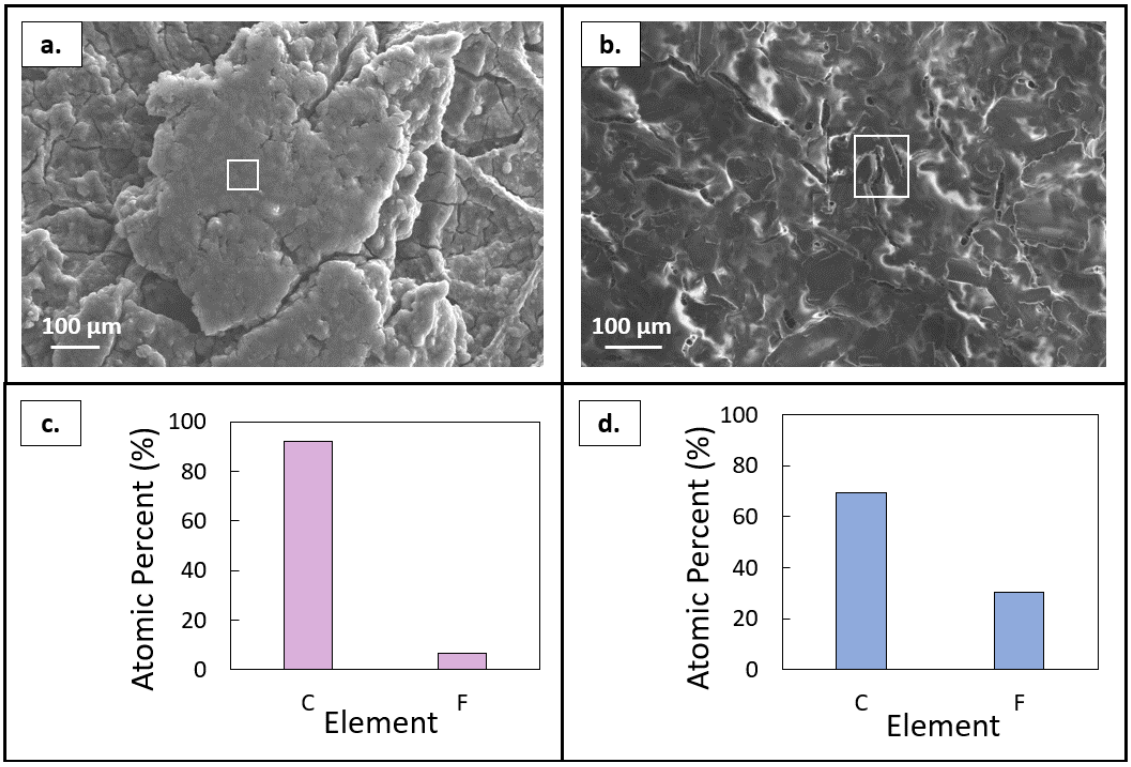


Figure 4.7 SEM images of a) prepared water-facing catalytic side and b) graphite air-facing side, and c) water-facing side and d) air-facing side atomic percent elemental compositions.

Figure 4.8 shows SEM images comparing a new cathode to that of the used cathode, on which the growth of two distinct morphologies was observed. The atomic percentages for panel a refer to the bright and popcorn-like clusters on the surface. The main components of this species were found to be O and Fe, at about 60% and 20%, respectively. The atomic percentages in panel b refer to the species that is not quite as bright and appears to have formed closer to or within the macropores, rather than on the upper most CB layer of the cathode. The main components were also O and Fe, at about 56% and 22%, respectively. Slightly less than 10% of C, Na and Si were

detected for both morphology types. The EDS also indicated that trace amounts of Cl, Mg, P, Ca and S were present.

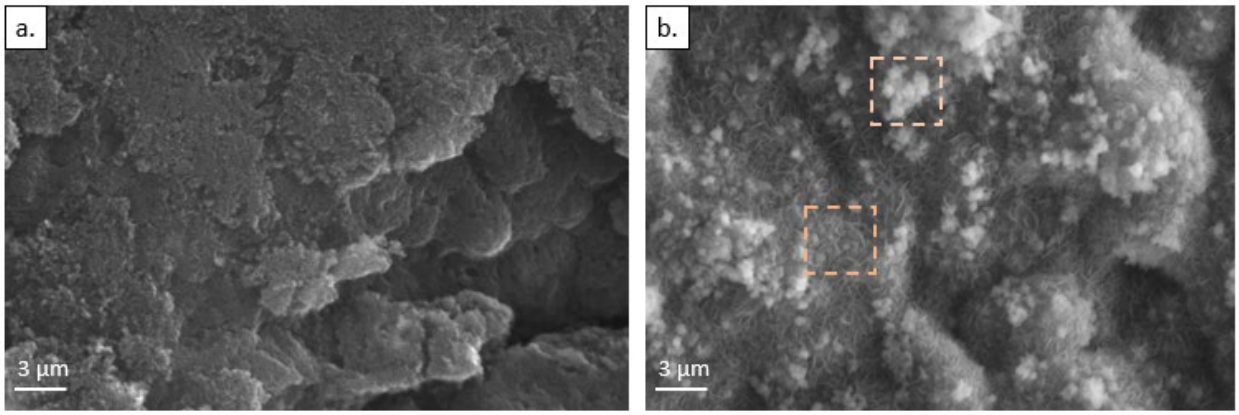


Figure 4.8 SEM images comparing a) new cathode and b) used cathode. The dashed boxes indicate the regions that may contain distinct phases of iron precipitates.

The morphology of the Fe species present in panel a of Figure 4.9 may indicate the presence of Hydrous Ferric Oxides (HFO), which are poorly crystalline Fe-bearing minerals that have been shown to be generated in both conventional Fe-EC and air-EC.[60,66] On the other hand, the lath-shaped species in panel b may be indicative of lepidocrocite, a moderately crystalline mineral that has been found in passive corrosion scales.[145] Lepidocrocite has also been produced in conventional Fe-EC systems,[102] which indicate its potential formation in air-EC, particularly at low CDRs when H_2O_2 production is low (about 30% *FE*). The presence of poorly-conducting Fe minerals, such as lepidocrocite, on the anode in Fe-EC has been found to increase the charge transfer resistance which has the effect of shifting the interface overpotential that may then favor other electrochemical reactions.[144] As such, the decrease in *FE* observed above could be explained by the current being directed to a reaction such as H_2 evolution, instead of H_2O_2 production.[130]

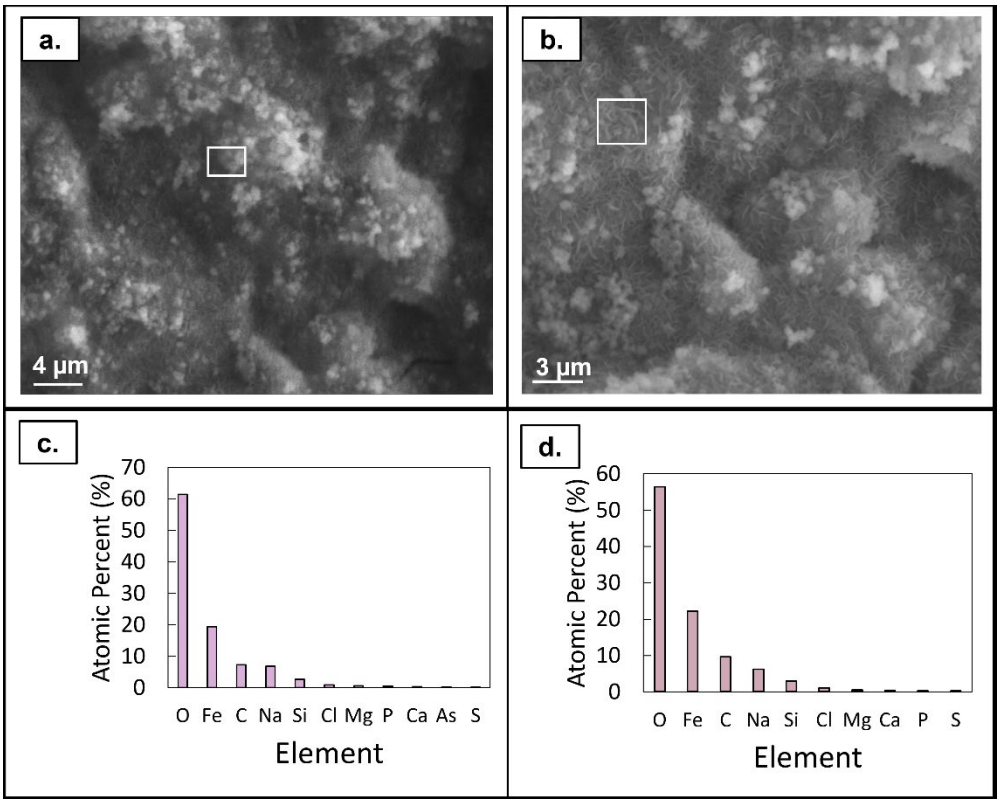


Figure 4.9 SEM and EDS of used cathodes corresponding to a and c) HFO-appearing species, and b and d) lepidocrocite-appearing species.

XRD was used to confirm the presence of crystalline phases on the carbon materials (Figure 4.10). As XRD is a bulk characterization technique, phases found on the surface of the GDL or cathodes were not visible in the diffractograms. The XRD indicates that there is no change in the dominant crystal structures of the bulk material, with three major peaks corresponding to PTFE and graphite across the samples. To identify the presence of iron or salts on the used cathode, additional surface techniques were performed.

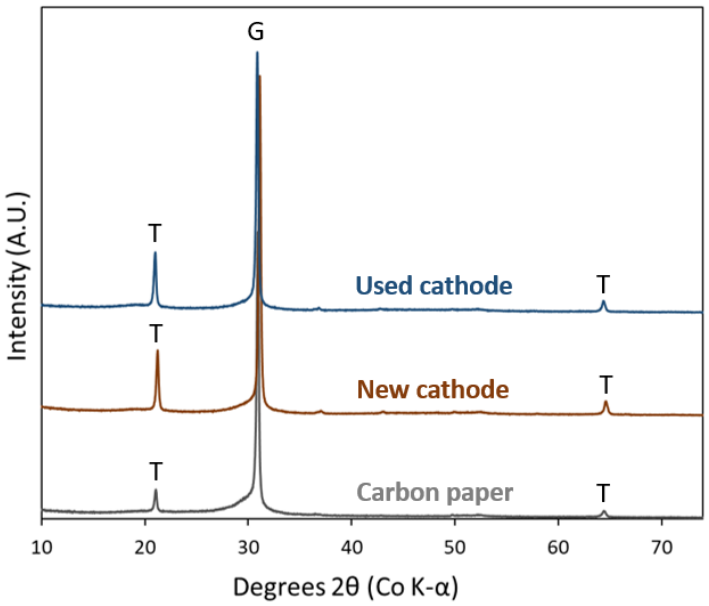


Figure 4.10 XRD of the carbon fiber paper, newly modified cathode, and used cathode. T and G refer to PTFE and graphite, respectively.

4.3.4 Influence of Complex Electrolyte on Precipitate Species

Figure 4.11 shows the regions of the used cathode, and the corresponding sample numbers, that were probed for XFM analysis. The cathode was divided into upper, middle, and lower sections corresponding to regions that may experience greater CO_2 exchange with the atmosphere or greater settling of Fe precipitates. Based on the macroscopic properties within these zones, a total of eight samples were selected to characterize distinct areas (i.e., varying color of deposits, or lack of visible deposits) as 1 cm^2 samples. The μXRF maps for selected samples corresponding to each region are shown below (Figure 4.12 and Figure 4.14).

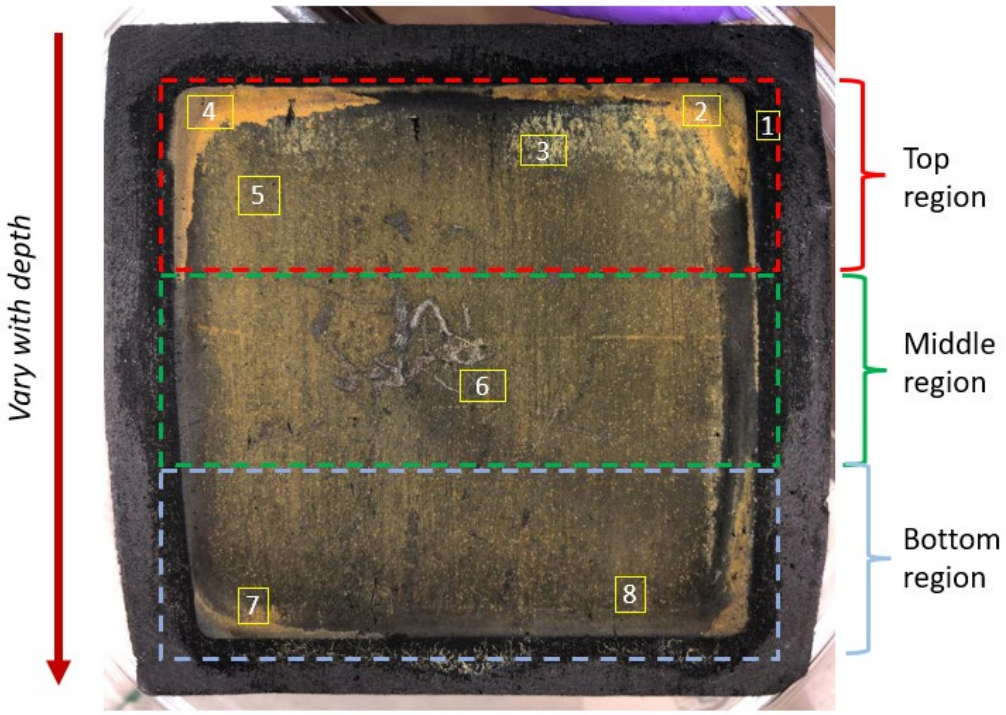


Figure 4.11 The eight sample locations of the used cathode that were probed with μXRF and μXANES spectroscopy. 1 x 1 cm^2 samples were cut as indicated by the numbered spots, each corresponding to either the top, middle, or bottom region of the cathode. The top region was closest to the electrolyte/air interface, as the reactor operated as an open-air batch process.

The μXRF maps for samples 5, 6, and 7 are shown below (Figure 4.12), which all confirm the presence of Fe, Ca, Cl, S, and P. The elemental maps appear to share similarities across the three distinct regions on the cathode. The high intensity regions of Fe tended to overlap with the Cl intensities. To a lesser degree, which can be attributed to the detector and the lighter molecular weight elements, S and P also follow similar intensities coinciding with Fe and Cl on the maps. On the other hand, the Ca maps were characterized by high intensity pinpoints, rather than the more diffuse regions found in Fe and Cl maps. The Ca maps also exhibited light diffuse regions, but the other elemental maps lack the highly concentrated points that characterize the Ca maps. Additional μXRF maps for samples 2 and 3 are shown in Figure 4.14. The μXANES of these features (Figure 4.13) share the similar line shape as the near edge structure of calcite. The XANES spectrum for calcite is characterized by two near edge peaks at 4052 and 4064 eV, lacking a sharp white line (as typical of As K-edge XANES) at the edge energy.[146] However, the μXANES spots on the more diffuse regions share greater similarities with the features of gypsum ($CaSO_4 \cdot 2(H_2O)$) XANES spectra.[147]

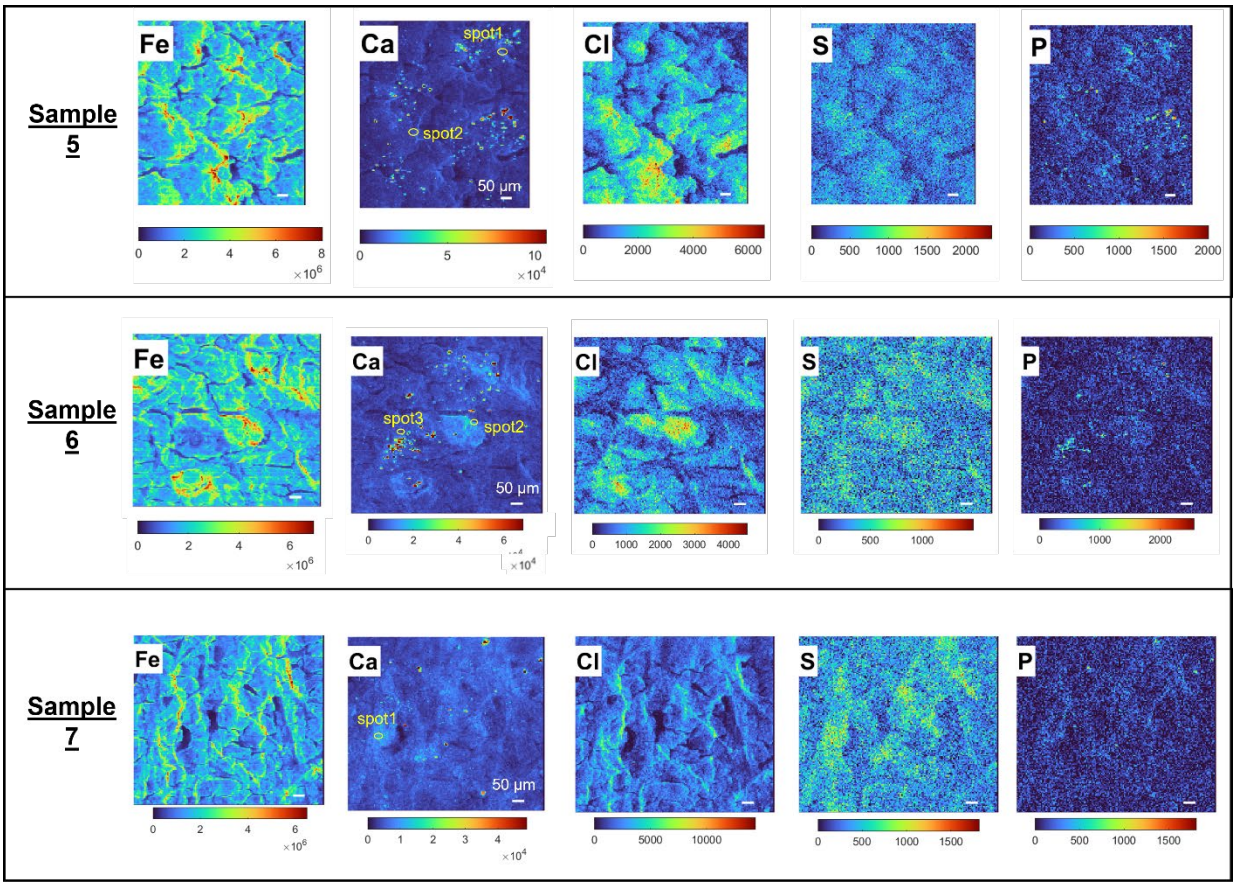


Figure 4.12 µXRF maps of samples 5, 6, and 7. The Fe map was scanned at 100 eV above the Fe K-edge. Other maps were acquired at 100 eV above the Ca K-edge. The spot labels on the Ca map indicate the points that were selected for Ca K-edge µXANES. The scale bars are 50 µm.

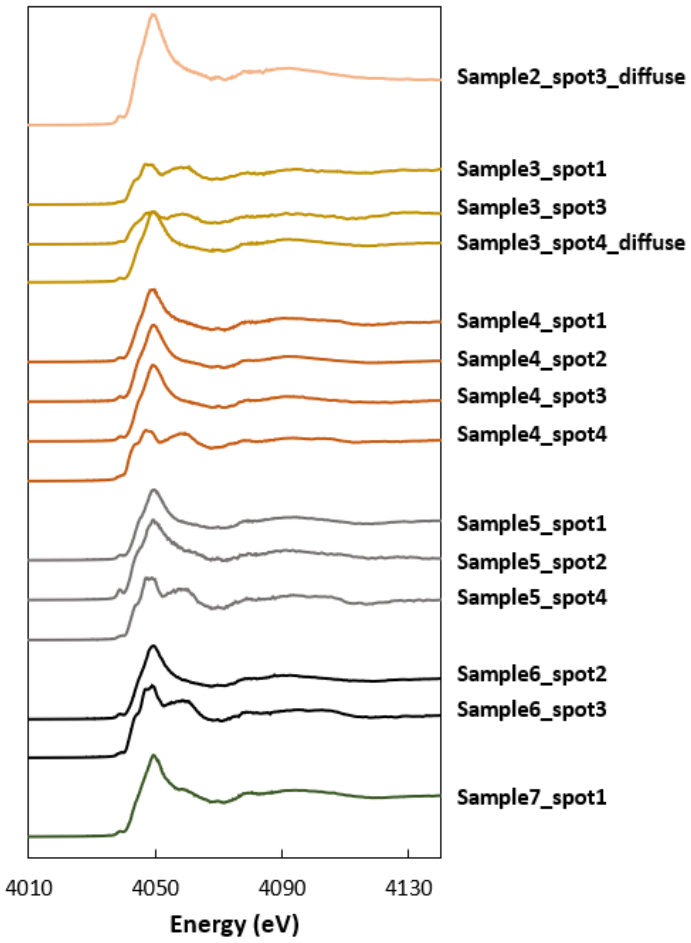


Figure 4.13 Ca K-edge μXANES on selected spots of μXRF maps.

The phenomenon of salt precipitation on the water-facing side of the air cathode can be explained by the electric field driving force that induces transfer of ion salts,[148] as well as the localized alkaline environment from the cathodic reactions.[134] The electric field induced salt precipitation could cause both blockage of O_2 and OH^- transport through the porous cathode and routes for active reaction sites, and thus lowering favorable catalytic activity. Evaporation of the electrolyte through the air cathode was not considered as a significant contributor to the presence of salts as the electrode was never exposed to solution for long periods (longer than 100 min) at a time during batch experiments. However, despite the high conductivity of the groundwater (4.57 ± 0.35 mS/cm) and electrolyte (75.93 ± 1.45 mS/cm) used in the experiment series, the Fe(III) precipitates were found in greater amounts on the cathode than the Ca or Na salts.

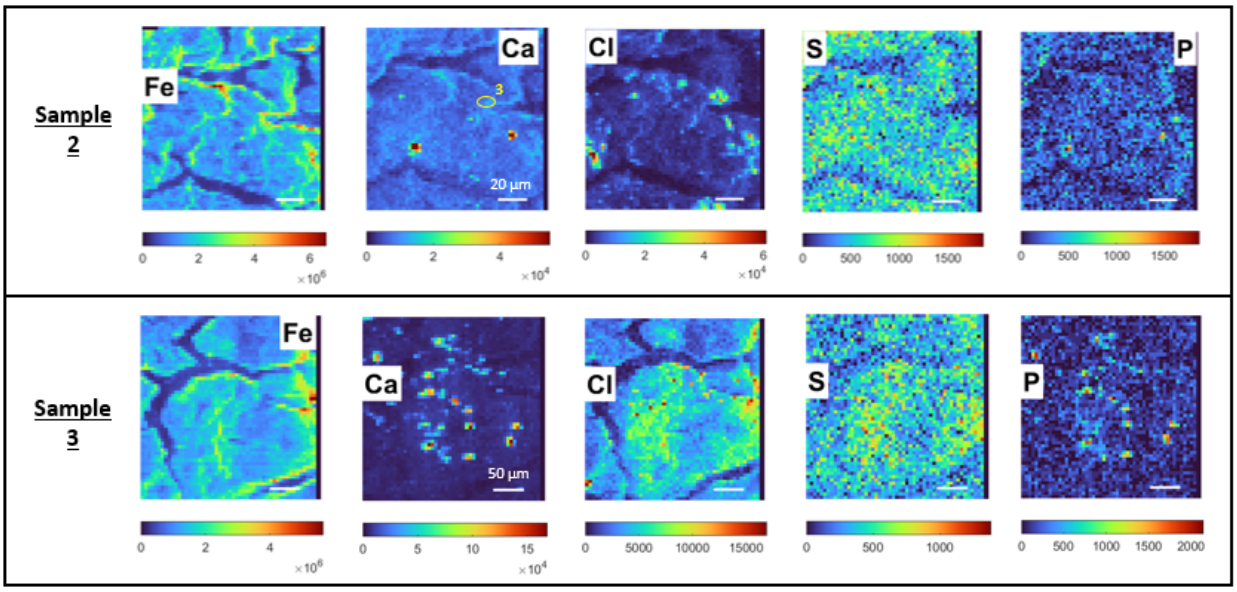


Figure 4.14 µXRF maps of samples 2 and 3. The Fe map was scanned at 100 eV above the Fe K-edge. Other maps were acquired at 100 eV above the Ca K-edge. The spot label on the Ca map indicates the point selected for Ca K-edge µXANES. The scale bars are 20 µm (sample 2) and 50 µm (sample 3).

4.3.5 Effect of Air-EC Operating Conditions on ORR Catalytic Sites

Raman spectroscopy was used to quantify lattice defect densities. Specifically, the D and G modes in a Raman spectrum correspond to disordered carbon and sp^2 hybridized carbon, respectively.[149] The Raman D band is established once point-like defects are introduced into the planar sp^2 carbon lattice.[150] Comparing the relative intensity of the D to the G mode serves as an area defect density metric, allowing for the monitoring of chemical functionalization. A high D to G ratio reflects more structural disorder and a higher degree of defects in the material. The D and G modes lie within 1200 and 1400 cm^{-1}, and between 1560 and 1640 cm^{-1}, respectively. As seen in Figure 4.15, the D and G peaks for the carbon fiber paper, new- and used cathodes fall within these specified ranges.

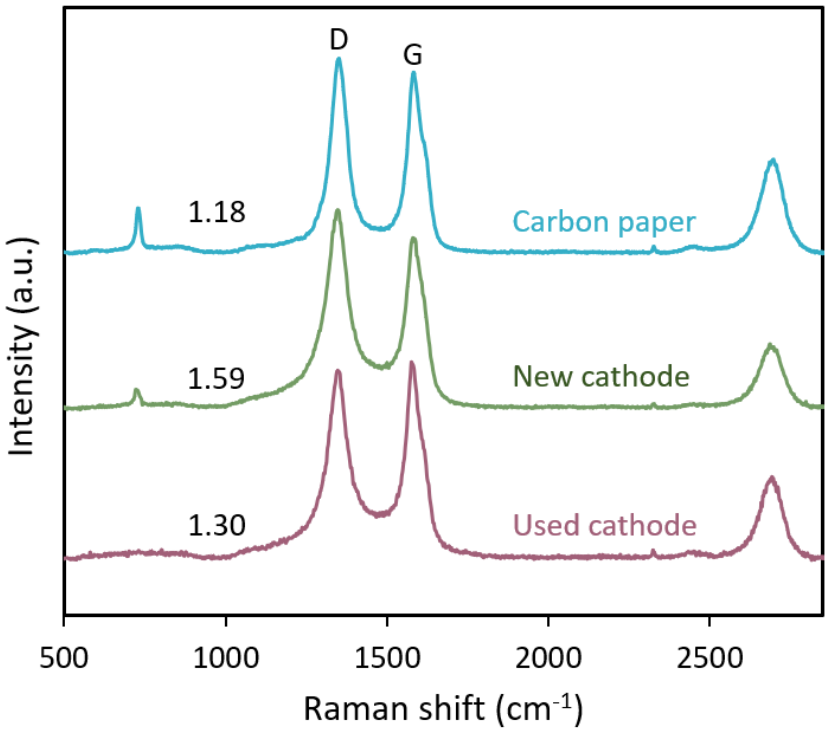


Figure 4.15 Raman spectra of representative samples of carbon fiber paper, newly modified cathode, and used cathode.

The D peaks were located at 1352, 1349, and 1346 cm^{-1} for carbon paper, new cathode, and used cathode, respectively. The G peaks were located at 1582, 1583, and 1576 cm^{-1} for carbon paper, new cathode, and used cathode, respectively. The carbon fiber paper used as the foundational GDE was determined to have an I_D/I_G ratio of 1.18. After the application of CB and PTFE, and subsequent sintering at high temperature (350 ºC), the I_D/I_G value increased to 1.59. After cathode use exposed to a synthetic groundwater matrix containing SO_4^{2-}, PO_4^{3-}, SiO_4^{4-}, Ca^{2+}, Mg^{2+}, Fe^{2+} dissolved ions, and after 6190 Coulombs passed through the cathodic active area (64 cm^2), the I_D/I_G ratio lowered to 1.30. The higher I_D/I_G ratio after modifying the base GDL carbon paper suggests the fabrication method employed is effective in increasing the degree of defects, which may play a key role in the high initial *FE* of ~80% for the high CDR conditions (Figure 4.2).

XPS analysis was used to determine the chemical composition of the various states of the carbon materials. Figure 4.16a shows the survey scan, in the range of 0 – 1300 eV, and the C 1s spectra of the as-purchased carbon fiber paper, newly modified cathode with an applied CB layer, and a used cathode (~100 Coulombs/cm^2 at the end of experimental series). The survey spectra of the carbon paper confirmed the presence of C and F elements, and O was additionally identified in the new cathode spectra. The used cathode survey spectra confirmed the presence of Fe, Na, and Si, in addition to C, F and O. Trace amount of Mn and Mg were also identified (Table 4.1).

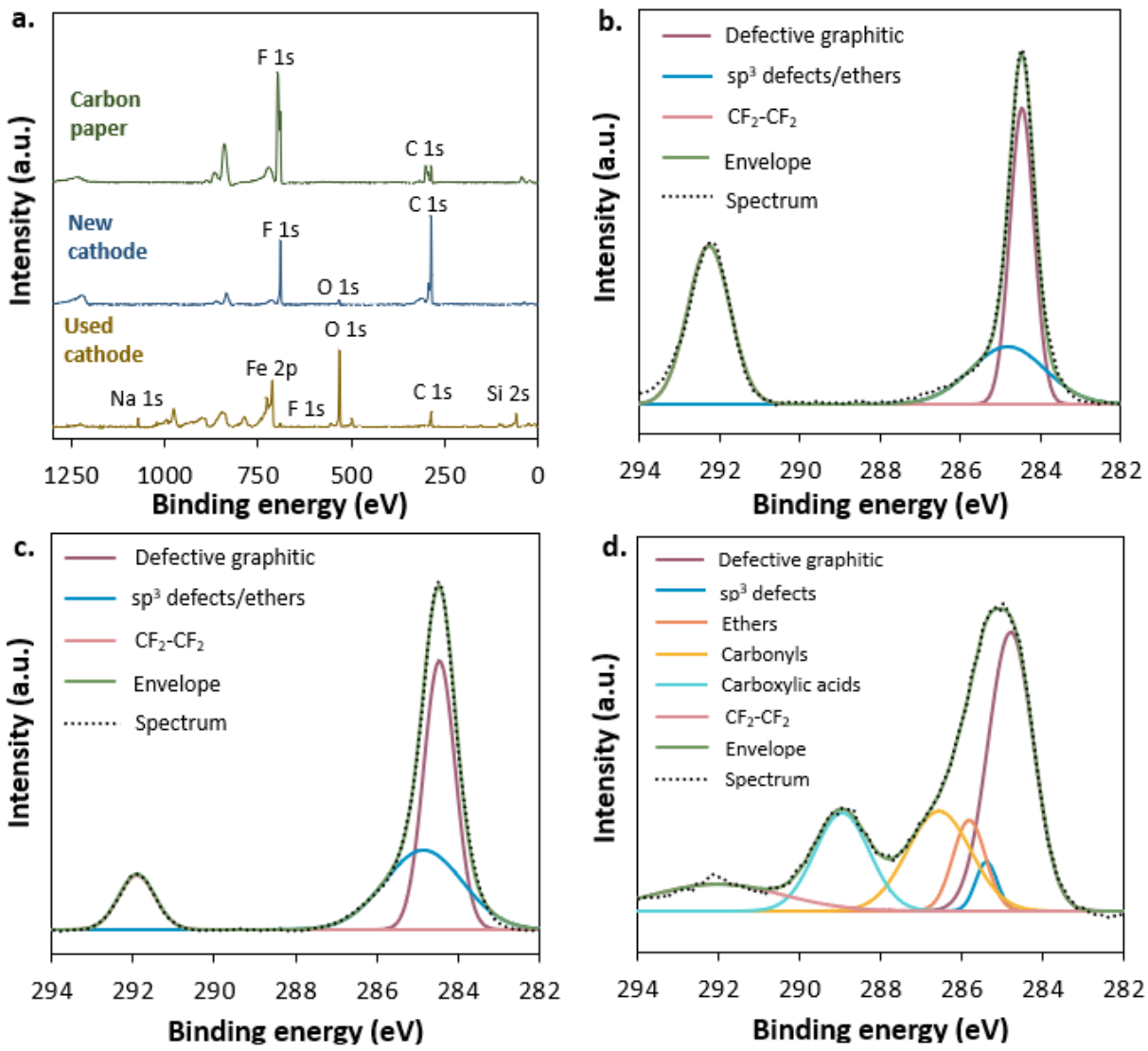


Figure 4.16 XPS spectra of representative samples of carbon fiber paper, newly modified cathode, and used cathode a) survey spectra b) carbon paper, c) new cathode, and d) used cathode C 1s spectrum.

Table 4.1 Atomic % from XPS analysis of used cathode condition.

Atomic %							
C 1s	**F 1s**	**O 1s**	**Si 2p**	**Fe 2p**	**Na 1s**	**Mg 1s**	**Mn 2p3**
27.61 ± 1.17	3.95 ± 1.18	48.65 ± 1.92	3.72 ± 0.27	12.49 ± 0.41	2.45 ± 0.02	0.76 ± 0.02	0.53 ± 0.00

The C 1s spectra (panels c – d), confirm sp^2 bonding in graphitic carbon (purple-colored peak) at around 284.6 eV in all samples analyzed. Modifying the carbon paper increased this component from about 40% to 51%. After use, the sp^2 bonding decreased back down to 40%. The sp^3 surface defects increased from about 24% to 37%, after the modification process. However, these defects only accounted for 3% of the used cathode deconvoluted C 1s peak. The blue peaks in all samples at around 285.1 eV indicate the presence of surface defects. The CF_2 – CF_2 bond was found at 292.1 eV for the carbon fiber paper and used cathode, while being shifted slightly to around 291.8 eV in the new cathode. This PTFE functional group contributes to enhanced hydrophobicity of the cathode.[124] However, it was found that the CF_2 – CF_2 component was about the same at 11% and 12% for new and used cathodes while being around 37% for the carbon paper. The C 1s peak of the used cathode broadened, as compared to the carbon fiber paper and the new cathode, as well as its center shifting from 284.5 eV to 285.1 eV. Deconvoluted peaks at 286.0 eV, 286.9 eV, and 288.9 eV were assigned to ether, carbonyl, and carboxylic acid functional groups, respectively, with ratios of about 9%, 20%, and 17%.

Table 4.2 Results of C 1s deconvolution of all samples.

	Defective graphitic	**sp^3 defects**	**CF_2-CF_2**	**Ethers**	**Carbonyls**	**Carboxylic acids**
Carbon paper	39.52 ± 0.69	23.58 ± 0.77	36.90 ± 0.32			
New cathode	50.55 ± 0.60	37.33 ± 0.62	12.12 ± 0.16			
Used cathode	39.91 ± 5.34	3.36 ± 20.71	10.90 ± 1.07	9.19 ± 39.95	19.87 ± 25.88	16.78 ± 1.95

Previous research has shown the capability of oxygen-containing functional groups on CB to improve H_2O_2 production.[121,151] Figure 4.17 shows the XPS O 1s deconvoluted peaks of new and used cathode spectra. The peaks at 531.2 eV, 533.0 eV, and 534.9 eV were assigned as carbonyl, ether, and chemisorbed O, respectively, for the new cathode spectra. For the used cathode, the peaks at 530.5 eV, 531.8 eV, 533.4 eV, and 535.6 eV were assigned to Fe_2O_3, carbonates, $Fe_2(SO_4)_3$ and chemisorbed O, respectively. As seen in Table 4.2, the initial ether and carbonyl percentages are higher in the new cathode, at about 40% and 27%, respectively. These results indicate that decrease in *FE* also corresponds to the decrease of these surface O acidic moieties, which function as active sites that accelerate electrochemical reactions.[152]

These results suggest that the vast decrease in defects and oxygen containing surface sites in the used cathode contribute to the up to 40% decrease in *FE*. Previous studies have suggested that graphitic surface defects are the active electrocatalytic sites for the $2e^-$ ORR for H_2O_2 production.[152] These results suggest that loss of ORR sites on the cathode surface, rather than mass transfer limitations of O_2 and H_2O_2, contributed to the loss in *FE* after sustained use.

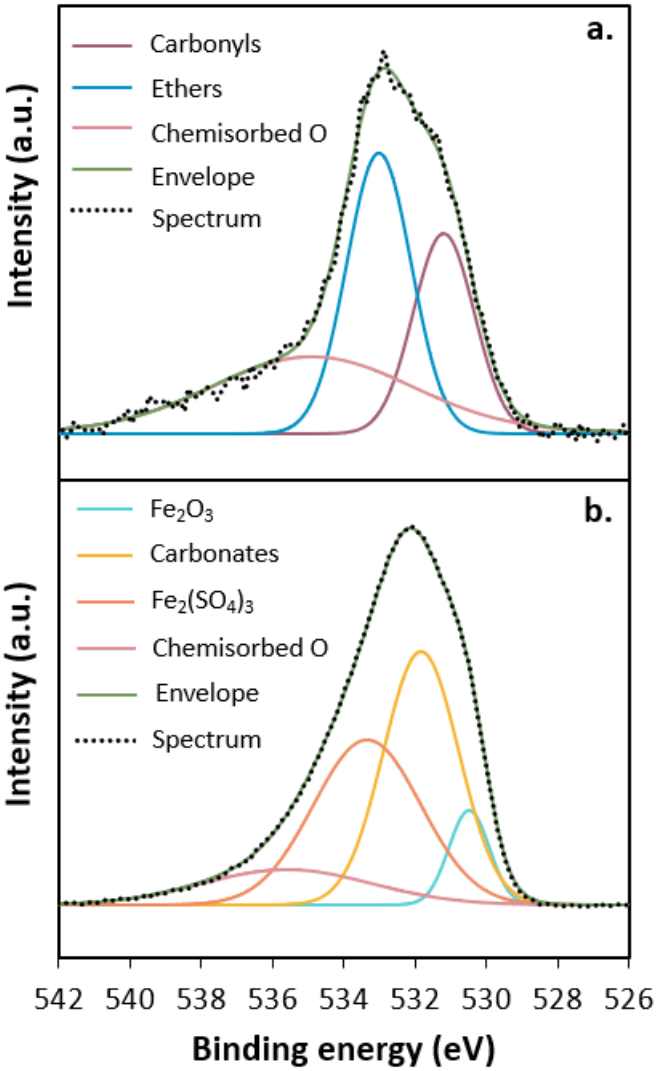


Figure 4.17 XPS O 1s spectrum of a) newly modified cathode and b) used cathode.

Table 4.3 Results of O 1s deconvolution of all samples.

	Concentration (%)					
	Carbonyls	**Ethers**	**Chemisorbed O**	**Fe_2O_3**	**Carbonates**	**$Fe_2(SO_4)_3$**
New cathode	26.75 ± 2.82	39.74 ± 2.61	33.51 ± 2.55	-	-	-
Used cathode	-	-	12.97 ± 9.75	8.24 ± 1.12	40.74 ± 16.49	48.05 ± 24.32

4.3.6 Anode Characterization

Previous work had found high current densities (>2.8 mA/cm^2) to be an effective approach to reducing the formation of a corrosion layer on the anode in conventional Fe-EC, sustaining high *FE* (>90%) for Fe^{2+} production over repeated operating cycles.[133] Mechanistically, this result was explained by the high flux of positively charged Fe^{2+} ions at current densities greater than 2.8 mA/cm^2, coupled with the high positive charge of the anode. These attributes would yield greater diffusion of cations and electrostatic repulsion between the cations and anode. As a result, at high current densities there is greater migration of Fe cations to the bulk solution, as opposed to accumulation of the ions at the electrode surface, typical of low current density systems. The depletion of oxygen near the anode surface was also observed, which prevents Fe^{2+} oxidation and deposition of Fe^{3+} (oxyhydr)oxides onto the electrode.[133]

The carbon steel anode in single-chambered air-EC at current densities much above 2.8 mA/cm^2 is expected to behave in a similar way as previous high current density Fe-EC studies. SEM and vertical scanning interferometry were performed on unused and used carbon-steel plates that served as the anode for experiments in the air-EC system. The original unused carbon steel plate had a thickness of about 5,000 μm. In Figure 4.18 it appears that the high current densities yielded pitting corrosion, with corrosion pits being about 10 μm in depth. The crater depth was calculated based on two cross sections obtained in perpendicular directions, as the difference between the averaged surface level and averaged bottom level of the crater. This characterization was exploratory, and not completed. It was conducted after an experimental series of multiple batch processes. As such, characterization over long duration experiments is required to observe rust formation and *FE* of Fe^{2+} production.

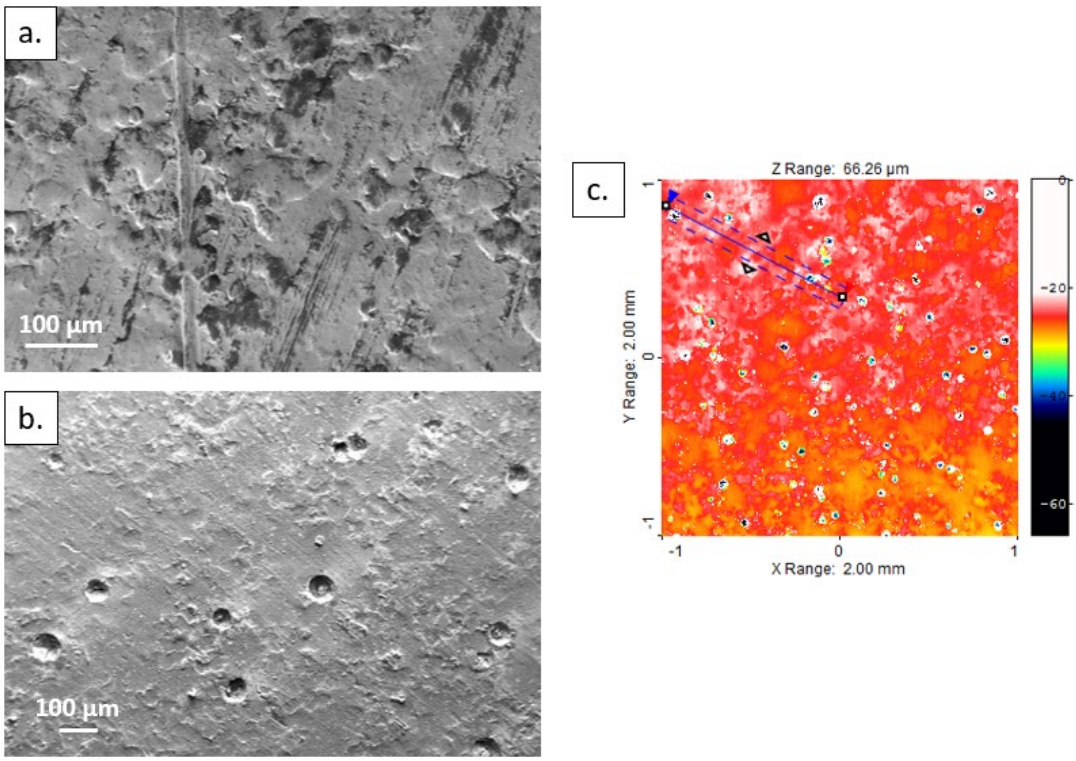


Figure 4.18 SEM of a) unused iron anode and b) iron electrode after use at high dosage rates (50 – 100 C/L/min, 5 – 10 mA/cm^2 or) and c) vertical scanning interferometry of the used anode.

4.3.7 Technical and Environmental Implications

With a decreasing supply of clean water in rural California, low-cost and high-throughput technologies are required to meet future demands for safe drinking water. The H_2O_2 production at the cathode and the Fe^{2+} production at the anode allows for the formation of reactive intermediate species for contaminant oxidation, and uptake on the generated Fe^{3+} solids. Maintaining high cathodic, and anodic, *FE* is thus critical for optimal operation of the air-EC system.

Under current single-chamber configuration of air-EC, Fe and salt precipitation will occur on the cathode after sustained operation, particularly in treating high conductivity groundwater. Although the Fe and salt precipitation on the cathode led to a decrease in *FE*, it may not prove detrimental to contaminant removal efficiency if oxidation or degradation processes are not required. For example, the removal of As(V) is governed by adsorption on the *in-situ* generated adsorbent. Even in low H_2O_2 *FE,* complete oxidation of Fe(II), and subsequent precipitation of Fe(III) (oxyhydr)oxides, can occur given the excess DO being produced in the catholyte.

However, the significant decrease in *FE* after sustained use suggests the need for an optimized mode of operation. To leverage the Fenton chemistry for contaminant removal while increasing the lifespan of the cathode, a two-chamber system can be employed for regular operation using a carbon steel anode, and not only to conduct *FE* tests (for which MMO anode is used). The volumes of these divided cells would then be allowed to mix in a post-electrolysis step.

Moreover, the cathode does not require special storage conditions in between treatments. We observed through multiple experiments that multiple cycles of wetting, and drying in between batch experiments, did not have a negative impact on stability of the cathode. A robust cathodic material, as the one modified in this study, that sustains water repellency and shows no evidence of flooding, is required in the field as to minimize O&M labor and costs. While high ionic strength waters (in some California groundwaters, SO_4^{2-} and Cl^- ion concentrations may be as high as ~1200 mg/L each[153]) promote degradation of the cathode through salt precipitation, low conductivity waters also pose a challenge to air-EC by increasing ohmic resistance. As such, the cathode material must exhibit high charge transfer properties, to prevent high voltage drops and high energy demands.

Chapter 5. Conclusions

The objectives of my dissertation were centered on technology development and deployment for arsenic remediation in resource-constrained communities. In my work I attempted to help fill in the gaps for the process of taking a technology from the lab to the field for positive societal impact. In this way, I navigated the innovation path, as depicted in Chapter 2, starting at a large prototype stage, and then returning to ideation and research. In my doctoral research I had the opportunity to learn about the technology maturation process along different phases, and most importantly, how it does not occur in a vacuum. In this chapter I summarize the main findings from Chapters 2 – 4, discuss the implications of the work presented, and provide areas for future research.

5.1 Strategies for Successful Field Deployment in a Resource-Poor Region: Arsenic Remediation Technology for Drinking Water

5.1.1 Summary of Results

Chapter 2 recounted the lessons learned from the deployment of a scaled up arsenic remediation technology through a participatory and market-based business model. ECAR proved to be a robust and effective technological intervention despite unforeseen technical challenges when evolving from the lab to the field. The 10-year timespan from the beaker-scale ECAR to commissioning of a 10,000 LPD plant shows the persistent efforts required by a multidisciplinary and international team. The data show consistent production of arsenic-safe drinking water over a 10-month period, reducing initial arsenic from ~250 μg/L to ~3 μg/L. The success and acceptance of ECAR relied on key activities, termed Critical Effort Strategies, within the identified 4-year Critical Effort Zone (CEZ) for the piloting phase. Commercializing the pilot plant required the preparation of operation and maintenance manuals, based on the knowledge acquired by field researchers during the CEZ. The industry partner acquired local (State-level and District-level) licenses for permission to establish and operate a plant (an industrial business) that would sell drinking water at less than 1 cent per liter to the surrounding community.

Community outreach during the CEZ included public events hosted by both academic and industrial project members to present on the detrimental health effects of consuming arsenic-contaminated drinking water, explain the ECAR process, and answer questions about the timeline for water distribution. The educational campaign at the school and transparency regarding project milestones and challenges were critical for community trust building. Moreover, the process of knowledge transfer from researchers to the industry partner was a key activity in the CEZ and to ensure the long-term operation of the plant. Finally, based on the commissioning of ECAR through a sustainable business model, several SDGs were addressed in the process, including SDG 6 of safe drinking water, SDG 4 of quality education, and SDG 17 of partnerships for the goals. These efforts resulted in the uptake of ECAR product water by the 3,000 students, teachers and staff at Dhapdhapi High School, and the community, and the plant's long-term technical and financial viability.

5.1.2 Implications of Research and Future Work

Previous literature focused on technology efficacy in the lab until deployment in the field, without discussion of business models or approaches for sustained use as a safe drinking water system. These are defined as being quite distinct from a product or an intervention, with the continued use of the system for greater than five months after ending field research.[154] The ECAR

plant in rural West Bengal meets the criteria as a safe water system, through its continuous operation, maintenance, water distribution, and being financially sustained since field researchers left the site (over six years as of Nov. 2022).

The time within the CEZ allowed for societal readiness towards technology adoption, also described by the concept of "social embedding".[155] However, this signifies that acquiring a safe water system for communities is a multi-year effort (taking 10 years for ECAR from lab-scale to large prototype) with various types of challenges along the way. Project delays can lead to frustration from the community, and urgency towards safe water provision may conflict with the time required for product water quality assurance and entire system readiness. Especially for novel technologies, rigorous testing, sampling, and dissemination of results is critical.

As a most recent outcome from the critical effort strategies, our industry partner replicated the second-ever ECAR plant in Uttar Pradesh, India. This plant delivers 5,000 liters per day of arsenic-safe drinking water. The plant is fully solar-PV powered with roof-top solar panels and has an internal water storage capacity of 15,000 liters to provide for three days of water supply in case of power interruption. Lastly, as a well-managed safe water system, community members were willing to pay for the drinking water produced. In a willingness to pay (WTP) study, conducted by our local academic partners, during the installation of the ECAR pilot plant, 64% of 1003 households surveyed were willing to pay for ECAR-treated safe drinking water.[155]

Conducting a follow-up study at the first ECAR plant location, and at the second plant location, would provide updated information on the number of people in the surrounding community purchasing ECAR water as well as assessing who is still not consuming ECAR water. This allows for a general evaluation of a micro-utility/market-based approach as opposed to an aid/subsidy-based model for arsenic remediation technology deployment in rural India. This post-project survey could also evaluate changes in awareness of the arsenic problem since commercialization of the plant in 2016, and how far beyond the centralized school location the educational efforts reached households. Furthermore, detailed cost assessments for water treatment innovations throughout their scale-up progression would be greatly beneficial to include in publications. While costs of commissioning depend on local water quality and water demand, a fuller transparency of costs from previous sites and multi-year projects may allow for greater adoption of technologies, like ECAR, due to better estimations of benefit-cost ratios for each community.

5.2 Inverse Trends of As(III) and Mn(II) Removal in Air Cathode Assisted Iron Electrocoagulation

5.2.1 Summary of Results

Chapter 3 investigated the effect of charge dosage rate (6, 600 and 1500 C/L/min) and pH (4, 7 and 10) on the combined removal of 1500 µg/L As(III) and 1000 µg/L Mn(II) in air-EC. Decreasing As(III) removal was observed with increasing pH, whereas Mn(II) removal increased with pH. CDR had a modest effect at pH 7, with increasing CDR decreasing As removal, but increasing Mn removal. The EPA-MCL for As was achieved at pH 4 and 7, but only at pH 10 for Mn. Characterization by XRD indicated the high disorder of the Fe precipitates by the presence of one broad peak at 41º 2θ in all conditions. However, the peak appeared sharper in pH 10 sample, indicating a higher level of crystallinity. This was explained by the lesser degree of oxyanion surface poisoning at pHs above typical point of zero charge (PZC) for Fe(III)(oxyhydr)oxides. The

Fe K-edge X-ray absorption spectroscopy also validated that pH and CDR did not impact the structure of Fe(III) precipitates, which were present as highly disordered Hydrous Ferric Oxide (HFO) and two-line ferrihydrite (2LFh), according to the LCFs. The Fe K-edge shell-by-shell fits did not indicate significant differences in the electrolytically generated precipitates. Solution composition, and pH dependency of solutes and solids (electrostatics), appeared to play a greater role than CDR on the structure of the Fe precipitates.

The XAS data indicated that complete As(III) oxidation was achieved in air-EC, but only about 40% was oxidized in conventional Fe-EC. The As K-edge EXAFS shell-by-shell fits showed that As(V) is bound through binuclear corner sharing complexes on the Fe(III) precipitates. Despite the highly oxidizing conditions in air-EC, Mn(II) was not as effectively oxidized as As(III), and was present mostly as Mn(II) (~60%), with some Mn(III) (~40%). In Fe-EC about 30% of Mn(II) was oxidized to Mn(III). The difference in Mn(II) and As(III) removal in air-EC was explained by the selectivity and reaction rates of the Fenton-type reactive intermediates as well as pH dependent Fe(III) surface charge. The effective oxidation of As(III) at all CDRs signifies great amenability to the operating mode of air-EC in the field. Overall, our results indicate that air-EC can be an effective method for both As and Mn remediation, but the pH range for optimal co-removal is limited to circumneutral waters.

5.2.2 Implications of Research and Future Work

As groundwaters contain a wide range of co-occurring contaminant concentrations, the optimal operating conditions of air-EC for As and Mn removal will vary accordingly.[156] Moreover, the co-oxidation of As(III) and Mn(II) with Fe(II) have also been shown to rely on their respective molar ratios.[157] It was observed that at a low As(III)/Fe molar ratio in air-EC yielded effective As(III) oxidation. However, high As(III)/Fe ratios could potentially result in As(III) adsorption to the solids. Adjusting the Mn(II)/Fe ratios for more effective oxidation to Mn(III) or Mn(IV) could benefit removal, or increase the competition for reactive oxidant species.[157] Therefore, future work can focus on characterizing the solids generated at As(III)/Fe and Mn(II)/Fe in low to high molar ratios (e.g., 0.006 to 0.1), providing a greater understanding on the reaction pathways under multiple dosing conditions.

Furthermore, developing a computational model for air-EC, based on previous Fe-EC chemical dynamic models[57,82], would provide minimum iron dose requirements based on CDR, pH, and co-occurring ions. The model should incorporate the oxygen reduction reaction (ORR) at the cathode, and oxidation and adsorption kinetic parameters for Mn(II), in addition to As(III). Data extracted from batch tests in the lab, and from a recent field test of ACAIE, would improve the model predictions. This work can help in system optimization, particularly for co-removal of contaminants with opposing removal trends.

Finally, the rapid rate of Fe(II) oxidation by H_2O_2 in air-EC yielded highly disordered Fe(III) precipitates. As a scaled-up system, collection of the As- and Mn-laden sludge and subsequent disposal at a landfill will be required. However, the contaminant-bound Fe(III) precipitates may transform into higher crystalline and ordered phases over time and with changes in pH. Previous work has shown that the transformation of metastable Fe(III) precipitates into more crystalline solids, such HFO to goethite,[158] decreases reactive surface area and mobilizes particle-bound species, such as As and Mn.[159,160] More research to track the transformation of electrolytically generated As- and Mn-bearing precipitates will provide practical information for implementing a large prototype of air-EC. As such, aging the solids in both aerobic and anaerobic

conditions at varying pH can mimic the behavior expected within hazardous or non-hazardous waste landfills in the United States.

5.3 Investigating Performance of Modified Gas Diffusion Layer in Air-EC

5.3.1 Summary of Results

Chapter 4 sought to better understand the mechanisms by which H_2O_2 production decreases at the cathode. Faradaic Efficiency (*FE)* was used as a performance metric to indicate efficiency of H_2O_2 production at the modified carbon cathode. It was found that operating at high CDRs (600 and 1500 C/L/min) yielded almost three times higher *FE* than at low CDR (6 C/L/min). The DO increase observed in the anolyte chamber suggested water oxidation occurring on the anode. However, the DO increase at the cathode could be attributed to either the parasitic $4e^-$ ORR or cathodic H_2O_2 decomposition.

The SEM of the GDL, modified cathode, and used cathode showed the interwoven nature of 6.5 – 6.7 μm carbon fibers embedded within a PTFE matrix. The CB slurry added topographical features that showed its heterogeneity on top of the GDL base. The EDS confirmed that the GDL base and the modified cathode was made up of a high percentage of C (70 – 90%), followed by F (10 – 30%) from the PTFE. The EDS also confirmed the high percentage of Fe (20 – 22%) and O (56 – 60%) on the used cathode, suggesting the presence of Fe oxides. Based on the morphology, the precipitates appeared to comprise two distinct species, HFO and lepidocrocite. The synchrotron-based X-ray fluorescence spectromicroscopy confirmed the presence of Ca, Cl, and S on the used cathode, and the influence of salt precipitation on *FE*. The line shape of the Ca K-edge μXANES indicates the presence of calcite in addition to Fe(III) precipitates.

The D and G modes of the Raman spectra were used to obtain I_D/I_G ratios of the carbon fiber paper, newly modified cathode, and used cathode. The ratios increased from 1.18 to 1.59 after modification but decreased to 1.30 after use. These results indicate that the 40% reduction in *FE* was due to a loss of defects in the carbon lattice. Moreover, the XPS survey spectra showed the presence of Mn, Mg, Na, and Si on the surface of the used cathode. The deconvoluted C 1s showed a ~33% decrease in sp^3 defects. The deconvoluted O 1s spectra showed ~30% decrease in ethers, ~7% decrease in carbonyls, and ~21% decrease in chemisorbed O. Thus, the decrease in these catalytic ORR sites contributed to the lower *FE* for H_2O_2 production.

5.3.2 Implications of Research and Future Work

Cathode designs with favorable ORR yields have been attributed to high ionic conductivity and hydrophobic yet pervious features.[124] Optimal cathode fabrication must balance the hydrophobicity that prevents flooding with the hydrophilicity of electrochemical active sites for H_2O_2 production. Future work includes systematic testing of novel materials and catalysts to improve ion transfer efficiencies at the water-facing layer while ensuring flooding does not occur over prolonged use.

Although high CDRs improves H_2O_2 production, the higher current applied signifies greater energy requirements. Fabricating cathodes that operate with low steady-state cell voltages, is another important factor to allow for lower energy consumption. Additionally, low conductivity waters cause greater ohmic resistance, which may be overcome by decreasing interelectrode spacing. However, a more robust approach might be to lower the internal resistance of the catalyst material, for high CDRs to be achieved while minimizing energy consumption. Electrochemical

tests, such as electrochemical impedance spectroscopy (EIS), can inform the increase or decrease in internal resistance of distinctly modified GDLs.

Furthermore, operating air-EC as a two-chamber system separated by an AEM prevented H_2O_2 decomposition on the anode. As such, a future study may replace the MMO used in *FE* tests with an iron plate, adding an immediate post-electrolysis mixing step where the oxidation and adsorption processes occur. This design does not add much system complexity while potentially increasing the lifespan of the cathode by preventing the deposition of Fe precipitates. The impact on the carbon defects of the cathode also remains to be investigated. In the absence of Fe, the influence of Ca^{2+}, Na^{2+}, Mg^{2+} salts and NOM might become more apparent on ORR catalytic sites.

Lastly, a better understanding of the impact of fluid dynamics in a continuous flow system on cathode fouling (and anode corrosion/surface layer formation) is still needed, especially for its applicability to scaled-up air-EC in the field. The design of air-EC using computational fluid dynamics (CFD) can provide a robust model considering mass transport and key electrochemical reactions at the electrode boundary layers.

References

(1) Minatel, B. C.; Sage, A. P.; Anderson, C.; Hubaux, R.; Marshall, E. A.; Lam, W. L.; Martinez, V. D. Environmental Arsenic Exposure: From Genetic Susceptibility to Pathogenesis. *Environ. Int.* **2018**, *112*, 183–197. https://doi.org/10.1016/j.envint.2017.12.017.

(2) Podgorski, J.; Berg, M. Global Threat of Arsenic in Groundwater. *Science* **2020**, *368* (6493), 845–850. https://doi.org/10.1126/science.aba1510.

(3) Naujokas, M. F.; Anderson, B.; Ahsan, H.; Aposhian, H. V.; Graziano, J. H.; Thompson, C.; Suk, W. A. The Broad Scope of Health Effects from Chronic Arsenic Exposure: Update on a Worldwide Public Health Problem. *Environ. Health Perspect.* **2013**, *121* (3), 295–302. https://doi.org/10.1289/ehp.1205875.

(4) *Guidelines for Drinking-Water Quality*, 4th ed.; World Health Organization, Ed.; World Health Organization: Geneva, 2011.

(5) Smith, A. H.; Steinmaus, C. M. Health Effects of Arsenic and Chromium in Drinking Water: Recent Human Findings. *Annu. Rev. Public Health* **2009**, *30* (1), 107–122. https://doi.org/10.1146/annurev.publhealth.031308.100143.

(6) I. A. Katsoyiannis; A. I. Zouboulis. Comparative Evaluation of Conventional and Alternative Methods for the Removal of Arsenic from Contaminated Groundwaters. *Rev. Environ. Health* **2006**, *21* (1), 25–42. https://doi.org/10.1515/REVEH.2006.21.1.25.

(7) Zakhar, R.; Derco, J.; Čacho, F. An Overview of Main Arsenic Removal Technologies. *Acta Chim. Slovaca* **2018**, *11* (2), 107–113. https://doi.org/10.2478/acs-2018-0016.

(8) Ahmad, S. A.; Sayed, M. H.; Barua, S.; Khan, M. H.; Faruquee, M. H.; Jalil, A.; Hadi, S. A.; Talukder, H. K. Arsenic in Drinking Water and Pregnancy Outcomes. *Environ. Health Perspect.* **2001**, *109* (6), 629–631. https://doi.org/10.1289/ehp.01109629.

(9) Liu, S.; Guo, X.; Wu, B.; Yu, H.; Zhang, X.; Li, M. Arsenic Induces Diabetic Effects through Beta-Cell Dysfunction and Increased Gluconeogenesis in Mice. *Sci. Rep.* **2014**, *4* (1), 6894. https://doi.org/10.1038/srep06894.

(10) Yu, H.-S.; Lee, C.-H.; Chen, G.-S. Peripheral Vascular Diseases Resulting from Chronic Arsenical Poisoning. *J. Dermatol.* **2002**, *29* (3), 123–130. https://doi.org/10.1111/j.1346-8138.2002.tb00234.x.

(11) Treatment Technologies for Arsenic Removal. United Stated Environmental Protection Agency, 2005. https://nepis.epa.gov/Exe/ZyPDF.cgi/20017IDW.PDF?Dockey=20017IDW.PDF (accessed 2022-03-31).

(12) Martinez, V. D.; Vucic, E. A.; Becker-Santos, D. D.; Gil, L.; Lam, W. L. Arsenic Exposure and the Induction of Human Cancers. *J. Toxicol.* **2011**, *2011*, 431287. https://doi.org/10.1155/2011/431287.

(13) National Research Council. *Arsenic in Drinking Water: 2001 Update*; The National Academies Press: Washington, DC, 2001. https://doi.org/10.17226/10194 (accessed 2020-08-11).

(14) Smedley, P. L.; Kinniburgh, D. G. Arsenic in Groundwater and the Environment. In *Essentials of Medical Geology: Revised Edition*; Selinus, O., Ed.; Springer Netherlands: Dordrecht, 2013; pp 279–310. https://doi.org/10.1007/978-94-007-4375-5_12.

(15) *U.S. EPA. 2018 Edition of the Drinking Water Standards and Health Advisories Tables.*; 2018. https://www.epa.gov/sites/production/files/2018-03/documents/dwtable2018.pdf. (accessed 2018-10-18).
(16) *U.S. EPA. IRIS Toxicological Review of Inorganic Arsenic*; 2010. https://cfpub.epa.gov/ncea/iris_drafts/recordisplay.cfm?deid=219111 (accessed 2018-10-18).
(17) Smith, A. H.; Lopipero, P. A.; Bates, M. N.; Steinmaus, C. M. Arsenic Epidemiology and Drinking Water Standards. *Science* **2002**, *296* (5576), 2145–2146. https://doi.org/10.1126/science.1072896.
(18) Fisher, A. T.; López-Carrillo, L.; Gamboa-Loira, B.; Cebrián, M. E. Standards for Arsenic in Drinking Water: Implications for Policy in Mexico. *J. Public Health Policy* **2017**, *38* (4), 395–406. https://doi.org/10.1057/s41271-017-0087-7.
(19) *Arsenic in Drinking Water | California State Water Quality Control Board*. https://www.waterboards.ca.gov/drinking_water/certlic/drinkingwater/Arsenic.html (accessed 2022-06-20).
(20) Ahmad, A.; van der Wens, P.; Baken, K.; de Waal, L.; Bhattacharya, P.; Stuyfzand, P. Arsenic Reduction to <1 µg/L in Dutch Drinking Water. *Environ. Int.* **2020**, *134*, 105253. https://doi.org/10.1016/j.envint.2019.105253.
(21) Jameel, Y.; Mozumder, M. R. H.; van Geen, A.; Harvey, C. F. Well-Switching to Reduce Arsenic Exposure in Bangladesh: Making the Most of Inaccurate Field Kit Measurements. *GeoHealth* **2021**, *5* (12), e2021GH000464. https://doi.org/10.1029/2021GH000464.
(22) Indian Standard Drinking Water - Specification (Second Revision) IS 10500 : 2012, 2012.
(23) Amrose, S.; Gadgil, A.; Srinivasan, V.; Kowolik, K.; Muller, M.; Huang, J.; Kostecki, R. Arsenic Removal from Groundwater Using Iron Electrocoagulation: Effect of Charge Dosage Rate. *J. Environ. Sci. Health Part A* **2013**, *48* (9), 1019–1030. https://doi.org/10.1080/10934529.2013.773215.
(24) Ahmad, S. A.; Khan, M. H.; Haque, M. Arsenic Contamination in Groundwater in Bangladesh: Implications and Challenges for Healthcare Policy. *Risk Manag. Healthc. Policy* **2018**, *11*, 251–261. https://doi.org/10.2147/RMHP.S153188.
(25) Ghosh, N.; Singh, R. Groundwater Arsenic Contamination in India: Vulnerability and Scope for Remedy. **2009**.
(26) Flanagan, S. V.; Johnston, R. B.; Zheng, Y. Arsenic in Tube Well Water in Bangladesh: Health and Economic Impacts and Implications for Arsenic Mitigation. *Bull. World Health Organ.* **2012**, *90*, 839–846. https://doi.org/10.2471/BLT.11.101253.
(27) Das, A.; Roy, J.; Chakraborti, S. *Socio-Economic Analysis of Arsenic Contamination of Groundwater in West Bengal*; Springer, 2016.
(28) Das, A.; Roy, J. Socio-Economic Fallout of Arsenicosis in West Bengal: A Case Study in Murshidabad District. *J Indian Soc Agric Stat* **2013**, *67*, 267–278.
(29) Ayotte, J. D.; Nolan, B. T.; Gronberg, J. A. Predicting Arsenic in Drinking Water Wells of the Central Valley, California. *Environ. Sci. Technol.* **2016**, *50* (14), 7555–7563. https://doi.org/10.1021/acs.est.6b01914.
(30) Pelton, T.; Bernhardt, C.; Schaeffer, E. *Arsenic in California Drinking Water*; Environmental Integrity Project, 2016.
(31) Balazs, C. L.; Morello-Frosch, R.; Hubbard, A. E.; Ray, I. Environmental Justice Implications of Arsenic Contamination in California's San Joaquin Valley: A Cross-Sectional, Cluster-Design Examining Exposure and Compliance in Community Drinking

Water Systems. *Environ. Health* **2012**, *11* (1), 84. https://doi.org/10.1186/1476-069X-11-84.
(32) Hering, J. G.; Katsoyiannis, I. A.; Theoduloz, G. A.; Berg, M. Arsenic Removal from Drinking Water: Experiences with Technologies and Constraints in Practice. *J. Environ. Eng.* **2017**, *143* (5), 03117002.
(33) *Arsenic Rule Could Cost Utilities Billions*. WaterWorld. https://www.waterworld.com/drinking-water/potable-water-quality/article/16191503/arsenic-rule-could-cost-utilities-billions (accessed 2022-10-12).
(34) Vu, K. B.; Kaminski, M. D.; Nunez, L. *Review of Arsenic Removal Technologies for Contaminated Groundwaters.*; United States, 2003. https://doi.org/10.2172/815660.
(35) *Definition: public water system from 42 USC § 300f(4)(A) | LII / Legal Information Institute*. https://www.law.cornell.edu/uscode/text/42/300f#4_A (accessed 2022-11-03).
(36) Hanak, E.; Mount, J. *Water Use in California*. Public Policy Institute of California. https://www.ppic.org/publication/water-use-in-california/ (accessed 2020-07-15).
(37) Balazs, C. L.; Ray, I. The Drinking Water Disparities Framework: On the Origins and Persistence of Inequities in Exposure. *Am. J. Public Health* **2014**, *104* (4), 603–611. https://doi.org/10.2105/AJPH.2013.301664.
(38) *Arsenic Treatment Technology Evaluation Handbook for Small Systems*; EPA 816-R-03-014.; USEPA: Office of Water, Washington, DC, 2003.
(39) Höll, W. H. Mechanisms of Arsenic Removal from Water. *Environ. Geochem. Health* **2010**, *32* (4), 287–290. https://doi.org/10.1007/s10653-010-9307-9.
(40) O'Day, P. A. Chemistry and Mineralogy of Arsenic. *Elements* **2006**, *2* (2), 77–83. https://doi.org/10.2113/gselements.2.2.77.
(41) Ng, K.-S.; Ujang, Z.; Le-Clech, P. Arsenic Removal Technologies for Drinking Water Treatment. *Rev. Environ. Sci. Biotechnol.* **2004**, *3* (1), 43–53. https://doi.org/10.1023/B:RESB.0000040054.28151.84.
(42) Nicomel, N. R.; Leus, K.; Folens, K.; Van Der Voort, P.; Du Laing, G. Technologies for Arsenic Removal from Water: Current Status and Future Perspectives. *Int. J. Environ. Res. Public. Health* **2016**, *13* (1), 62. https://doi.org/10.3390/ijerph13010062.
(43) Bondu, R.; Cloutier, V.; Rosa, E.; Benzaazoua, M. A Review and Evaluation of the Impacts of Climate Change on Geogenic Arsenic in Groundwater from Fractured Bedrock Aquifers. *Water. Air. Soil Pollut.* **2016**, *227* (9), 296. https://doi.org/10.1007/s11270-016-2936-6.
(44) Ahmad, A. Arsenic Removal by Iron Based Co-Precipitation : Mechanisms in Groundwater Treatment, Wageningen University, 2020. https://doi.org/10.18174/519635.
(45) Holl, W. H. Mechanisms of Arsenic Removal from Water. *Environ. Geochem. Health* **2010**, *32* (4), 287–290. https://doi.org/10.1007/s10653-010-9307-9.
(46) Siddique, T. A.; Dutta, N. K.; Roy Choudhury, N. Nanofiltration for Arsenic Removal: Challenges, Recent Developments, and Perspectives. *Nanomaterials* **2020**, *10* (7), 1323. https://doi.org/10.3390/nano10071323.
(47) *UN General Assembly. Transforming Our World: The 2030 Agenda for Sustainable Development*; 2015. https://sustainabledevelopment.un.org/content/documents/21252030%20Agenda%20for%20Sustainable%20Development%20web.pdf (accessed 2019-06-18).
(48) Hering, J. G.; Maag, S.; Schnoor, J. L. A Call for Synthesis of Water Research to Achieve the Sustainable Development Goals by 2030. *Environ. Sci. Technol.* **2016**, *50* (12), 6122–6123. https://doi.org/10.1021/acs.est.6b02598.

(49) Song, P.; Yang, Z.; Zeng, G.; Yang, X.; Xu, H.; Wang, L.; Xu, R.; Xiong, W.; Ahmad, K. Electrocoagulation Treatment of Arsenic in Wastewaters: A Comprehensive Review. *Chem. Eng. J.* **2017**, *317*, 707–725. https://doi.org/10.1016/j.cej.2017.02.086.
(50) Nidheesh, P.; Singh, T. A. Arsenic Removal by Electrocoagulation Process: Recent Trends and Removal Mechanism. *Chemosphere* **2017**, *181*, 418–432. https://doi.org/10.1016/j.chemosphere.2017.04.082.
(51) Raven, K. P.; Jain, A.; Loeppert, R. H. Arsenite and Arsenate Adsorption on Ferrihydrite: Kinetics, Equilibrium, and Adsorption Envelopes. *Environ. Sci. Technol.* **1998**, *32* (3), 344–349. https://doi.org/10.1021/es970421p.
(52) Roberts, L. C.; Hug, S. J.; Ruettimann, T.; Billah, M. M.; Khan, A. W.; Rahman, M. T. Arsenic Removal with Iron(II) and Iron(III) in Waters with High Silicate and Phosphate Concentrations. *Environ. Sci. Technol.* **2004**, *38* (1), 307–315. https://doi.org/10.1021/es0343205.
(53) Waychunas, G. A.; Rea, B. A.; Fuller, C. C.; Davis, J. A. Surface Chemistry of Ferrihydrite: Part 1. EXAFS Studies of the Geometry of Coprecipitated and Adsorbed Arsenate. *Geochim. Cosmochim. Acta* **1993**, *57* (10), 2251–2269. https://doi.org/10.1016/0016-7037(93)90567-G.
(54) van Genuchten, C. M.; Pena, J.; Amrose, S. E.; Gadgil, A. J. Structure of Fe (III) Precipitates Generated by the Electrolytic Dissolution of Fe (0) in the Presence of Groundwater Ions. *Geochim. Cosmochim. Acta* **2014**, *127*, 285–304.
(55) Elless, M. P.; Poynton, C. Y.; Willms, C. A.; Doyle, M. P.; Lopez, A. C.; Sokkary, D. A.; Ferguson, B. W.; Blaylock, M. J. Pilot-Scale Demonstration of Phytofiltration for Treatment of Arsenic in New Mexico Drinking Water. *Water Res.* **2005**, *39* (16), 3863–3872. https://doi.org/10.1016/j.watres.2005.07.029.
(56) Gadgil, A. J.; Addy, S. E.; Kostecki, R. Electrochemical Removal of Arsenic. **2011**.
(57) Li, L.; van Genuchten, C. M.; Addy, S. E.; Yao, J.; Gao, N.; Gadgil, A. J. Modeling As (III) Oxidation and Removal with Iron Electrocoagulation in Groundwater. *Environ. Sci. Technol.* **2012**, *46* (21), 12038–12045. https://doi.org/10.1021/es302456b.
(58) van Genuchten, C. M.; Addy, S. E.; Peña, J.; Gadgil, A. J. Removing Arsenic from Synthetic Groundwater with Iron Electrocoagulation: An Fe and As K-Edge EXAFS Study. *Environ. Sci. Technol.* **2012**, *46* (2), 986–994. https://doi.org/10.1021/es201913a.
(59) Amrose, S. E.; Bandaru, S. R.; Delaire, C.; van Genuchten, C. M.; Dutta, A.; DebSarkar, A.; Orr, C.; Roy, J.; Das, A.; Gadgil, A. J. Electro-Chemical Arsenic Remediation: Field Trials in West Bengal. *Sci. Total Environ.* **2014**, *488*, 539–546. https://doi.org/10.1016/j.scitotenv.2013.11.074.
(60) van Genuchten, C. M.; Peña, J.; Amrose, S. E.; Gadgil, A. J. Structure of Fe (III) Precipitates Generated by the Electrolytic Dissolution of Fe (0) in the Presence of Groundwater Ions. *Geochim. Cosmochim. Acta* **2014**, *127*, 285–304. https://doi.org/10.1016/j.gca.2013.11.044.
(61) Balazs, C.; Faust, J.; Goddard, J.; Bangia, K.; Fons, E.; Starke, M. *A Framework and Tool for Evaluating California's Progress in Achieving the Human Right to Water*; Office of Environmental Health Hazard Assessment, 2019. https://oehha.ca.gov/media/downloads/water/report/hr2wframeworkpublicreviewdraft010319.pdf (accessed 2020-02-01).
(62) Hug, S. J.; Leupin, O. Iron-Catalyzed Oxidation of Arsenic (III) by Oxygen and by Hydrogen Peroxide: PH-Dependent Formation of Oxidants in the Fenton Reaction. *Environ. Sci. Technol.* **2003**, *37* (12), 2734–2742. https://doi.org/10.1021/es026208x.

(63) Si, Y.; Li, G.; Zhang, F. Energy-Efficient Oxidation and Removal of Arsenite from Groundwater Using Air-Cathode Iron Electrocoagulation. *Environ. Sci. Technol. Lett.* **2016**, *4* (2), 71–75. https://doi.org/10.1021/acs.estlett.6b00430.
(64) Barazesh, J. M.; Hennebel, T.; Jasper, J. T.; Sedlak, D. L. Modular Advanced Oxidation Process Enabled by Cathodic Hydrogen Peroxide Production. *Environ. Sci. Technol.* **2015**, *49* (12), 7391–7399. https://doi.org/10.1021/acs.est.5b01254.
(65) King, D. W.; Farlow, R. Role of Carbonate Speciation on the Oxidation of Fe(II) by H2O2. *Mar. Chem.* **2000**, *70* (1), 201–209. https://doi.org/10.1016/S0304-4203(00)00026-8.
(66) Bandaru, S. R.; van Genuchten, C. M.; Kumar, A.; Glade, S.; Hernandez, D.; Nahata, M.; Gadgil, A. Rapid and Efficient Arsenic Removal by Iron Electrocoagulation Enabled with in Situ Generation of Hydrogen Peroxide. *Environ. Sci. Technol.* **2020**, *54* (10), 6094–6103. https://doi.org/10.1021/acs.est.0c00012.
(67) Roy, J. Economic Benefits of Arsenic Removal from Ground Water — A Case Study from West Bengal, India. *Sci. Total Environ.* **2008**, *397* (1–3), 1–12. https://doi.org/10.1016/j.scitotenv.2008.02.007.
(68) Adams, P. In Bangladesh, Funds Dry up for Arsenic Mitigation Research. *The Lancet* **2013**, *382* (9906), 1693–1694. https://doi.org/10.1016/S0140-6736(13)62391-0.
(69) Hoque, B. A.; Hoque, M. M.; Ahmed, T.; Islam, S.; Azad, A. K.; Ali, N.; Hossain, M.; Hossain, M. S. Demand-Based Water Options for Arsenic Mitigation: An Experience from Rural Bangladesh. *Public Health* **2004**, *118* (1), 70–77. https://doi.org/10.1016/S0033-3506(03)00135-5.
(70) Ahmad, J.; Goldar, B. N.; Misra, S.; Jakariya, M. Willingness to Pay for Arsenic-Free, Safe Drinking Water in Bangladesh. *World Bank Water Sanit. Program-South Asia* **2003**.
(71) Etmannski, T. R.; Darton, R. C. A Methodology for the Sustainability Assessment of Arsenic Mitigation Technology for Drinking Water. *Sci. Total Environ.* **2014**, *488–489*, 505–511. https://doi.org/10.1016/j.scitotenv.2013.10.112.
(72) Sarkar, S.; Greenleaf, J. E.; Gupta, A.; Ghosh, D.; Blaney, L. M.; Bandyopadhyay, P.; Biswas, R. K.; Dutta, A. K.; SenGupta, A. K. Evolution of Community-Based Arsenic Removal Systems in Remote Villages in West Bengal, India: Assessment of Decade-Long Operation. *Water Res.* **2010**, *44* (19), 5813–5822. https://doi.org/10.1016/j.watres.2010.07.072.
(73) Griggs, D.; Stafford-Smith, M.; Gaffney, O.; Rockström, J.; Öhman, M. C.; Shyamsundar, P.; Steffen, W.; Glaser, G.; Kanie, N.; Noble, I. Policy: Sustainable Development Goals for People and Planet. *Nature* **2013**, *495*, 305–307. https://doi.org/10.1038/495305a.
(74) Delaire, C.; Amrose, S.; Zhang, M.; Hake, J.; Gadgil, A. How Do Operating Conditions Affect As (III) Removal by Iron Electrocoagulation? *Water Res.* **2017**, *112*, 185–194. https://doi.org/10.1016/j.watres.2017.01.030.
(75) Gadgil, A.; Amrose, S.; Bandaru, S.; Delaire, C.; Torkelson, A.; van Genuchten, C. Addressing Arsenic Mass Poisoning in South Asia with Electrochemical Arsenic Remediation. In *Water Reclamation and Sustainability*; Ahuja, S., Ed.; Elsevier: Boston, 2014; pp 115–154. https://doi.org/10.1016/B978-0-12-411645-0.00006-7.
(76) van Genuchten, C. M.; Bandaru, S. R.; Surorova, E.; Amrose, S. E.; Gadgil, A. J.; Pena, J. Formation of Macroscopic Surface Layers on Fe (0) Electrocoagulation Electrodes during an Extended Field Trial of Arsenic Treatment. *Chemosphere* **2016**, *153*, 270–279. https://doi.org/10.1016/j.chemosphere.2016.03.027.

(77) van Genuchten, C. M.; Gadgil, A. J.; Peña, J. Fe (III) Nucleation in the Presence of Bivalent Cations and Oxyanions Leads to Subnanoscale 7 Å Polymers. *Environ. Sci. Technol.* **2014**, *48* (20), 11828–11836. https://doi.org/10.1021/es503281a.
(78) Cherry, J. A.; Shaikh, A. U.; Tallman, D. E.; Nicholson, R. V. Arsenic Species as an Indicator of Redox Conditions in Groundwater. In *Developments in Water Science*; Back, W., Stephenson, D. A., Eds.; Contemporary Hydrogeology; Elsevier, 1979; Vol. 12, pp 373–392. https://doi.org/10.1016/S0167-5648(09)70027-9.
(79) Smedley, P. L.; Kinniburgh, D. G. A Review of the Source, Behaviour and Distribution of Arsenic in Natural Waters. *Appl. Geochem.* **2002**, *17* (5), 517–568. https://doi.org/10.1016/S0883-2927(02)00018-5.
(80) Bullock, M. *House of Commons - Science and Technology: Written evidence submitted by Matthew Bullock*. United Kingdom Parliament. https://publications.parliament.uk/pa/cm201213/cmselect/cmsctech/348/348we25.htm (accessed 2019-05-09).
(81) Andreesen, M. *Product Market Fit. EE204: Business Management for Electrical Engineers and Computer Scientists.* Stanford University. https://web.stanford.edu/class/ee204/ProductMarketFit.html (accessed 2019-06-18).
(82) Delaire, C.; Das, A.; Amrose, S.; Gadgil, A.; Roy, J.; Ray, I. Determinants of the Use of Alternatives to Arsenic-Contaminated Shallow Groundwater: An Exploratory Study in Rural West Bengal, India. *J. Water Health* **2017**, *15* (5), 799–812. https://doi.org/10.2166/wh.2017.321.
(83) Roy, J.; Chattopadhyay, S.; Mukherjee, S.; Kanjilal, M.; Samajpati, S.; Roy, S. An Economic Analysis of Demand for Water Quality: Case of Kolkata. *Econ. Polit. Wkly.* **2004**, *39* (2), 186–192.
(84) Dreze, J.; Kingdon, G. G. School Participation in Rural India. *Rev. Dev. Econ.* **2001**, *5* (1), 1–24. https://doi.org/10.1111/1467-9361.00103.
(85) *Collecting and carrying water burdensome reality for women*. UN Women. http://www.unwomen.org/en/news/stories/2014/3/collecting-and-carrying-water-burdensome-reality-for-women (accessed 2019-06-18).
(86) Uddin, R.; Huda, N. H. Arsenic Poisoning in Bangladesh. *Oman Med. J.* **2011**, *26* (3), 207–209. https://doi.org/10. 5001/omj.2011.51.
(87) Dasgupta, P. Economics of Social Capital*. *Econ. Rec.* **2005**, *81* (s1), S2–S21. https://doi.org/10.1111/j.1475-4932.2005.00245.x.
(88) Roy, A.; van Genuchten, C. M.; Mookherjee, I.; Debsarkar, A.; Dutta, A. Concrete Stabilization of Arsenic-Bearing Iron Sludge Generated from an Electrochemical Arsenic Remediation Plant. *J. Environ. Manage.* **2019**, *233*, 141–150. https://doi.org/10.1016/j.jenvman.2018.11.062.
(89) Martínez-Cabanas, M.; Carro, L.; López-García, M.; Herrero, R.; Barriada, J. L.; de Vicente, M. E. S. Achieving Sub-10 Ppb Arsenic Levels with Iron Based Biomass-Silica Gel Composites. *Chem. Eng. J.* **2015**, *279*, 1–8. https://doi.org/10.1016/j.cej.2015.04.148.
(90) Tilak, J. B. G. Education and Poverty. *J. Hum. Dev.* **2002**, *3* (2), 191–207. https://doi.org/10.1080/14649880220147301.
(91) Ayotte, J. D.; Medalie, L.; Qi, S. L.; Backer, L. C.; Nolan, B. T. Estimating the High-Arsenic Domestic-Well Population in the Conterminous United States. *Environ. Sci. Technol.* **2017**, *51* (21), 12443–12454. https://doi.org/10.1021/acs.est.7b02881.

(92) *Public Health Goal for Arsenic*; California Environmental Protection Agency: Office of Environmental Health Hazard Assessment, 2004.
(93) Kohl, P. M.; Medlar, S. J. *Occurrence of Manganese in Drinking Water and Manganese Control*; American Water Works Association, 2006.
(94) Erickson, M. L.; Elliott, S. M.; Brown, C. J.; Stackelberg, P. E.; Ransom, K. M.; Reddy, J. E.; Cravotta, C. A. Machine-Learning Predictions of High Arsenic and High Manganese at Drinking Water Depths of the Glacial Aquifer System, Northern Continental United States. *Environ. Sci. Technol.* **2021**, *55* (9), 5791–5805. https://doi.org/10.1021/acs.est.0c06740.
(95) Lan, S.; Wang, X.; Xiang, Q.; Yin, H.; Tan, W.; Qiu, G.; Liu, F.; Zhang, J.; Feng, X. Mechanisms of Mn(II) Catalytic Oxidation on Ferrihydrite Surfaces and the Formation of Manganese (Oxyhydr)Oxides. *Geochim. Cosmochim. Acta* **2017**, *211*, 79–96. https://doi.org/10.1016/j.gca.2017.04.044.
(96) McBeath, S. T.; Hajimalayeri, A.; Jasim, S. Y.; Mohseni, M. Coupled Electrocoagulation and Oxidative Media Filtration for the Removal of Manganese and Arsenic from a Raw Ground Water Supply. *J. Water Process Eng.* **2021**, *40*, 101983. https://doi.org/10.1016/j.jwpe.2021.101983.
(97) Lakshmanan, D.; Clifford, D. A.; Samanta, G. Ferrous and Ferric Ion Generation During Iron Electrocoagulation. *Environ. Sci. Technol.* **2009**, *43* (10), 3853–3859. https://doi.org/10.1021/es8036669.
(98) Jacobsen, F.; Holcman, J.; Sehested, K. Activation Parameters of Ferryl Ion Reactions in Aqueous Acid Solutions. *Int. J. Chem. Kinet.* **1997**, *29* (1), 17–24. https://doi.org/10.1002/(SICI)1097-4601(1997)29:1<17::AID-KIN3>3.0.CO;2-O.
(99) Dixit, S.; Hering, J. G. Comparison of Arsenic(V) and Arsenic(III) Sorption onto Iron Oxide Minerals: Implications for Arsenic Mobility. *Environ. Sci. Technol.* **2003**, *37* (18), 4182–4189. https://doi.org/10.1021/es030309t.
(100) Hernandez, D.; Boden, K.; Paul, P.; Bandaru, S.; Mypati, S.; Roy, A.; Amrose, S.; Roy, J.; Gadgil, A. Strategies for Successful Field Deployment in a Resource-Poor Region: Arsenic Remediation Technology for Drinking Water. *Dev. Eng.* **2019**, *4*, 100045. https://doi.org/10.1016/j.deveng.2019.100045.
(101) King, D. Whitney.; Lounsbury, H. A.; Millero, F. J. Rates and Mechanism of Fe(II) Oxidation at Nanomolar Total Iron Concentrations. *Environ. Sci. Technol.* **1995**, *29* (3), 818–824. https://doi.org/10.1021/es00003a033.
(102) Van Genuchten, C. M.; Peña, J. Mn (II) Oxidation in Fenton and Fenton Type Systems: Identification of Reaction Efficiency and Reaction Products. *Environ. Sci. Technol.* **2017**, *51* (5), 2982–2991. https://doi.org/10.1021/acs.est.6b05584.
(103) Catrouillet, C.; Hirosue, S.; Manetti, N.; Boureau, V.; Peña, J. Coupled As and Mn Redox Transformations in an Fe(0) Electrocoagulation System: Competition for Reactive Oxidants and Sorption Sites. *Environ. Sci. Technol.* **2020**, *54* (12), 7165–7174. https://doi.org/10.1021/acs.est.9b07099.
(104) Ahmad, A.; van der Wal, A.; Bhattacharya, P.; van Genuchten, C. M. Characteristics of Fe and Mn Bearing Precipitates Generated by Fe(II) and Mn(II) Co-Oxidation with O2, MnO4 and HOCl in the Presence of Groundwater Ions. *Water Res.* **2019**, *161*, 505–516. https://doi.org/10.1016/j.watres.2019.06.036.
(105) King, D. W.; Farlow, R. Role of Carbonate Speciation on the Oxidation of Fe(II) by H2O2. *Mar. Chem.* **2000**, *70* (1), 201–209. https://doi.org/10.1016/S0304-4203(00)00026-8.

(106) Jia, Y.; Xu, L.; Fang, Z.; Demopoulos, G. P. Observation of Surface Precipitation of Arsenate on Ferrihydrite. *Environ. Sci. Technol.* **2006**, *40* (10), 3248–3253. https://doi.org/10.1021/es051872+.
(107) Kelly, S. D.; Hesterberg, D.; Ravel, B. Analysis of Soils and Minerals Using X-Ray Absorption Spectroscopy. In *Methods of Soil Analysis Part 5—Mineralogical Methods*; John Wiley & Sons, Ltd, 2008; pp 387–463. https://doi.org/10.2136/sssabookser5.5.c14.
(108) Calvin, S. *XAFS for Everyone*; CRC Press, 2013.
(109) Webb, S. M. SIXpack: A Graphical User Interface for XAS Analysis Using IFEFFIT. *Phys. Scr.* **2005**, *2005* (T115), 1011. https://doi.org/10.1238/Physica.Topical.115a01011.
(110) Genuchten, C. M. van; Behrends, T.; Dideriksen, K. Emerging Investigator Series: Interdependency of Green Rust Transformation and the Partitioning and Binding Mode of Arsenic. *Environ. Sci. Process. Impacts* **2019**, *21* (9), 1459–1476. https://doi.org/10.1039/C9EM00267G.
(111) Kitahama, K.; Kiriyama, R.; Baba, Y. Refinement of the Crystal Structure of Scorodite. *Acta Crystallogr. Sect. B* **1975**, *31* (1), 322–324. https://doi.org/10.1107/S056774087500266X.
(112) Newville, M. IFEFFIT: Interactive XAFS Analysis and FEFF Fitting. *J. Synchrotron Radiat.* **2001**, *8* (2), 322–324. https://doi.org/10.1107/S0909049500016964.
(113) Kaegi, R.; Voegelin, A.; Folini, D.; Hug, S. J. Effect of Phosphate, Silicate, and Ca on the Morphology, Structure and Elemental Composition of Fe(III)-Precipitates Formed in Aerated Fe(II) and As(III) Containing Water. *Geochim. Cosmochim. Acta* **2010**, *74* (20), 5798–5816. https://doi.org/10.1016/j.gca.2010.07.017.
(114) Delaire, C.; van Genuchten, C. M.; Nelson, K. L.; Amrose, S. E.; Gadgil, A. J. Escherichia Coli Attenuation by Fe Electrocoagulation in Synthetic Bengal Groundwater: Effect of PH and Natural Organic Matter. *Environ. Sci. Technol.* **2015**, *49* (16), 9945–9953. https://doi.org/10.1021/acs.est.5b01696.
(115) Voegelin, A.; Kaegi, R.; Frommer, J.; Vantelon, D.; Hug, S. J. Effect of Phosphate, Silicate, and Ca on Fe(III)-Precipitates Formed in Aerated Fe(II)- and As(III)-Containing Water Studied by X-Ray Absorption Spectroscopy. *Geochim. Cosmochim. Acta* **2010**, *74* (1), 164–186. https://doi.org/10.1016/j.gca.2009.09.020.
(116) Kanel, S. R.; Manning, B.; Charlet, L.; Choi, H. Removal of Arsenic(III) from Groundwater by Nanoscale Zero-Valent Iron. *Environ. Sci. Technol.* **2005**, *39* (5), 1291–1298. https://doi.org/10.1021/es048991u.
(117) King, D. W. Role of Carbonate Speciation on the Oxidation Rate of Fe(II) in Aquatic Systems. *Environ. Sci. Technol.* **1998**, *32* (19), 2997–3003. https://doi.org/10.1021/es980206o.
(118) Katsoyiannis, I. A.; Ruettimann, T.; Hug, S. J. PH Dependence of Fenton Reagent Generation and As (III) Oxidation and Removal by Corrosion of Zero Valent Iron in Aerated Water. *Environ. Sci. Technol.* **2008**, *42* (19), 7424–7430. https://doi.org/10.1021/es800649p.
(119) Sedlak, D. *Water 4.0: The Past, Present, and Future of the World's Most Vital Resource*; Yale University Press, 2014.
(120) Chaplin, B. P. The Prospect of Electrochemical Technologies Advancing Worldwide Water Treatment. *Acc. Chem. Res.* **2019**, *52* (3), 596–604. https://doi.org/10.1021/acs.accounts.8b00611.

(121) Yu, F.; Zhou, M.; Yu, X. Cost-Effective Electro-Fenton Using Modified Graphite Felt That Dramatically Enhanced on H2O2 Electro-Generation without External Aeration. *Electrochimica Acta* **2015**, *163*, 182–189. https://doi.org/10.1016/j.electacta.2015.02.166.
(122) Zhao, Q.; An, J.; Wang, S.; Qiao, Y.; Liao, C.; Wang, C.; Wang, X.; Li, N. Superhydrophobic Air-Breathing Cathode for Efficient Hydrogen Peroxide Generation through Two-Electron Pathway Oxygen Reduction Reaction. *ACS Appl. Mater. Interfaces* **2019**, *11* (38), 35410–35419. https://doi.org/10.1021/acsami.9b09942.
(123) Zhang, Q.; Zhou, M.; Ren, G.; Li, Y.; Li, Y.; Du, X. Highly Efficient Electrosynthesis of Hydrogen Peroxide on a Superhydrophobic Three-Phase Interface by Natural Air Diffusion. *Nat. Commun.* **2020**, *11* (1), 1731. https://doi.org/10.1038/s41467-020-15597-y.
(124) Li, H.; Quispe-Cardenas, E.; Yang, S.; Yin, L.; Yang, Y. Electrosynthesis of >20 g/L H2O2 from Air. *ACS EST Eng.* **2022**, *2* (2), 242–250. https://doi.org/10.1021/acsestengg.1c00366.
(125) Lu, Z.; Chen, G.; Siahrostami, S.; Chen, Z.; Liu, K.; Xie, J.; Liao, L.; Wu, T.; Lin, D.; Liu, Y.; Jaramillo, T. F.; Nørskov, J. K.; Cui, Y. High-Efficiency Oxygen Reduction to Hydrogen Peroxide Catalysed by Oxidized Carbon Materials. *Nat. Catal.* **2018**, *1* (2), 156–162. https://doi.org/10.1038/s41929-017-0017-x.
(126) Yang, S.; Verdaguer-Casadevall, A.; Arnarson, L.; Silvioli, L.; Čolić, V.; Frydendal, R.; Rossmeisl, J.; Chorkendorff, I.; Stephens, I. E. L. Toward the Decentralized Electrochemical Production of H2O2: A Focus on the Catalysis. *ACS Catal.* **2018**, *8* (5), 4064–4081. https://doi.org/10.1021/acscatal.8b00217.
(127) Wang, Z.; Li, Q.-K.; Zhang, C.; Cheng, Z.; Chen, W.; McHugh, E. A.; Carter, R. A.; Yakobson, B. I.; Tour, J. M. Hydrogen Peroxide Generation with 100% Faradaic Efficiency on Metal-Free Carbon Black. *ACS Catal.* **2021**, *11* (4), 2454–2459. https://doi.org/10.1021/acscatal.0c04735.
(128) Brillas, E.; Sirés, I.; Oturan, M. A. Electro-Fenton Process and Related Electrochemical Technologies Based on Fenton's Reaction Chemistry. *Chem. Rev.* **2009**, *109* (12), 6570–6631. https://doi.org/10.1021/cr900136g.
(129) Chatterjee, P.; Ghangrekar, M. M.; Leech, D. A Brief Review on Recent Advances in Air-Cathode Microbial Fuel Cells. *Environ. Eng. Manag. J. EEMJ* **2018**, *17* (7), 1531–1544. https://doi.org/10.30638/eemj.2018.152.
(130) Moreira, F. C.; Boaventura, R. A.; Brillas, E.; Vilar, V. J. Electrochemical Advanced Oxidation Processes: A Review on Their Application to Synthetic and Real Wastewaters. *Appl. Catal. B Environ.* **2017**, *202*, 217–261. https://doi.org/10.1016/j.apcatb.2016.08.037.
(131) Syam Babu, D.; Vijay, K.; Nidheesh, P. V.; Suresh Kumar, M. Performance of Continuous Aerated Iron Electrocoagulation Process for Arsenite Removal from Simulated Groundwater and Management of Arsenic-Iron Sludge. *Sustain. Energy Technol. Assess.* **2021**, *47*, 101476. https://doi.org/10.1016/j.seta.2021.101476.
(132) Bandaru, S. R.; Roy, A.; Gadgil, A. J.; van Genuchten, C. M. Long-Term Electrode Behavior during Treatment of Arsenic Contaminated Groundwater by a Pilot-Scale Iron Electrocoagulation System. *Water Res.* **2020**, 115668. https://doi.org/10.1016/j.watres.2020.115668.
(133) Müller, S.; Behrends, T.; van Genuchten, C. M. Sustaining Efficient Production of Aqueous Iron during Repeated Operation of Fe (0)-Electrocoagulation. *Water Res.* **2019**, *155*, 455–464. https://doi.org/10.1016/j.watres.2018.11.060.
(134) An, J.; Li, N.; Wu, Y.; Wang, S.; Liao, C.; Zhao, Q.; Zhou, L.; Li, T.; Wang, X.; Feng, Y. Revealing Decay Mechanisms of H2O2-Based Electrochemical Advanced Oxidation

Processes after Long-Term Operation for Phenol Degradation. *Environ. Sci. Technol.* **2020**, *54* (17), 10916–10925. https://doi.org/10.1021/acs.est.0c03233.
(135) AvCarb Carbon Papers Properties Sheet Version 1.0. https://www.fuelcellstore.com/teflon-coated-avcarb-p75t (accessed 2022-10-30).
(136) Hosseiny, S. S.; Wessling, M. Ion Exchange Membranes for Vanadium Redox Flow Batteries. In *Advanced Membrane Science and Technology for Sustainable Energy and Environmental Applications*; Basile, A., Nunes, S. P., Eds.; Energy; Woodhead Publishing, 2011; pp 413–434. https://doi.org/10.1533/9780857093790.4.413.
(137) Nozari-Asbemarz, M.; Amiri, M.; Imanzadeh, H.; Bezaatpour, A.; Nouhi, S.; Hosseini, P.; Wark, M.; Seifzadeh, D. Mixed Metal Oxides as Efficient Electrocatalysts for Water Oxidation. *Int. J. Hydrog. Energy* **2022**, *47* (8), 5250–5259. https://doi.org/10.1016/j.ijhydene.2021.11.145.
(138) Shestakova, M.; Sillanpää, M. Electrode Materials Used for Electrochemical Oxidation of Organic Compounds in Wastewater. *Rev. Environ. Sci. Biotechnol.* **2017**, *16* (2), 223–238. https://doi.org/10.1007/s11157-017-9426-1.
(139) Origin(Pro). https://www.originlab.com/.
(140) Marcus, M. A.; MacDowell, A. A.; Celestre, R.; Manceau, A.; Miller, T.; Padmore, H. A.; Sublett, R. E. Beamline 10.3.2 at ALS: A Hard X-Ray Microprobe for Environmental and Materials Sciences. *J. Synchrotron Radiat.* **2004**, *11* (3), 239–247. https://doi.org/10.1107/S0909049504005837.
(141) Kulkarni, A.; Siahrostami, S.; Patel, A.; Nørskov, J. K. Understanding Catalytic Activity Trends in the Oxygen Reduction Reaction. *Chem. Rev.* **2018**, *118* (5), 2302–2312. https://doi.org/10.1021/acs.chemrev.7b00488.
(142) Yuan, Y.; Zhou, S.; Tang, J. In Situ Investigation of Cathode and Local Biofilm Microenvironments Reveals Important Roles of OH– and Oxygen Transport in Microbial Fuel Cells. *Environ. Sci. Technol.* **2013**, *47* (9), 4911–4917. https://doi.org/10.1021/es400045s.
(143) Aguilar, Z. G.; Coreño, O.; Salazar, M.; Sirés, I.; Brillas, E.; Nava, J. L. Ti|Ir–Sn–Sb Oxide Anode: Service Life and Role of the Acid Sites Content during Water Oxidation to Hydroxyl Radicals. *J. Electroanal. Chem.* **2018**, *820*, 82–88. https://doi.org/10.1016/j.jelechem.2018.04.053.
(144) van Genuchten, C. M.; Dalby, K. N.; Ceccato, M.; Stipp, S. L. S.; Dideriksen, K. Factors Affecting the Faradaic Efficiency of Fe(0) Electrocoagulation. *J. Environ. Chem. Eng.* **2017**, *5* (5), 4958–4968. https://doi.org/10.1016/j.jece.2017.09.008.
(145) Cook, D. C.; Van Orden, A. C.; Carpio, J. J.; Oh, S. J. Atmospheric Corrosion in the Gulf of México. *Hyperfine Interact.* **1998**, *113* (1–4), 319–329. https://doi.org/10.1023/A:1012688003125.
(146) Monico, L.; Cartechini, L.; Rosi, F.; De Nolf, W.; Cotte, M.; Vivani, R.; Maurich, C.; Miliani, C. Synchrotron Radiation Ca K-Edge 2D-XANES Spectroscopy for Studying the Stratigraphic Distribution of Calcium-Based Consolidants Applied in Limestones. *Sci. Rep.* **2020**, *10* (1), 14337. https://doi.org/10.1038/s41598-020-71105-8.
(147) Prietzel, J.; Klysubun, W.; Hurtarte, L. C. C. The Fate of Calcium in Temperate Forest Soils: A Ca K-Edge XANES Study. *Biogeochemistry* **2021**, *152* (2), 195–222. https://doi.org/10.1007/s10533-020-00748-6.

(148) An, J.; Li, N.; Wan, L.; Zhou, L.; Du, Q.; Li, T.; Wang, X. Electric Field Induced Salt Precipitation into Activated Carbon Air-Cathode Causes Power Decay in Microbial Fuel Cells. *Water Res.* **2017**, *123*, 369–377. https://doi.org/10.1016/j.watres.2017.06.087.
(149) Mondal, J.; Srivastava, S. K. δ-MnO2 Nanoflowers and Their Reduced Graphene Oxide Nanocomposites for Electromagnetic Interference Shielding. *ACS Appl. Nano Mater.* **2020**, *3* (11), 11048–11059. https://doi.org/10.1021/acsanm.0c02247.
(150) Sebastian, F. L.; Zorn, N. F.; Settele, S.; Lindenthal, S.; Berger, F. J.; Bendel, C.; Li, H.; Flavel, B. S.; Zaumseil, J. Absolute Quantification of Sp3 Defects in Semiconducting Single-Wall Carbon Nanotubes by Raman Spectroscopy. *J. Phys. Chem. Lett.* **2022**, *13* (16), 3542–3548. https://doi.org/10.1021/acs.jpclett.2c00758.
(151) He, H.; Jiang, B.; Yuan, J.; Liu, Y.; Bi, X.; Xin, S. Cost-Effective Electrogeneration of H2O2 Utilizing HNO3 Modified Graphite/Polytetrafluoroethylene Cathode with Exterior Hydrophobic Film. *J. Colloid Interface Sci.* **2019**, *533*, 471–480. https://doi.org/10.1016/j.jcis.2018.08.092.
(152) Zhao, H.; Qian, L.; Chen, Y.; Wang, Q.; Zhao, G. Selective Catalytic Two-Electron O2 Reduction for Onsite Efficient Oxidation Reaction in Heterogeneous Electro-Fenton Process. *Chem. Eng. J.* **2018**, *332*, 486–498. https://doi.org/10.1016/j.cej.2017.09.093.
(153) Glade, S.; Bandaru, S. R.; Nahata, M.; Majmudar, J.; Gadgil, A. Adapting a Drinking Water Treatment Technology for Arsenic Removal to the Context of a Small, Low-Income California Community. *Water Res.* **2021**, *204*, 117595. https://doi.org/10.1016/j.watres.2021.117595.
(154) Amrose, S.; Burt, Z.; Ray, I. Safe Drinking Water for Low-Income Regions. *Annu. Rev. Environ. Resour.* **2015**, *40* (1), 203–231. https://doi.org/10.1146/annurev-environ-031411-091819.
(155) Dasgupta, S.; Roy, J.; Ghosh, M.; Talukder, J. Willingness to Pay (WTP) for Arsenic-Safe Drinking Water: A Case Study to Understand Societal Embedding of ECAR Technology in Rural West Bengal, India. *Dev. Eng.* **2022**, *7*, 100096. https://doi.org/10.1016/j.deveng.2022.100096.
(156) Ying, S. C.; Schaefer, M. V.; Cock-Esteb, A.; Li, J.; Fendorf, S. Depth Stratification Leads to Distinct Zones of Manganese and Arsenic Contaminated Groundwater. *Environ. Sci. Technol.* **2017**, *51* (16), 8926–8932. https://doi.org/10.1021/acs.est.7b01121.
(157) van Genuchten, C. M.; Ahmad, A. Groundwater As Removal by As(III), Fe(II), and Mn(II) Co-Oxidation: Contrasting As Removal Pathways with O2, NaOCl, and KMnO4. *Environ. Sci. Technol.* **2020**, *54* (23), 15454–15464. https://doi.org/10.1021/acs.est.0c05424.
(158) Das, S.; Hendry, M. J.; Essilfie-Dughan, J. Transformation of Two-Line Ferrihydrite to Goethite and Hematite as a Function of PH and Temperature. *Environ. Sci. Technol.* **2011**, *45* (1), 268–275. https://doi.org/10.1021/es101903y.
(159) Senn, A.-C.; Hug, S. J.; Kaegi, R.; Hering, J. G.; Voegelin, A. Arsenate Co-Precipitation with Fe(II) Oxidation Products and Retention or Release during Precipitate Aging. *Water Res.* **2018**, *131*, 334–345. https://doi.org/10.1016/j.watres.2017.12.038.
(160) Voegelin, A.; Senn, A.-C.; Kaegi, R.; Hug, S. J. Reductive Dissolution of As(V)-Bearing Fe(III)-Precipitates Formed by Fe(II) Oxidation in Aqueous Solutions. *Geochem. Trans.* **2019**, *20* (1), 2. https://doi.org/10.1186/s12932-019-0062-2.